



# **Superomniphobic Surfaces for Military Applications: Nano- and Micro-Fabrication Methods**

## *Year Three Report*

*Alidad Amirfazli*

*Prepared by:*

*Alidad Amirfazli*

*Department of Mechanical Engineering*

*University of Alberta*

*Edmonton, AB T6G 2G8*

*PWGSC Contract Number: W7707-098197*

*Contract Scientific Authority: Paul Saville, 250-363-2892*

*The scientific or technical validity of this Contract Report is entirely the responsibility of the contractor and the contents do not necessarily have the approval or endorsement of Defence R&D Canada.*

## **Defence R&D Canada – Atlantic**

Contract Report

DRDC Atlantic CR 2012-216

October 2012

This page intentionally left blank.

# **Superomniphobic Surfaces for Military Applications: Nano- and Micro-Fabrication Methods**

*Year Three Report*

Alidad Amirfazli

Prepared By:  
Alidad Amirfazli  
Department of Mechanical Engineering  
University of Alberta  
Edmonton, Alberta, T6G 2G8

PWGSC Contract Number: W7707-098197  
CSA: Paul Saville, 250 363 2892

The scientific or technical validity of this Contract Report is entirely the responsibility of the Contractor and the contents do not necessarily have the approval or endorsement of Defence R&D Canada.

**Defence R&D Canada – Atlantic**

Contract Report  
DRDC Atlantic CR 2012-216  
October 2012

Principal Author

*Original signed by Alidad Amirfazli*

---

Alidad Amirfazli

Approved by

*Original signed by Gary Fisher*

---

Gary Fisher

Head / Dockyard Laboratory Pacific

Approved for release by

*Original signed by Leon Cheng*

---

Leon Cheng

Chair / Document Review Panel

Sponsored by the 12S Sustain TAG

© Her Majesty the Queen in Right of Canada, as represented by the Minister of National Defence, 2012

© Sa Majesté la Reine (en droit du Canada), telle que représentée par le ministre de la Défense nationale, 2012



## Abstract

---

Superomniphobic surfaces possess unique properties that limit the ability of aqueous and organic liquids to adhere to the surface. As a result surface contamination should be minimized and their cleanability improved. Such traits in a material will have potential benefits to military systems ranging from rainwear, to chemical agent protection, to improved communications, and corrosion protection. This document reports on: the improvement of a sprayable superomniphobic coating by modifying the components; the study of the relationship between surface wear and wetting characteristics using confocal microscopy; and the interpretation of contact angle measurements for liquids on lithographically produced surfaces. A more durable coating was made however it was still susceptible to degradation with liquid contact duration. Skewedness and root mean square roughness surface descriptors have been identified for characterizing wear-wetting relationships; however, a combination of many surface parameters may be required to adequately wetting-wear behaviour. Finally it was found that the cosine of the measured contact angle accurately agrees with the cosine angle predicted by the Cassie equation for measurements made on complex lithographic surfaces, indicating that this equation can be used for designing surfaces.

## Résumé

---

Les surfaces superomniphobes possèdent des propriétés exceptionnelles qui limitent la capacité des liquides aqueux et organiques d'y adhérer. En conséquence, la contamination sur ces surfaces devrait être réduite au minimum et il devrait être plus facile de les entretenir et de les nettoyer. Les matériaux possédant de telles caractéristiques présentent de nombreux avantages potentiels pour les systèmes militaires, des vêtements de pluie aux vêtements de protection contre les agents de guerre chimique, et permettront d'améliorer les communications et la protection contre la corrosion. Le présent document résume des travaux visant à modifier des composants des revêtements superomniphobes pulvérisables dans le but de les améliorer, à étudier le lien entre l'usure de la surface et les caractéristiques de mouillabilité à l'aide de la microscopie confocale et à interpréter des mesures de l'angle de contact entre les liquides et des surfaces produites par des procédés lithographiques. Un revêtement plus durable a été fabriqué, cependant, il reste à ce jour sensible à la dégradation causée par un contact prolongé avec un liquide. De plus, la valeur efficace de la rugosité de la surface et des descripteurs d'asymétrie ont été définis pour caractériser la corrélation entre l'usure de la surface et sa mouillabilité; cependant, il sera peut-être nécessaire de combiner de nombreux paramètres de la surface pour décrire adéquatement cette corrélation. Enfin, on a trouvé que le cosinus de l'angle de contact mesuré était en bon accord avec le cosinus de l'angle prévu par l'équation de Cassie pour des mesures prises sur des surfaces complexes produites par des procédés lithographiques. Il est donc possible de conclure que cette équation peut être utilisée pour concevoir des surfaces.

This page intentionally left blank.

## Executive summary

---

### Superomniphobic Surfaces for Military Applications: Nano- and Micro-Fabrication Methods: Year Three Report

Alidad Amirfazli; DRDC Atlantic CR 2012-216; Defence R&D Canada – Atlantic; October 2012.

**Introduction:** Contamination of a material surface by liquids and solids can be unsightly, cause corrosion, degrade performance or in the case of chemical agents can increase exposure. Superomniphobic surfaces possess unique properties that limit the ability of liquids to adhere to surfaces and can facilitate contamination removal. Such traits in a material will have potential benefits to military systems ranging from rainwear, to chemical agent protection and decontamination, to improved communications, and corrosion protection. This report by the University of Alberta focuses on the development of a durable oil and water repellent coating, understanding how performance changes with surface wear and developing a theoretical understanding of how liquids interact with complex surfaces.

**Results:** Formulation optimization of a previously developed sprayable coating composed of nanoparticles, binder, dispersant, and hydrophobic polymer, improved the coating performance but was still susceptible to prolonged water immersion of more than three days. In order to develop more durable coatings, a number of surfaces were characterized for wear using surface roughness descriptors that show promise in relating topography-wetting behaviour; however a definitive relationship has yet to be found. Finally measurements made of water, oil, and other liquids in contact with lithographically produced surfaces designed to minimize wetting were in agreement with theoretical calculations based on the Cassie equation, suggesting that this equation can be used in the future for designing complex surfaces.

**Significance:** Superomniphobic coatings show potential for a number of military applications, including self-cleaning, anti-icing and decontamination. The development of useful coatings suitable for military environments depends, in part, on the durability of the material. The fragile structures inherent in superorganophobic materials wear easily, degrading the materials performance. Characterization of wear-wetting relationships may result in the development of better materials.

**Future plans:** Further work will investigate the applicability of non-wetting materials to military applications such as decontamination, anti-icing materials, and rapid liquid shedding for applications such as antenna performance improvement.

## Sommaire

---

### Superomniphobic Surfaces for Military Applications: Nano- and Micro-Fabrication Methods: Year Three Report

Alidad Amirfazli ; DRDC Atlantic CR 2012-216 ; R & D pour la défense Canada – Atlantique; octobre 2012.

**Introduction :** La contamination de la surface des matériaux par des liquides et des solides peut rendre celle-ci inesthétique, causer de la corrosion ou, dans le cas de produits chimiques, en augmenter l'exposition. Les surfaces superomniphobes possèdent des propriétés exceptionnelles qui limitent la capacité des liquides aqueux et organiques d'y adhérer et facilitent la décontamination. Les matériaux possédant de telles caractéristiques présentent de nombreux avantages potentiels pour les systèmes militaires, des vêtements de pluie aux vêtements de protection contre les agents de guerre chimique et les produits de décontamination, et permettront d'améliorer les communications et la protection contre la corrosion. Le présent rapport de l'Université de l'Alberta porte sur la mise au point d'un revêtement oléofuge et hydrofuge durable. Il décrit comment le rendement change lorsqu'une surface s'use et présente les principes théoriques sur la façon dont les liquides interagissent avec des surfaces complexes.

**Résultats :** L'optimisation de la formule d'un revêtement pulvérisable mis au point antérieurement et composé de nanoparticules, d'un liant, d'un agent dispersant et d'un polymère hydrophobe a permis d'améliorer le rendement du revêtement, qui est toutefois demeuré sensible à une immersion prolongée dans l'eau pendant plus de trois jours. Pour obtenir des revêtements plus durables, on a caractérisé un certain nombre de surfaces selon leur degré d'usure au moyen de descripteurs de rugosité. Cette méthode s'est révélée prometteuse, car elle permet d'établir une relation entre la topographie d'une surface et son comportement en matière de mouillabilité, mais il demeure qu'une corrélation définitive n'a pas encore été établie. Enfin, les mesures de l'eau, de l'huile et d'autres liquides en contact avec des surfaces produites par des procédés lithographiques conçues pour réduire au minimum le mouillage concordent avec les calculs théoriques fondés sur l'équation de Cassie, ce qui suggère que l'équation pourra être utilisée pour concevoir des surfaces complexes.

**Portée :** Les revêtements superomniphobes présentent un potentiel pour un certain nombre d'applications militaires, y compris l'autonettoyage, le déglçage et la décontamination. La mise au point de revêtements utiles convenant aux environnements militaires dépend, en partie, de la durabilité du matériau. À cause de la fragilité de leur structure, les matériaux superorganophobes s'usent facilement, ce qui diminue leur rendement. La caractérisation de la corrélation entre l'usure de la surface et sa mouillabilité pourrait se traduire par la mise au point de matériaux plus durables.

**Recherches futures :** De futurs travaux permettront d'étudier l'applicabilité de matériaux impossibles à mouiller à des fins militaires comme la décontamination, le déglçage et l'élimination rapide de liquides, qui permettront d'améliorer le rendement des antennes.

# Table of contents

---

Abstract .....	i
Résumé .....	i
Executive summary .....	iii
Sommaire .....	iv
Table of contents .....	v
List of figures .....	vii
List of tables .....	xii
1 Overview.....	1
2 Sprayable Superhydrophobic Coatings: Component Optimization .....	2
2.1 Introduction .....	2
2.2 Materials and Methods .....	3
2.2.1 Solvent Concentration .....	3
2.2.2 Nanoparticle Concentration .....	4
2.2.3 Cross-Linker Concentration.....	4
2.2.4 Experimental Set-up .....	4
2.3 Results and Discussion .....	5
2.3.1 Solvent Concentration .....	5
2.3.2 Nanoparticle Concentration .....	15
2.3.3 Cross-Linker Concentration.....	20
2.4 Conclusions .....	23
3 Wetting Performance of Worn Superhydrophobic Surfaces.....	24
3.1 Introduction .....	24
3.1.1 Literature Review .....	26
3.1.2 Motivation of the Study .....	26
3.2 Experimental Section.....	26
3.2.1 Fabricating Pillars with Flat Tops.....	28
3.3 Results and Discussion .....	29
3.3.1 Use of White Light Confocal Microscope in Imaging the Water-Air Interface .....	29
3.3.2 Future Work.....	34
3.4 Characterizing Surfaces through Surface Topography Descriptors .....	34
3.4.1 Introduction.....	35
3.4.2 Way Forward .....	35
3.4.3 Experimental Methods.....	36
3.4.4 Results and Discussion .....	40
3.4.4.1 Quantitative Examination of Surface Wear and Wetting Characteristics.....	40

3.4.4.2	Evolution of Surface Topographical Descriptors.....	57
3.4.5	Future Work.....	63
4	Superhydrophobic and Superoleophobic Behaviour on Variant Geometry Micropillar Arrays .....	64
4.1	Introduction .....	64
4.2	Procedure.....	67
4.3	Results .....	68
4.4	Analysis .....	70
4.5	Future Work .....	74
5	Publications.....	75
	References .....	77
	List of symbols/abbreviations/acronyms/initialisms .....	79
	Distribution list.....	81

## List of figures

---

Figure 2-1: Schematic of the treated glass sample showing the relevant portions for the preliminary immersion test performed.....	5
Figure 2-2: CA and SA measurements vs. solvent concentration for unimmersed samples.....	6
Figure 2-3: CA and SA measurements vs. solvent concentration for a total immersion of 24 hours.....	6
Figure 2-4: CA and SA measurements vs. solvent concentration for a total immersion of 48 hours.....	7
Figure 2-5: CA and SA measurements vs. solvent concentration for a total immersion of 72 hours.....	7
Figure 2-6: Advancing CA measurements vs. immersion time for each solvent concentration.....	9
Figure 2-7: Receding CA measurements vs. immersion time for each solvent concentration.....	9
Figure 2-8: CA Hysteresis vs. immersion time for each solvent concentration.....	10
Figure 2-9: SA measurements vs. immersion time for each solvent concentration.....	10
Figure 2-10: CA Hysteresis (difference of cosines) vs. immersion time for each solvent concentration.....	11
Figure 2-11: SEM Images for 50% solvent concentration, before and after 72-hour immersion in water.....	12
Figure 2-12: SEM Images for 75% solvent concentration, before and after 72-hour immersion in water.....	12
Figure 2-13: SEM Images for 100% solvent concentration, before and after 72-hour immersion in water.....	13
Figure 2-14: SEM Images for 125% solvent concentration, before and after 72-hour immersion in water.....	13
Figure 2-15: SEM Images for 150% solvent concentration, before and after 72-hour immersion in water.....	14
Figure 2-16: SEM Images at 1000X and 5000X magnification of SiO <sub>2</sub> particles.....	15
Figure 2-17: CA and SA measurements vs. nanoparticle concentration for unimmersed samples. Due to increased viscosity, 200% nanoparticle concentration was impossible to spray with internal mixing airbrush. Plot clearly shows improved wetting performance with increasing nanoparticle concentration.....	16
Figure 2-18: CA and SA measurements vs. nanoparticle concentration for samples immersed for 24 hours. It can be seen that 150% nanoparticle concentration provides the best performance for this immersion period.....	16
Figure 2-19: CA and SA measurements vs. nanoparticle concentration for samples immersed for 48 hours. It can be seen that 150% nanoparticle concentration still provides the best performance for this immersion period.....	17

Figure 2-20: CA and SA measurements vs. nanoparticle concentration for samples immersed for 72 hours. It can be seen that 150% nanoparticle concentration provides the best performance overall. ....	17
Figure 2-21: Advancing CA vs Immersion Time for different nanoparticle concentrations. It can be seen from the plot that after 72 hours, 150% nanoparticle concentrations maintains the highest CA. ....	18
Figure 2-22: Receding CA vs Immersion Time for different nanoparticle concentrations. It can be seen from the plot that after 72 hours, 150% nanoparticle concentrations maintains the highest CA. ....	19
Figure 2-23: CA hysteresis vs Immersion Time for different nanoparticle concentrations. It can be seen from the plot that after 72 hours, 150% nanoparticle concentrations has the lowest hysteresis. ....	19
Figure 2-24: SA measurements vs Immersion Time for different nanoparticle concentrations. It can be seen from the plot that after 72 hours, 150% nanoparticle concentrations maintains the lowest SA. ....	20
Figure 2-25: Advancing CA vs. Cross Linker concentration for different cumulative immersion periods. It can be seen from the plot that concentrations up to 7.4% maintain the highest CA. ....	21
Figure 2-26: Receding CA vs. Cross Linker concentration for different cumulative immersion periods. It can be seen from the plot that 7.4% concentration shows the smallest change between any immersion period (i.e., maximum change/difference is between 0 hrs and 72 hrs). ....	22
Figure 2-27: CA Hysteresis vs. Cross Linker concentration for different cumulative immersion periods. It can be seen from the plot that 7.4% concentration shows the smallest change between any immersion period (i.e., maximum change/difference, between 0 hrs and 72 hrs, is $14.85^\circ$ ). ....	22
Figure 3-1: Illustration showing water drop resting on a superhydrophobic surface. Also, it is shown how the parameters $f_1$ and $f_2$ , used in the Cassie Equation (3-1), are defined and calculated. ....	25
Figure 3-2: SEM of unworn plasma etched Teflon. ....	27
Figure 3-3: a) SEM image of silanized Si cylindrical flat-top pillars arranged in a rectangular unit cell. b) PDMS pillars fabricated by making a double negative of the pillars shown in Figure a), c) AZ P4620 hemispherical dome cylindrical pillars. ....	29
Figure 3-4: a) CSM “all-in-focus” image of the PDMS superhydrophobic structure with cylindrical flat-top pillars arranged in a rectangular unit cell. b) height profile of the above pillars taken on as denoted by red line in above figure. Pillar height is $10\text{ }\mu\text{m}$ , and their diameter is $8\text{ }\mu\text{m}$ with a centre-to-centre pillar distance of $15\text{ }\mu\text{m}$ . .	30
Figure 3-5: Schematic showing the set-up for imaging the water-air interface on PDMS cylindrical pillar substrate. The SHS is placed in a Petri dish, which is subsequently filled with water just until the SHS is fully covered in water. A water immersion objective with 20x magnification is used to image the surface topography. White areas indicate air. ....	31



Figure 3-6: Possible shape of the interface near pillar boundaries and over the pillar tops. The boundary pillar without the air pocket on top demonstrates another possible interface.....	31
Figure 3-7: a) CSM image of the PDMS SHS surface immersed under water. On the right is the smooth PDMS surface base acting as a reference. b) Line profile of the immersed SHS, taken along the red line depicted in a). It can be seen that the pillar on the edge has not been imaged correctly. Also, the rest of the pillars have been elevated by a certain degree which in reality should be aligned with the smooth PDMS surface.....	32
Figure 3-8: a) CSM image of the PDMS SHS surface immersed under water. A portion of the SHS on the right is in Wenzel regime, as signified by the color change. On the right of the pillars is the smooth PDMS surface acting as a reference. b) height profile taken along the red line depicted in a). .....	34
Figure 3-9: Hydrophobic bulk in a SHS eliminates studying changes in surface chemistry, and allows focussing only on surface topography as it is a prime factor in imparting superhydrophobicity.....	36
Figure 3-10: SEM of unworn plasma etched Teflon. ....	37
Figure 3-11: Photograph of abrasion setup.....	38
Figure 3-12: Flowchart of experimental procedure. SHS is abraded and cleaned of contaminants. Topography and wetting are characterized by CSM and CAs respectively. ....	39
Figure 3-13: Schematic showing regions of sample and respective characterization done. The holes signify the place where syringe is inserted from the bottom for ADSA CA measurements. Numbered portions 1, 2, and 3 in the lower right corner signify the sample portions which were systematically cut out after each wear cycle. ....	40
Figure 3-14: SEM of sample 17 being worn at 250 rpm for different durations of time. Inset shows the cumulative time a surface has been worn. In Figure (a) the protrusion is an artifact stuck on the surface. Figure (a) also shows the regional dependency of wear, due to it being a stochastic phenomenon. ....	42
Figure 3-15: SEM of sample 25 as it is worn down at 250 rpm. Inset shows the time the sample has been worn down for. ....	44
Figure 3-16: SEM of sample 18 being worn at 250 rpm for different durations of time. Inset shows the cumulative time a surface has been worn. ....	46
Figure 3-17: Surface profiles for (a) unworn, (b) 3, (c) 12, and (d) 27-minute worn samples evaluated from CSM data. The profiles are for sample 25.....	47
Figure 3-18: Normalized histograms for (a) unworn, (b) 3, (c) 12, and (d) 27 minute worn samples evaluated from CSM data. The corresponding height profiles are displayed in Figure 3-16. It can be seen that height distribution starts as Gaussian, becomes positively skewed Poisson distribution, and then becomes a lognormal distribution with high peaks and low valleys removed. The histogram distributions are for sample 25. The information has undergone noise filtering to remove artificial peaks and valleys. ....	48

Figure 3-19: Illustrating the length of flattened patches on sample 25 SEM, worn for 3 minutes. The small black bars have length of 10 $\mu\text{m}$ , and bigger bars are of length 20 $\mu\text{m}$ . It can be seen that surface has large number of flattened patches with 10 $\mu\text{m}$ length, and some of them extend to 20 $\mu\text{m}$ . The black bars act as a visual guide to flat patches on the surface. ....	49
Figure 3-20: Surface profiles for (a) unworn, (b) 3 minutes, (c) 12 minutes, and (d) 27-minutes worn samples. The profiles are for sample 27-1.....	50
Figure 3-21: Normalized histograms for (a) unworn, (b) 3 min, (c) 12 minutes, and (d) 27-minutes worn samples evaluated from CSM data. The corresponding height profiles are displayed in Figure 3-17. It can be seen that height distribution starts as Gaussian, becomes positively skewed, and then returns to Gaussian but with high peaks and low valleys removed. The profiles are for sample 27-1. The information has undergone noise filtering to remove artificial peaks and valleys. ....	51
Figure 3-22: Comparing height distribution in (a) Sample 25, and (b) Sample 27-1 at unworn, 3 minutes, and 27 minute of wear duration. Normalized histograms have been evaluated from CSM data. The information has undergone noise filtering to remove artificial peaks and valleys. ....	52
Figure 3-23: Wetting data on plasma etched PTFE surface, sample 18. This graph shows the wetting data in the initial stages of wearing. ....	54
Figure 3-24: Wetting data on plasma etched PTFE surface, sample 17. Graph tabulates the long term wear wetting data. ....	55
Figure 3-25: Wetting data on various plasma etched PTFE surfaces. ....	56
Figure 3-26: Normalized histograms for the samples when the hysteresis jumps, (a) Sample 25 at 9 minutes, (b) Sample 27-1 at 6 minutes, and (c) Sample 27-2 at 24 minutes... ..	57
Figure 3-27: RMS roughness for PTFE worn surfaces. ....	58
Figure 3-28: Schematic showing surface profile and the corresponding skewness distribution curve. <sup>26</sup> .....	59
Figure 3-29: Evolution of skewness as a surface wears down. Error bars show the standard deviation in the parameter. ....	60
Figure 3-30: Schematic showing surface topography and corresponding kurtosis. <sup>26</sup> .....	62
Figure 3-31: Evolution of kurtosis as a surface wears down. Error bars show the standard deviation in the parameter. ....	62
Figure 4-1: SEM image of the micropillars with overhanging caps. Image taken at 7000X magnification.....	66
Figure 4-2: The oleophobic wafer with placed hexadecane drops on the seven cases tested.....	66
Figure 4-3: Hexadecane drop developed on Case 8 of the surface. The end state of the advancing (A) drop when it is at 75 $\mu\text{L}$ is shown on the left, while the end state of the receding (R) drop when it is at 10 $\mu\text{L}$ is shown on the right. ....	67
Figure 4-4: SEM image of Case 7 and the intermittent connectivity between the pillar tops. Image taken at 5000X. ....	68

Figure 4-5: Expected and observed advancing and receding angles for water plotted against the Cassie fractions for each case.....	70
Figure 4-6: Expected and observed advancing and receding angles for ethylene glycol plotted against the Cassie fractions for each case. ....	71
Figure 4-7: Expected and observed advancing and receding angles for hexadecane plotted against the Cassie fractions for each case. ....	71
Figure 4-8: Cosine averaged contact angles with water vs. Cassie fraction.....	72
Figure 4-9: Cosine averaged contact angles with ethylene glycol vs. Cassie fraction. ....	73
Figure 4-10: Cosine averaged contact angles with hexadecane vs. Cassie fraction. ....	73

## List of tables

---

Table 1-1: The project goals for year three. ....	1
Table 2-1: Percentages by weight of the different components used in the B22 using nanoclay (NC) or SiO <sub>2</sub> nano particles. B22-SiO <sub>2</sub> contains the same volume of nanoparticles as B22-NC. The component weight percentages are different between the formulations due to the different nano particle densities. ....	3
Table 4-1: Measured dimensions of the tops of the pillars for the oleophobic wafer compared with their designed dimensions. ....	68
Table 4-2: Table of measured contact angles with water on the various cases. ....	69
Table 4-3: Table of measured contact angles with ethylene glycol on the various cases.....	69
Table 4-4: Table of measured contact angles with hexadecane on the various cases. ....	69

# 1 Overview

---

This report covers the activities done in year three as described in Table 1-1. There are three main chapters reporting on results for each of the topics described in the Table 1-1. Also, the following dissemination of work was done based on the results obtained in the reporting period, and it is anticipated that further work can be published from the results of this study (an example is given below).

## Journal Publications

- G. Fang, A. Amirfazli, "Understanding the Edge Effect in Wetting: A Thermodynamic Approach", Langmuir, 28, 9421-9430, 2012

## Journal Papers (in preparation)

- B.M. Koch, J.W. Elliott, A. Amirfazli, "Towards Understanding of Superomniphobic Surfaces"

## Conference Presentations

- G. Fang, A. Amirfazli, "A Thermodynamic Approach to Describe Spreading of Sessile Drops Encountering a Sharp Edge", CECAM workshop "Modeling Wetting Phenomena: From Particle Based Models to the Continuum" Lausanne, Switzerland, Sept. 14-16, 2011

*Table 1-1: The project goals for year three.*

<b>To further our understanding of the relationship between surface texture and contact angle and contact angle hysteresis for surfaces that are worn to allow design of durable superomniphobic surfaces</b>
To conclude the fabrication techniques for production of: <ul style="list-style-type: none"><li>• model surfaces with high liquid repellency through either of silicon or polymeric materials</li><li>• practical surface with high liquid repellency that are sprayable</li></ul>

## 2 Sprayable Superhydrophobic Coatings: Component Optimization

---

The development, optimization, and characterization of sprayable, high-performing and durable superhydrophobic (SH) coatings have been carefully studied over the last three years. While sprayable SH coatings were developed during the first reporting year, they were found to be mechanically fragile and susceptible to prolonged water exposure. Nonetheless, the concept of being able to develop and spray SH coatings was clearly demonstrated, paving the way for work that has been done on optimizing component selection and concentration in order to achieve the highest hydrophobicity and durability. The work that has been performed as part of this study can be summarized as follows:

- Developed, characterized and tested a sprayable SH coating.
- Achieved mechanical and water durable coatings through an investigation of alternate components and their concentrations (without sacrificing coating versatility).
- Determined optimum application (i.e., number of coats and coating thickness) and curing techniques (i.e., combinations of temperature, vacuum, and time) for maximum wetting performance and coating durability.
- Demonstrated that the sprayable SH coating can be used for Lab-on-Chip and Lab-on-Paper applications. The results of such work have been published and presented to the scientific community.
- Developed alternative/conceptual SH coatings where different nanoparticles and/or components are used. Additionally, a set of different layered SH coatings have been proposed for study.
- Demonstrated that correct solvent and nanoparticle concentrations would maximize a coating's wetting performance. This wetting performance improvement, combined with optimized cross-linker concentrations, could also result in durability improvements when subject to prolonged immersion in water.

### 2.1 Introduction

The work described in this chapter continues on the development of the sprayable superhydrophobic (SH) coating and the optimization of its various components. Specifically, it presents quantitative and qualitative information on the optimization of solvent and nanoparticle concentrations of the SH coating developed to date. This work has been motivated by evidence presented by Bayer et al.<sup>1-4</sup> on the sensitivity of their sprayable SH coatings to different component concentrations in the context of wetting performance and coating durability. Given that our own SH coating consists of similar components to Bayer's,<sup>5</sup> it has been decided that we must optimize our component concentrations in order to find an optimum SH coating with improved durability and wetting performance.

## 2.2 Materials and Methods

The starting formulation for this optimization study is the previously reported B22.<sup>32</sup> However, based on previously reported information related to montmorillonite nanoclay's ability to absorb and hold water, it was decided to use SiO<sub>2</sub> particles instead. While an optimum SiO<sub>2</sub> particle concentration is currently under study, it has been determined empirically that an equal volume of SiO<sub>2</sub> particles to that occupied by nanoclay particles as used to date, would be sufficient to render the coating superhydrophobic. Table 2-1 contains the weight percentages of the original B22 formulation (i.e., with nanoclay particles) compared to the modified version containing the SiO<sub>2</sub> nanoparticles. The new formulation presented (B22-SiO<sub>2</sub>) is used as the new baseline for the optimization of the solvent and nanoparticle concentrations.

*Table 2-1: Percentages by weight of the different components used in the B22 using nanoclay (NC) or SiO<sub>2</sub> nano particles. B22-SiO<sub>2</sub> contains the same volume of nanoparticles as B22-NC. The component weight percentages are different between the formulations due to the different nano particle densities.*

Component	B22-NC % wt	B22-SiO <sub>2</sub> % wt
Nanomer ® Nanoclay Particles	6.28%	
SiO <sub>2</sub> Nanoparticles		0.92%
Gorilla Glue Adhesive	2.34%	2.85%
Trifluoroethanol Solvent	37.88%	39.45%
4FVBA Fluonova Sealant	29.44%	31.51%
Poly-isocyanate Cross Linker	1.83%	1.95%
Teflon® AF	22.34%	23.31%
TOTAL	100%	100%

### 2.2.1 Solvent Concentration

The first step in component optimization was to investigate the effect of different solvent concentrations on the wetting performance and durability of treated microscope glass slides when immersed in water for prolonged periods of time. Taking the baseline formulation's (B22-SiO<sub>2</sub>) solvent concentration as 100%, different batches of SH paint were made with solvent concentrations of 50%, 75%, 100%, 125% and 150%.

### **2.2.2 Nanoparticle Concentration**

Following the conclusion on the optimum solvent concentration, the next step was to investigate the effect of different nanoparticle concentrations on the wetting performance and durability of treated microscope glass slides when immersed in water for prolonged periods of time. The baseline formulation for these tests is B22-SiO<sub>2</sub> for the optimum solvent concentration as determined from the solvent concentration optimization investigation. Different batches of the SH paint were made with nanoparticle concentrations of 100%, 125%, 150%, 175%, and 200%.

### **2.2.3 Cross-Linker Concentration**

Prior to determining the optimum adhesive polymer concentrations, an optimization of the cross-linker concentration was performed. Different cross-linker concentrations were added to the fluoropolymer (4FVBA Fluonova Sealant) to determine its effect on the fluoropolymer's durability (in terms of wetting behaviour) over a prolonged water immersion period. The following cross-linker concentrations were studied: 0%, 5.44% (effective cross-linker concentration with respect to 4FVBA and Gorilla Glue), 7.4% (manufacturer's recommended ratio), 15%, 30%, and 50%.

### **2.2.4 Experimental Set-up**

After mixing the different batches of SH paint, they were sprayed on microscope glass slides with a single thick layer (B\*T as previously reported).<sup>32</sup> Each batch of paint (i.e., for each solvent concentration, and, subsequently, for each nanoparticle concentration) was sprayed onto two microscope slides such that statistically significant data could be obtained. A total of 10 microscope slides were treated (2 samples for each of the 5 different concentrations) for each optimization case. The samples were allowed to cure in vacuum at 100°C for a period of 3 hours prior to any testing or characterization.

Treated samples would then be characterized by using the contact angle (CA) and sliding angle (SA) measuring machine in our labs, as well as the Scanning Electron Microscope (SEM) available to our group at the University's NanoFab facilities. After characterizing the freshly prepared and cured samples, they were immersed in deionized (DI) water for a total of 72 hours (with 24-hour intervals). The samples were characterized following each immersion interval in order to monitor the progress/trends in the coatings' durability. SEM images were only obtained on one set of samples (i.e., one of the two samples for each solvent concentration) after the immersion testing was complete, providing information only on the initial (unimmersed) and final (72-hour immersion) topographies. The sliding angle is as the name implies the angle at which the drop will slide across a tilted surface. A small sliding angle implies that there is little adhesion of the drop to the surface. The advancing and receding contact angles are the angles on the downhill and uphill sides of a pinned drop, respectively, or the angles formed as a drop grows or shrinks, respectively. The difference in advancing and receding contact angles, the hysteresis is another measure of the adhesion of the drop to the surface.



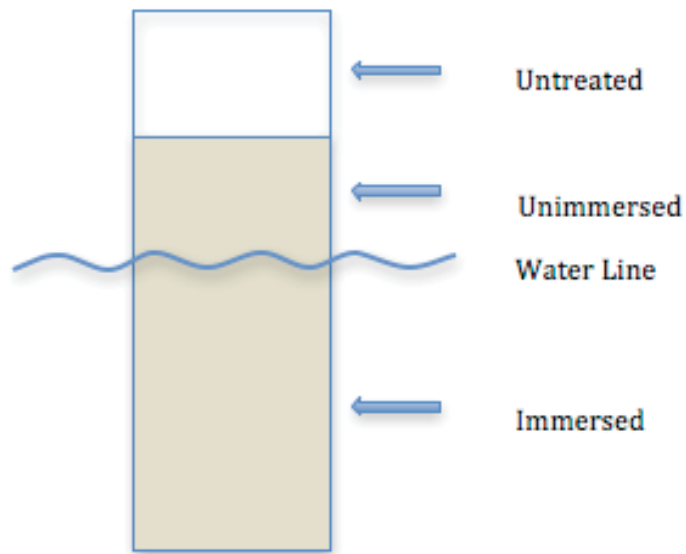


*Figure 2-1: Schematic of the treated glass sample showing the relevant portions for the preliminary immersion test performed.*

## **2.3 Results and Discussion**

### **2.3.1 Solvent Concentration**

The following figures contain the contact and sliding angle measurements for the samples treated with the different batches (i.e., contact/sliding angle vs. solvent concentration). Each plot is for a different immersion interval as follows:

- Figure 2-2: Unimmersed
- Figure 2-3: Immersed for 24 hours
- Figure 2-4: Immersed for 48 hours
- Figure 2-5: Immersed for 72 hours

It can be seen that in three out of four of the immersion periods (unimmersed, 24 hours and 72 hours), that 75% solvent concentration provides the highest contact angles while at the same time the smallest sliding angle measurements. The baseline solvent concentration (i.e., 100%) has similar wetting performance, yet inferior to 75% solvent concentration. The remaining solvent concentrations (50%, 125%, and 150%) show lower contact angles and higher sliding angles.

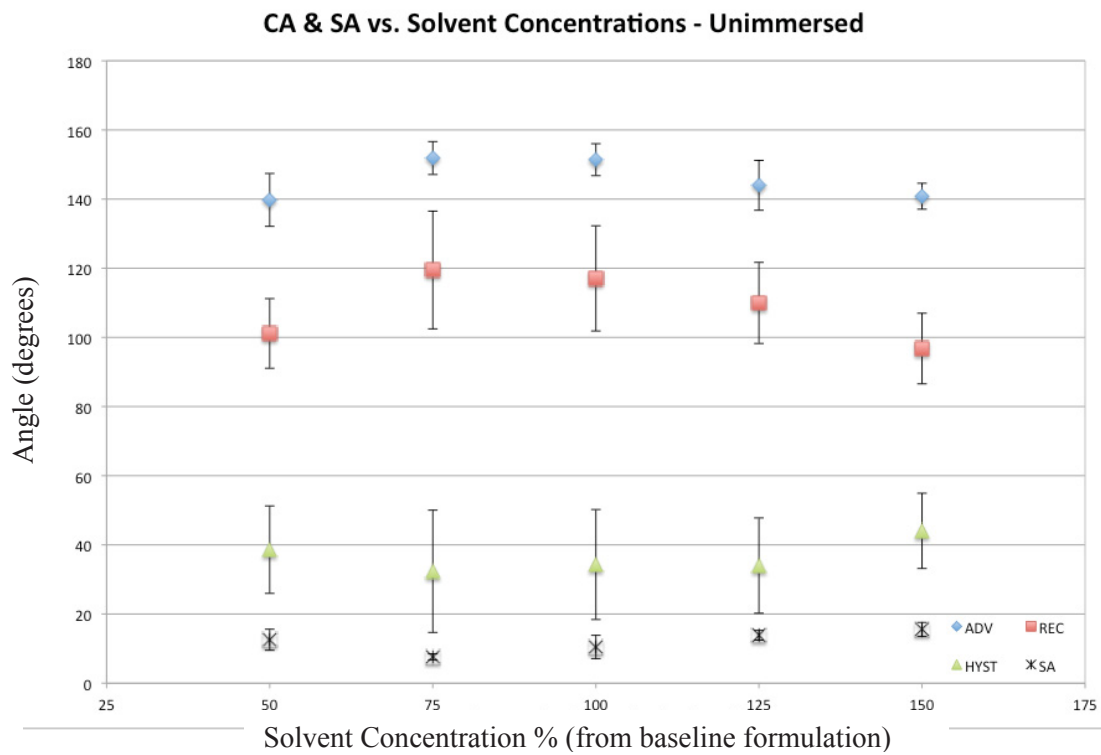


Figure 2-2: CA and SA measurements vs. solvent concentration for unimmersed samples.

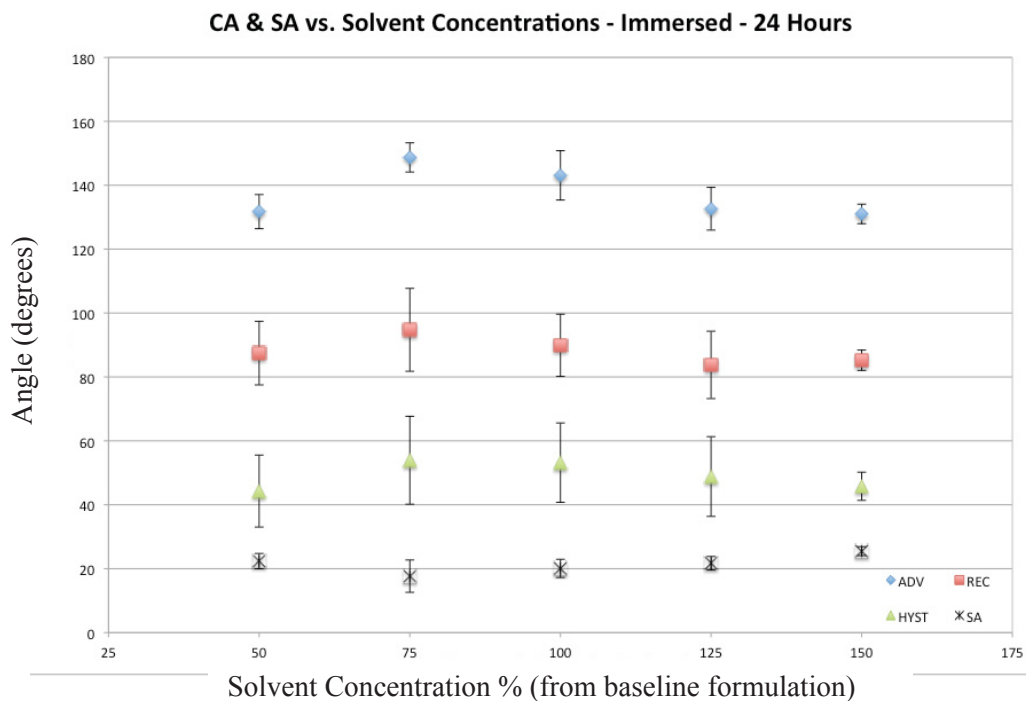


Figure 2-3: CA and SA measurements vs. solvent concentration for a total immersion of 24 hours.

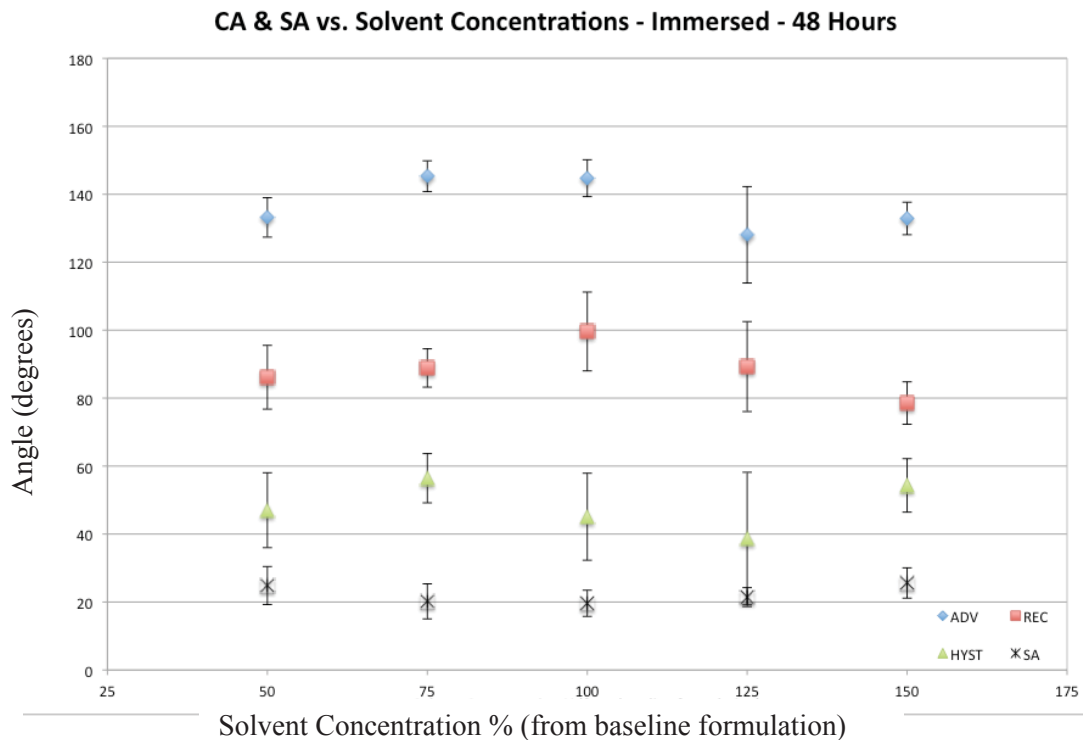


Figure 2-4: CA and SA measurements vs. solvent concentration for a total immersion of 48 hours.

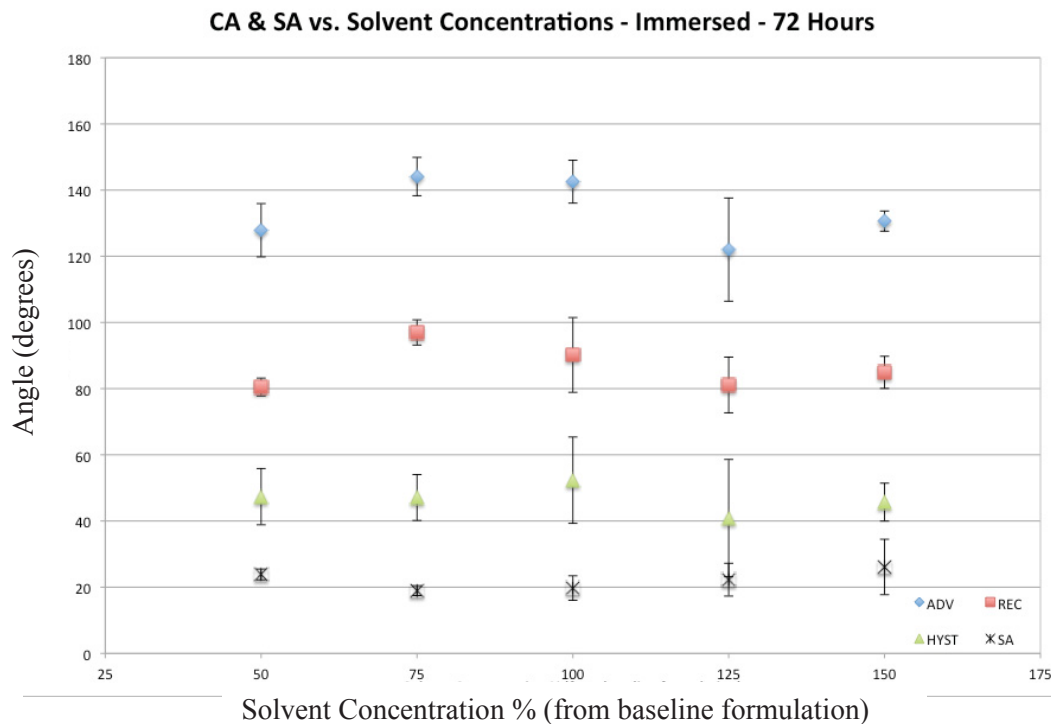


Figure 2-5: CA and SA measurements vs. solvent concentration for a total immersion of 72 hours.

The following figures show the CA and SA measurements plotted independently from each other with immersion time as the variable (i.e., contact angle vs. immersion time). Each plot is for a different angle measurement, showing its variation with immersion time and solvent concentration as follows:

- 50% solvent concentration
- 75% solvent concentration
- 100% solvent concentration
- 125% solvent concentration
- 150% solvent concentration

Contact angle hysteresis is presented in two ways:

- Difference between advancing and receding contact angle
- Difference between the cosines of receding and advancing contact angles

The latter was chosen as an alternative given its more frequent use in literature when describing contact angle hysteresis.

It can be seen from the individual angle plots that while 75% and 100% solvent concentrations are consistently better performers (i.e., higher advancing and receding contact angles with lower sliding angles), 75% continues to appear to be the best performer. The remaining solvent concentrations (50%, 125% and 150%) are either significantly inferior to 75% and 100% or have sharper decreases in performance over time.

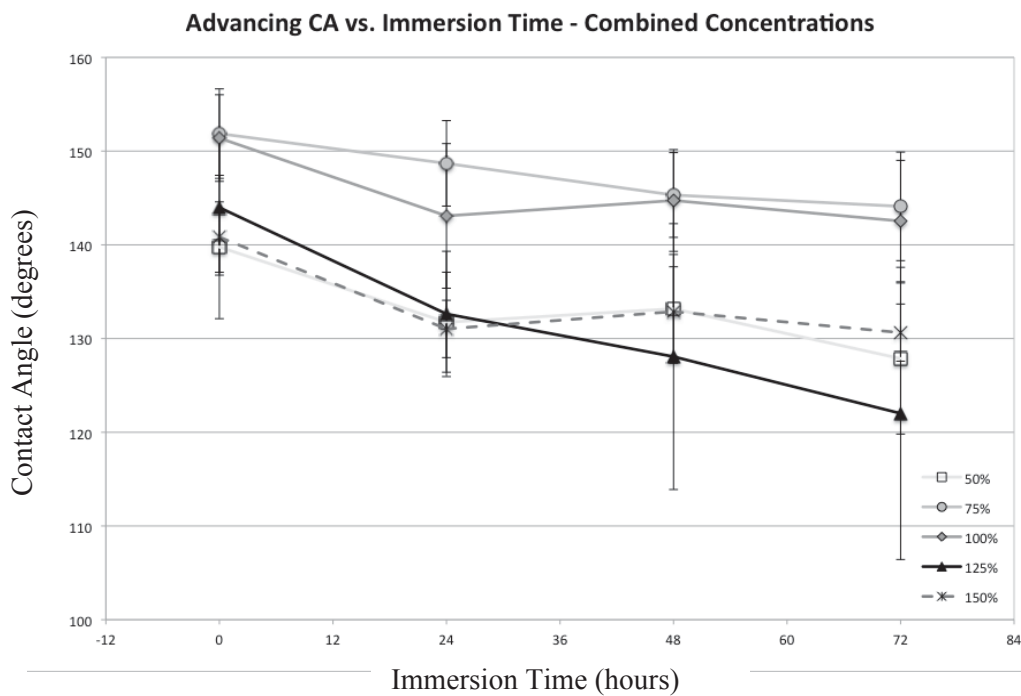


Figure 2-6: Advancing CA measurements vs. immersion time for each solvent concentration.

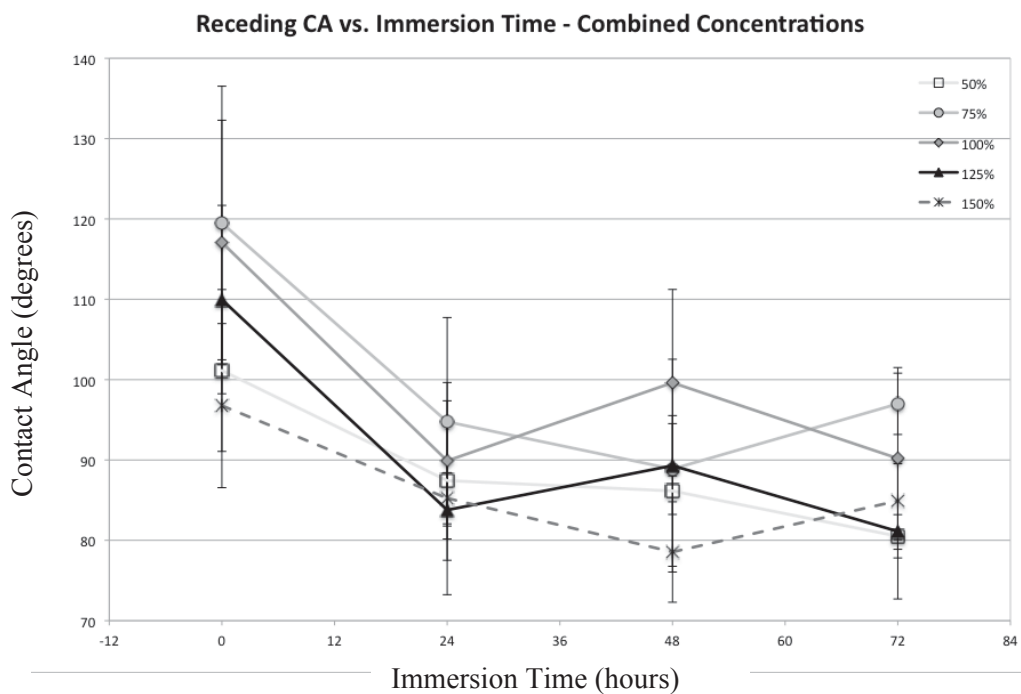


Figure 2-7: Receding CA measurements vs. immersion time for each solvent concentration.

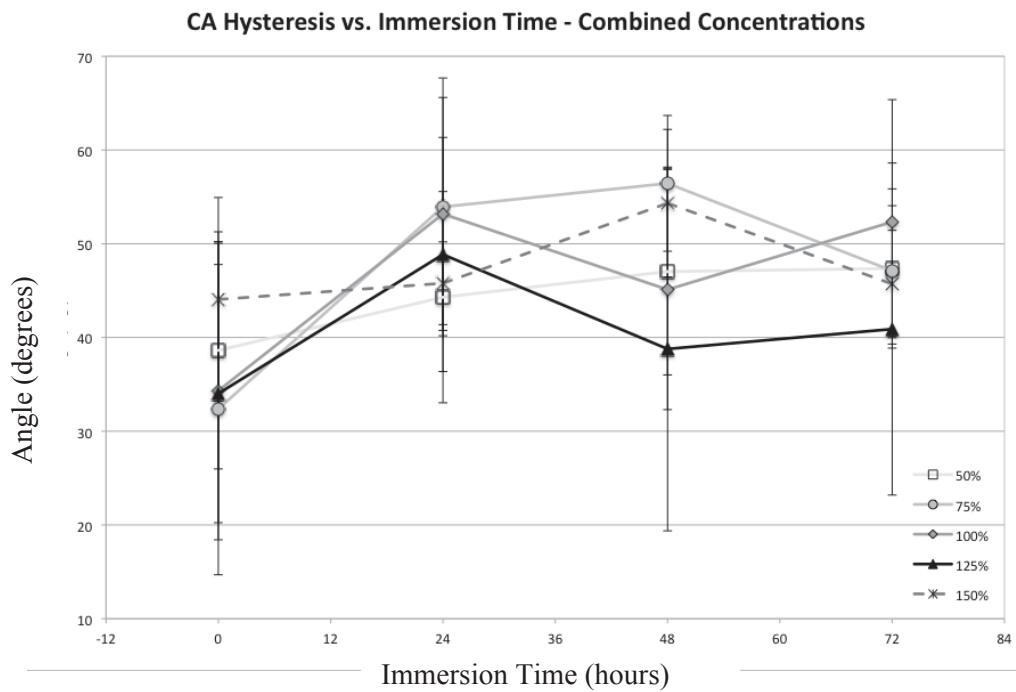


Figure 2-8: CA Hysteresis vs. immersion time for each solvent concentration.

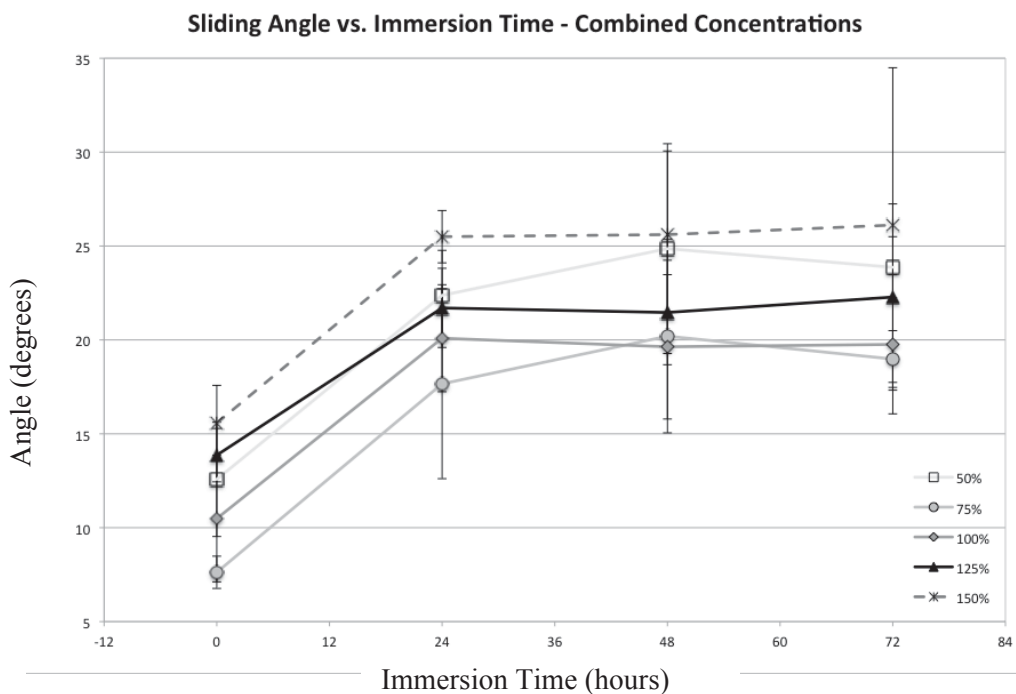
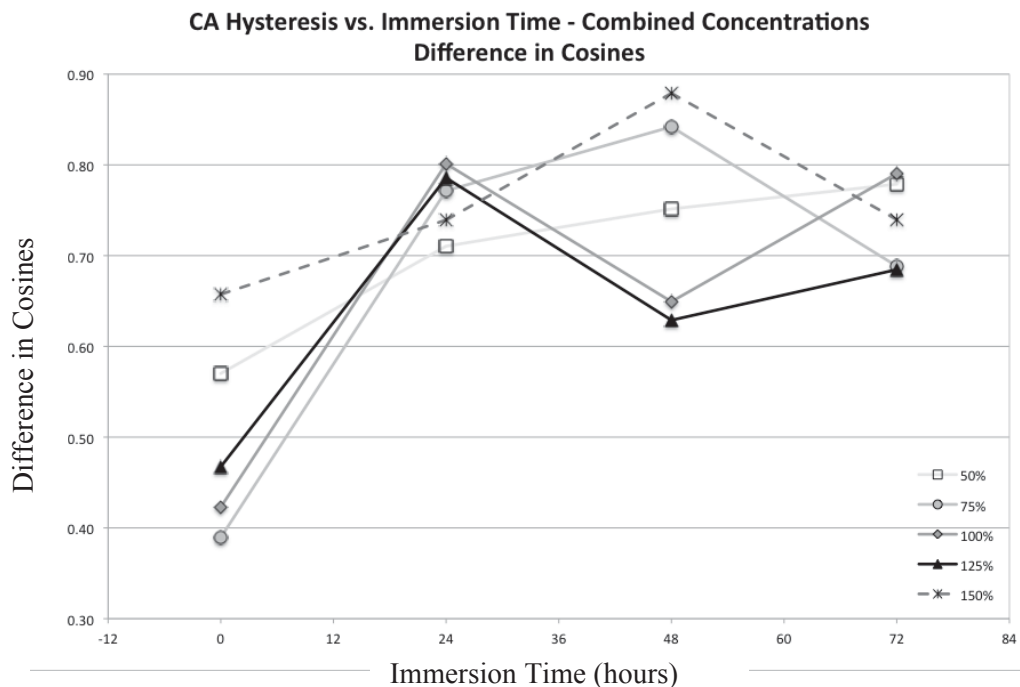


Figure 2-9: SA measurements vs. immersion time for each solvent concentration.



*Figure 2-10: CA Hysteresis (difference of cosines) vs. immersion time for each solvent concentration.*

The following pages contain the SEM images for the samples treated with the different solvent concentrations. Images were taken for the immersed and unimmersed portions of the sample (see Figure 2-1) such that a direct comparison could be made. Additionally, Figure 2-17 shows SEM images at 1000X and 5000X magnification of the  $\text{SiO}_2$  particles used to make the SH coating.

It can be seen from the images that the immersed and unimmersed portions are very similar. The only differences that can be currently pointed out are:

1. Connecting 'structures' between the coating's topography (for 50% solvent concentration) seem to have completely disconnected/broken after the prolonged water immersion (see 500X and 1000X images for 50% solvent concentration sample).
2. The apparent roughness of the coating film appears to be smoother after the immersion period. This is more evident on the 250X images for 100% (barely), 125% and 150% solvent concentrations. Such smoother topography is not evident in 50% and 75% solvent concentrations.
3. With increasing solvent concentration, there is also an increase in the formation of what appear to be pits in the coated film. Such pits appear to increase in number and size with increasing solvent concentration.

### 50% Solvent Concentration

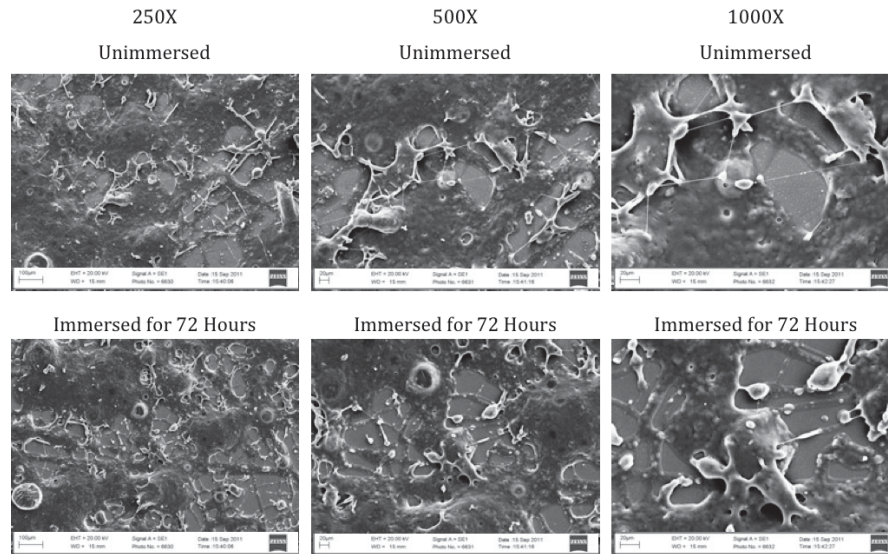


*Figure 2-11: SEM Images for 50% solvent concentration, before and after 72-hour immersion in water.*

### 75% Solvent Concentration

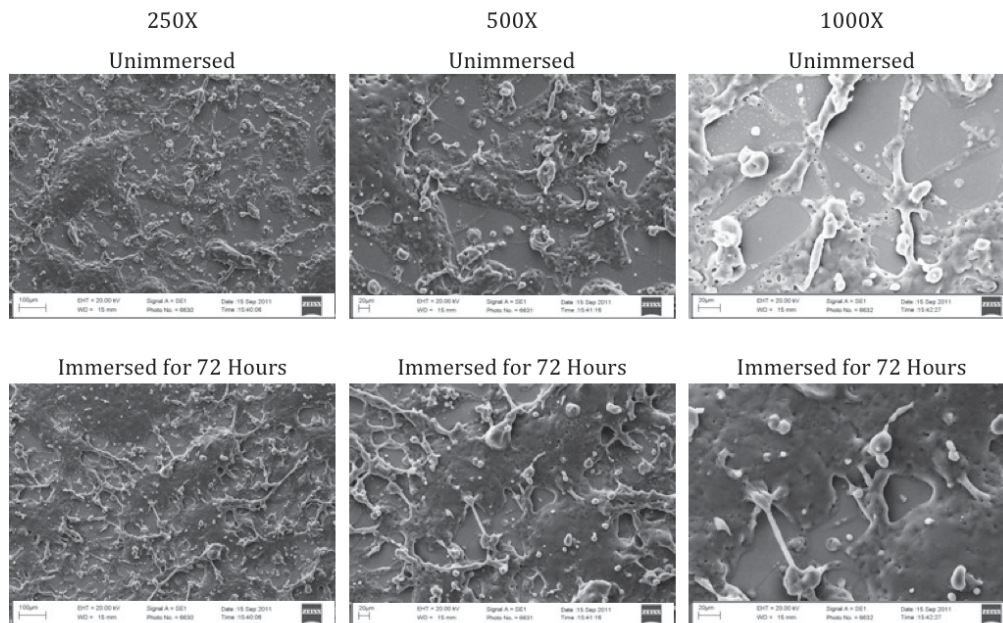


*Figure 2-12: SEM Images for 75% solvent concentration, before and after 72-hour immersion in water.*



### 100% Solvent Concentration

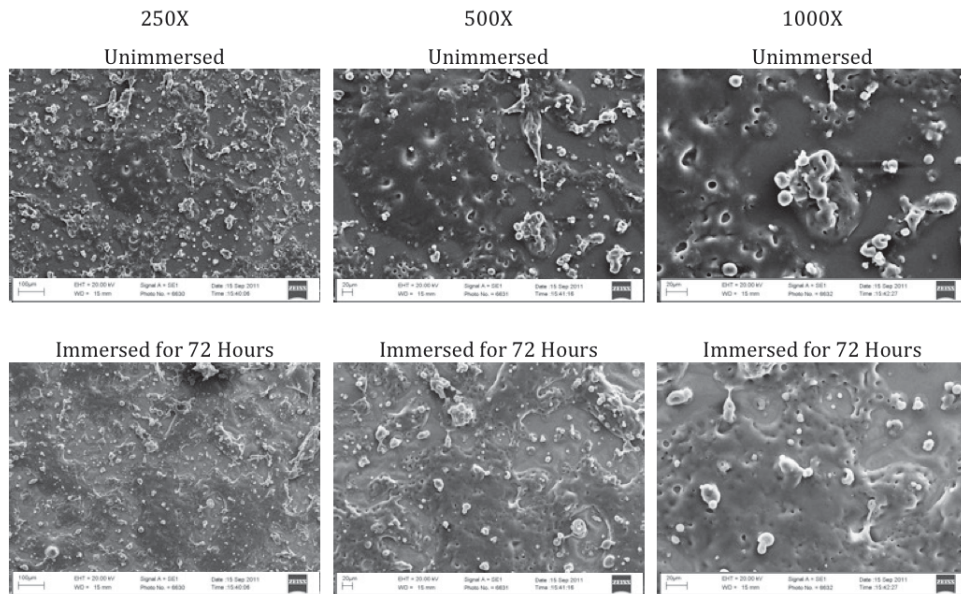


*Figure 2-13: SEM Images for 100% solvent concentration, before and after 72-hour immersion in water.*

### 125% Solvent Concentration

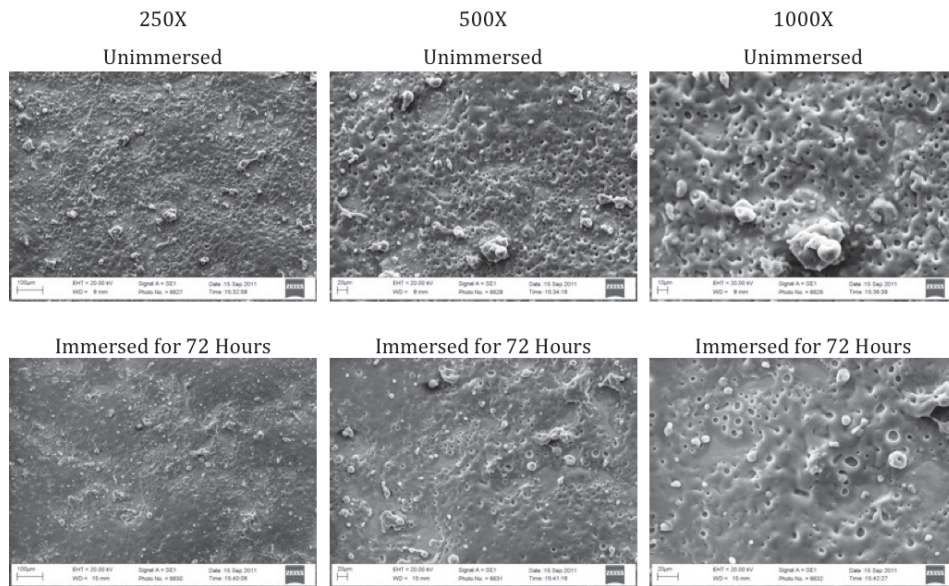


*Figure 2-14: SEM Images for 125% solvent concentration, before and after 72-hour immersion in water.*

### 150% Solvent Concentration

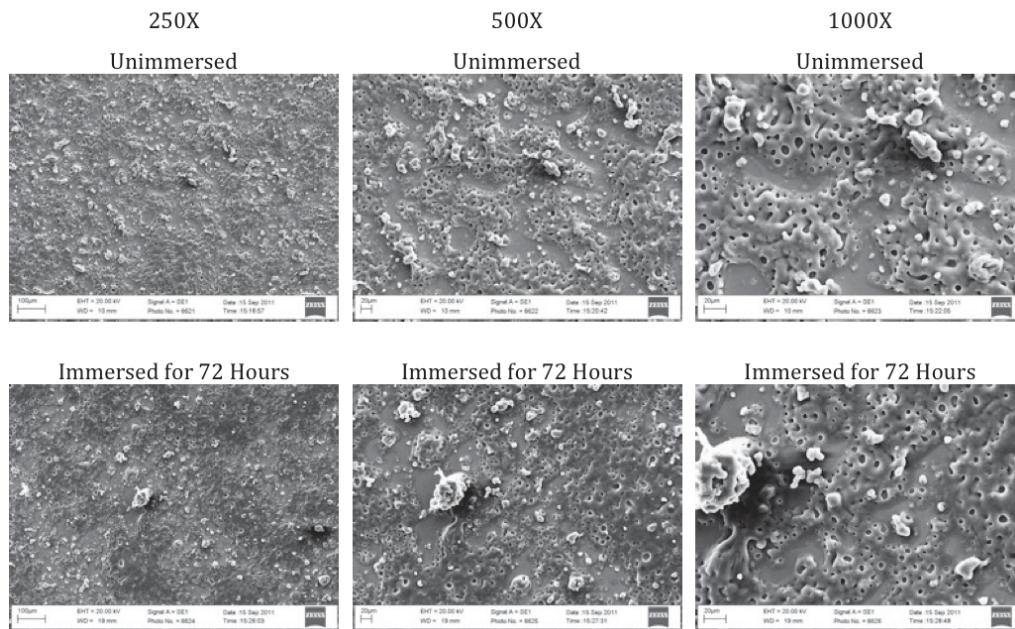
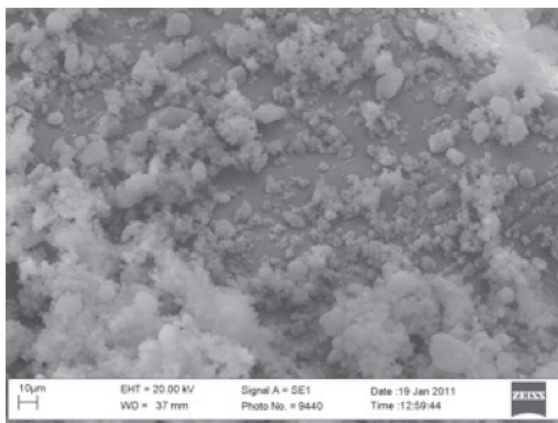


*Figure 2-15: SEM Images for 150% solvent concentration, before and after 72-hour immersion in water.*

### SiO<sub>2</sub> Particles

1000X



5000X

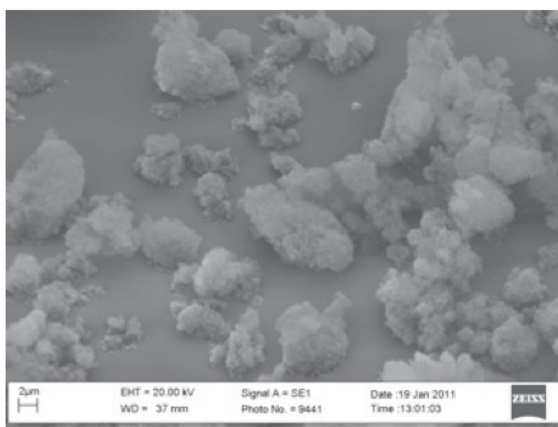


*Figure 2-16: SEM Images at 1000X and 5000X magnification of SiO<sub>2</sub> particles.*

### 2.3.2 Nanoparticle Concentration

The following figures contain the contact and sliding angle measurements for the samples treated with the different nanoparticle concentration batches (100%, 125%, 150%, 175% and 200%) for 75% solvent concentration. The following plots are:

- Figure 2-17: Combined plot of CA and SA for unimmersed
- Figure 2-18: Combined plot of CA and SA for samples immersed for 24 hours
- Figure 2-19: Combined plot of CA and SA for samples immersed for 48 hours
- Figure 2-20: Combined plot of CA and SA for samples immersed for 72 hours

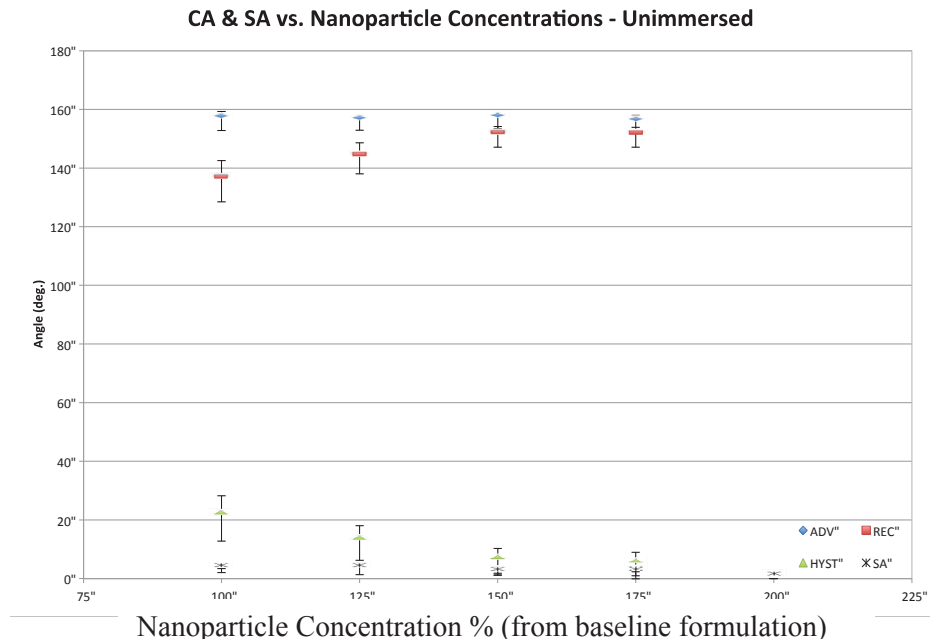


*Figure 2-17: CA and SA measurements vs. nanoparticle concentration for unimmersed samples. Due to increased viscosity, 200% nanoparticle concentration was impossible to spray with internal mixing airbrush. Plot clearly shows improved wetting performance with increasing nanoparticle concentration.*

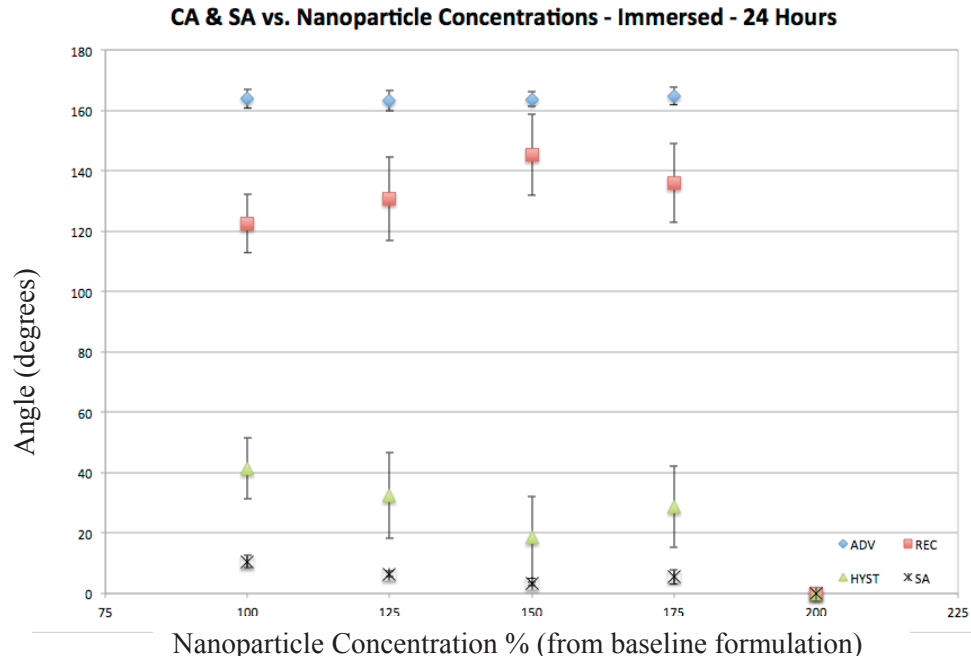


*Figure 2-18: CA and SA measurements vs. nanoparticle concentration for samples immersed for 24 hours. It can be seen that 150% nanoparticle concentration provides the best performance for this immersion period.*

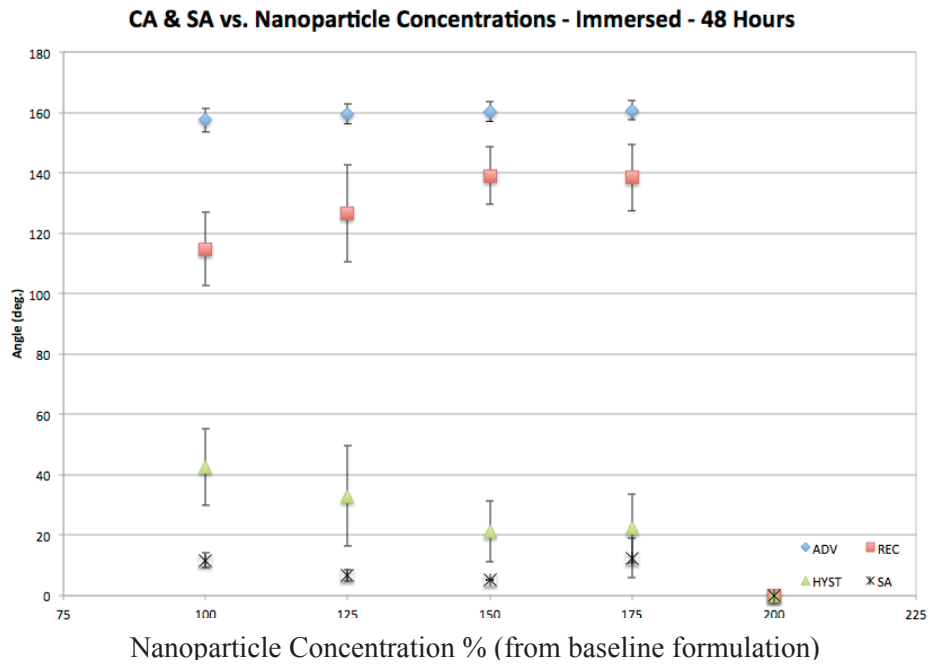


Figure 2-19: CA and SA measurements vs. nanoparticle concentration for samples immersed for 48 hours. It can be seen that 150% nanoparticle concentration still provides the best performance for this immersion period.

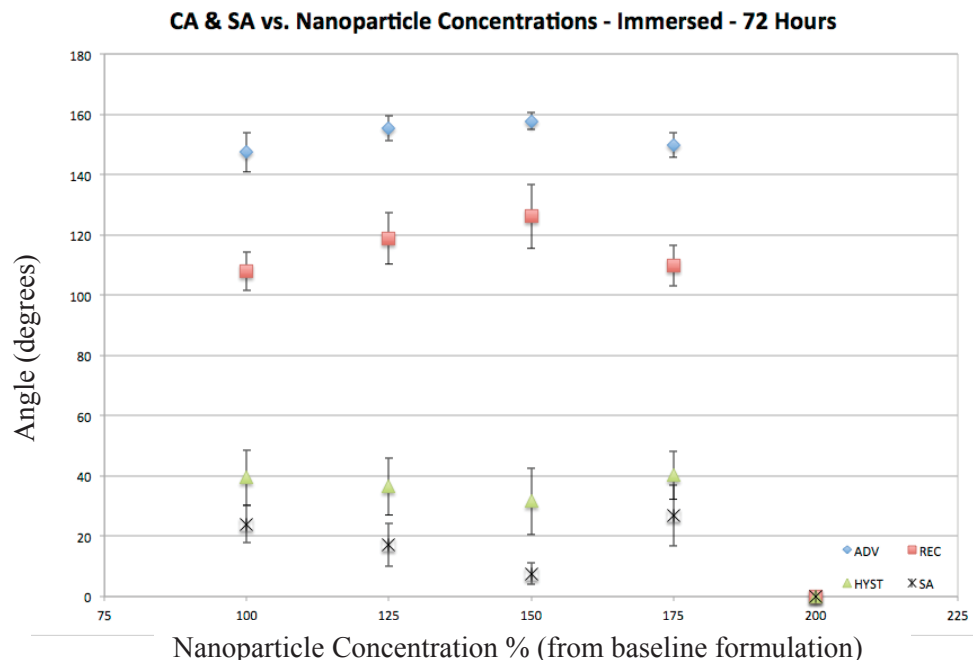


Figure 2-20: CA and SA measurements vs. nanoparticle concentration for samples immersed for 72 hours. It can be seen that 150% nanoparticle concentration provides the best performance overall.



The following figures show the CA and SA measurements plotted independently from each other with immersion time as the variable (i.e., contact angle vs. immersion time). Each plot is for a different angle measurement, showing its variation with immersion time and nanoparticle concentration (as compared to the baseline formulation) as follows:

- Figure 2-21: Advancing CA vs. Immersion Time for all nanoparticle concentrations.
- Figure 2-22: Receding CA vs. Immersion Time for all nanoparticle concentrations.
- Figure 2-23: CA Hysteresis vs. Immersion Time for all nanoparticle concentrations.
- Figure 2-24: SA vs. Immersion Time for all nanoparticle concentrations

It can be seen from the individual angle plots that 125% and 150% nanoparticle concentrations are the best performers (i.e., higher advancing and receding contact angles with lower sliding angles), after 72 hours of total immersion. 175% nanoparticle concentration showed excellent superhydrophobic performance for the first 24 to 48 hours, but quickly degraded to the performance of 100% nanoparticle concentration.

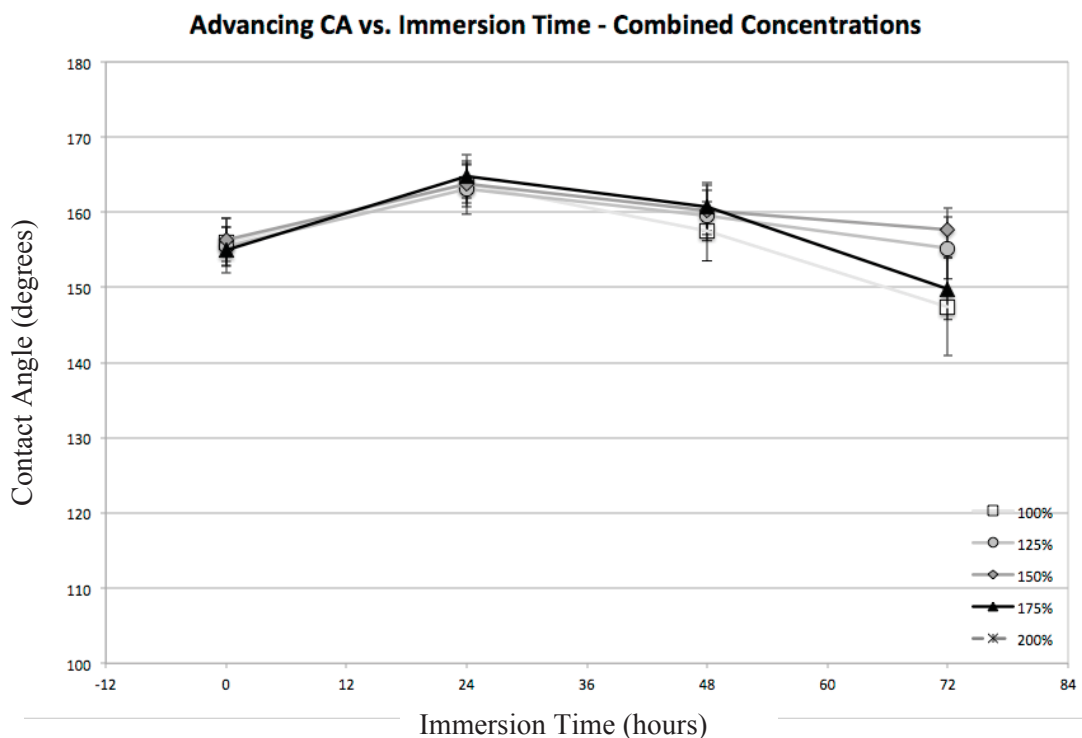


*Figure 2-21: Advancing CA vs Immersion Time for different nanoparticle concentrations. It can be seen from the plot that after 72 hours, 150% nanoparticle concentrations maintains the highest CA.*

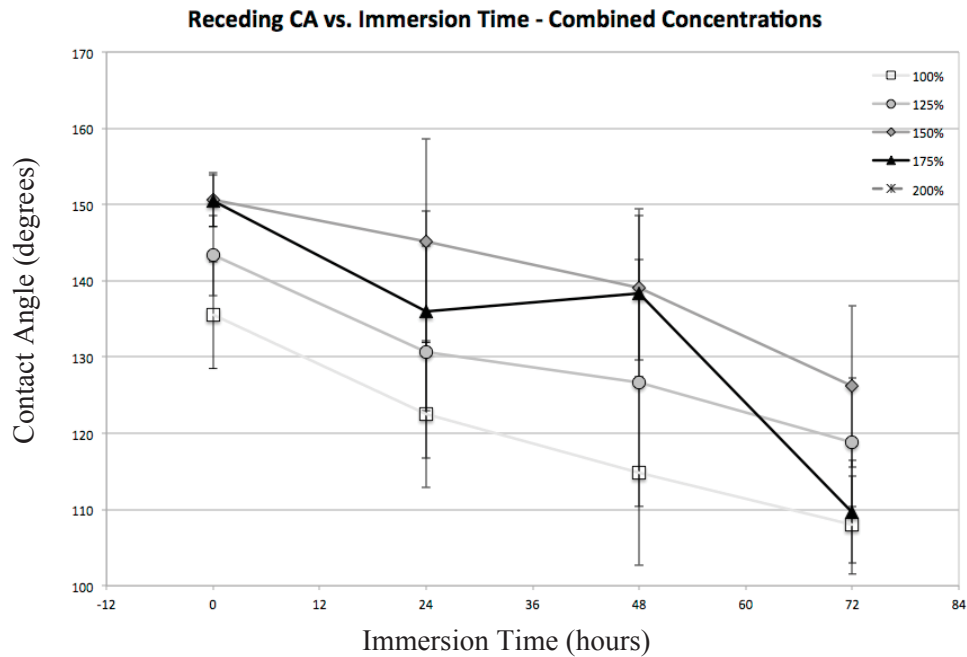


Figure 2-22: Receding CA vs Immersion Time for different nanoparticle concentrations. It can be seen from the plot that after 72 hours, 150% nanoparticle concentrations maintains the highest CA.

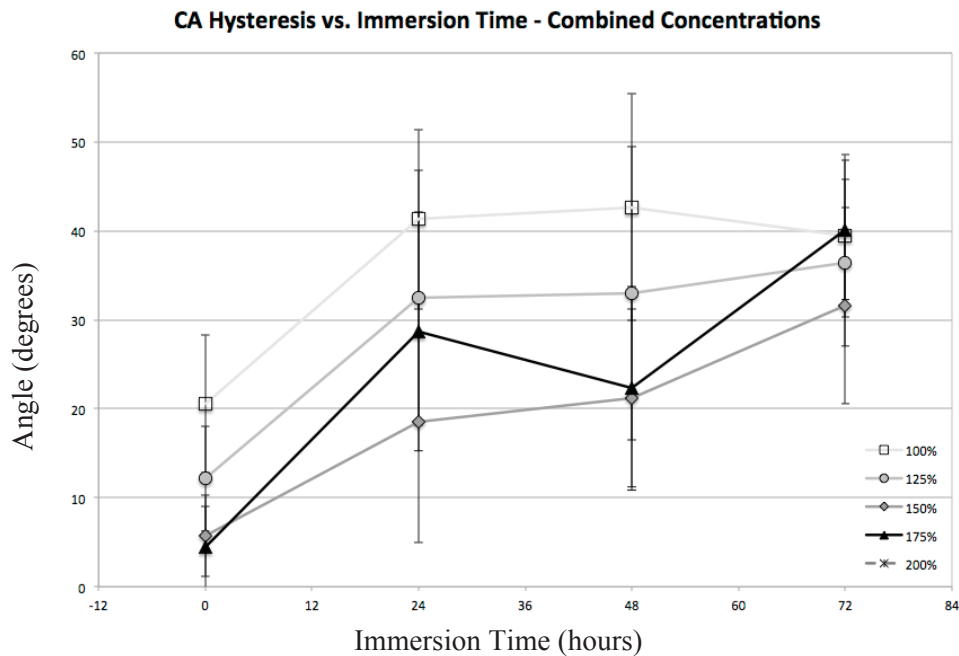


Figure 2-23: CA hysteresis vs Immersion Time for different nanoparticle concentrations. It can be seen from the plot that after 72 hours, 150% nanoparticle concentrations has the lowest hysteresis.

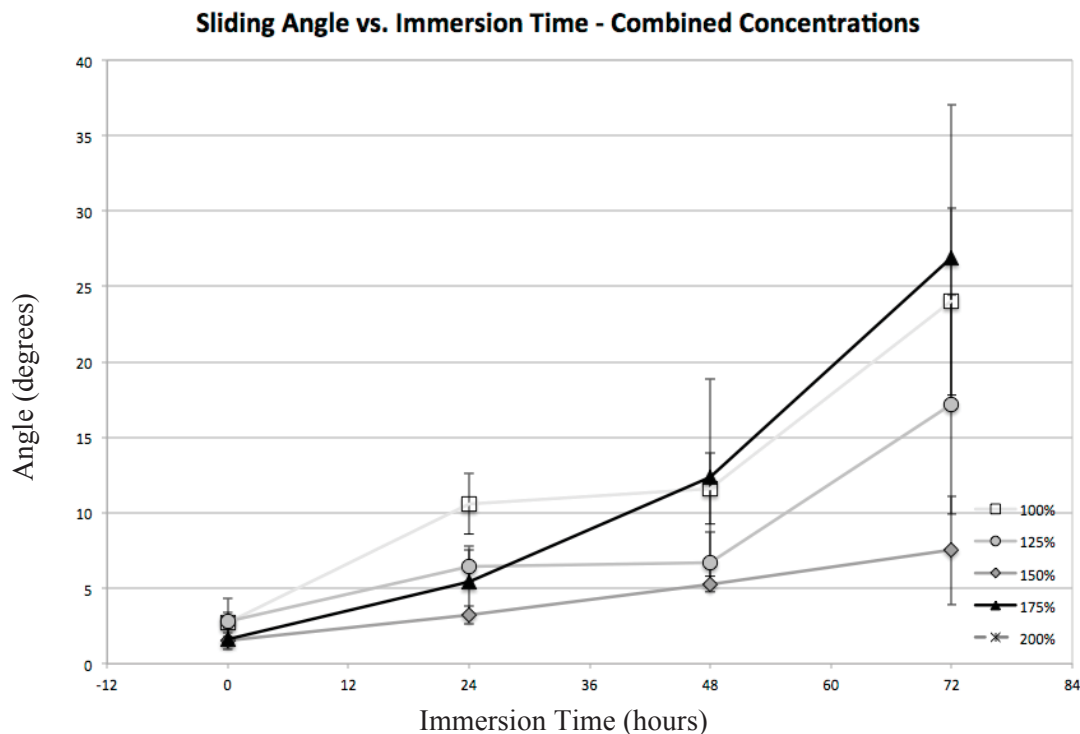


Figure 2-24: SA measurements vs Immersion Time for different nanoparticle concentrations. It can be seen from the plot that after 72 hours, 150% nanoparticle concentrations maintains the lowest SA.

It can be seen from these plots, that 150% nanoparticle concentrations provide the highest contact angles while at the same time the smallest sliding angle measurements (for 75% solvent concentration). While wetting performance improves with increased nanoparticle concentration, so does the coating's viscosity. Due to this increased viscosity, it was very difficult to spray the 175% nanoparticle concentration batch, and impossible to spray the 200% nanoparticle concentration batch (with internal mixing airbrush). Should these high nanoparticle concentrations be desired, we would have to look at advanced mixing or dispersing methods (i.e., utilizing probe sonicators) or alternate spraying systems (i.e., external mixing airbrushes). Nonetheless, from this optimization of the coating, 150% nanoparticle concentration provides excellent wetting properties and a very good balance between coating viscosity (i.e., ability to spray) and immersion durability, possibly reducing, the need to test higher nanoparticle concentrations.

### 2.3.3 Cross-Linker Concentration

The following figures show the CA measurements plotted independently from each other with cross-linker concentration as the variable for multiple (and cumulative) water immersion periods (measurements were made on samples coated only with the adhesive and cross-linker mix). Each plot is for a different angle measurement, showing its variation with cross-linker concentration as follows:



- Figure 2-25: Advancing CA for all cross-linker concentration and immersion periods.
- Figure 2-26: Receding CA for all cross-linker concentration and immersion periods.
- Figure 2-27: CA Hysteresis for all cross-linker concentration and immersion periods.

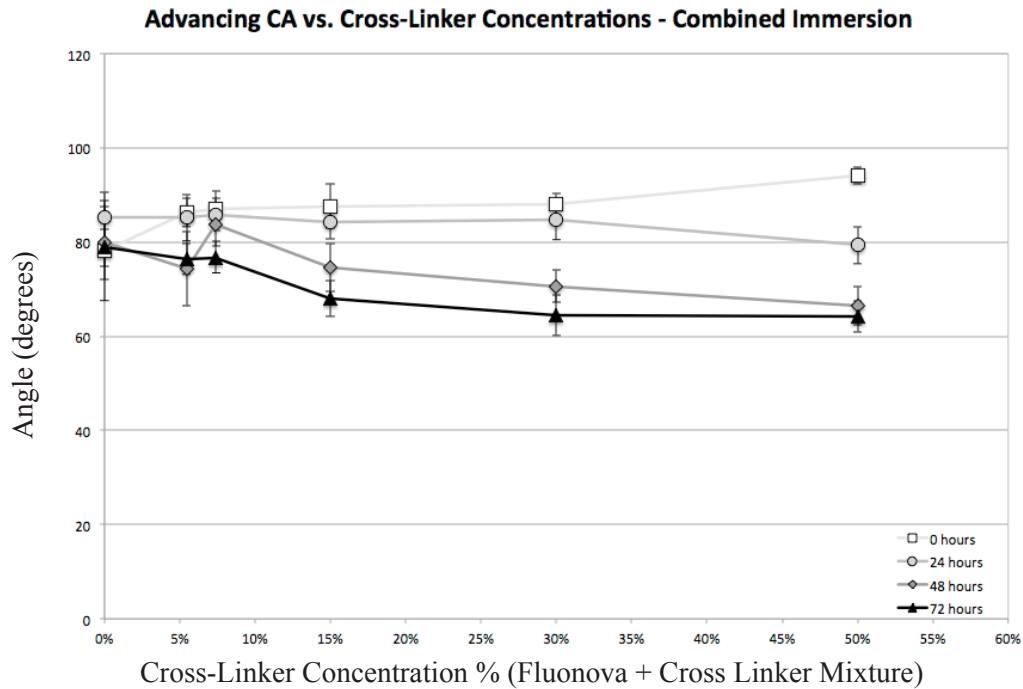


Figure 2-25: Advancing CA vs. Cross Linker concentration for different cumulative immersion periods. It can be seen from the plot that concentrations up to 7.4% maintain the highest CA.

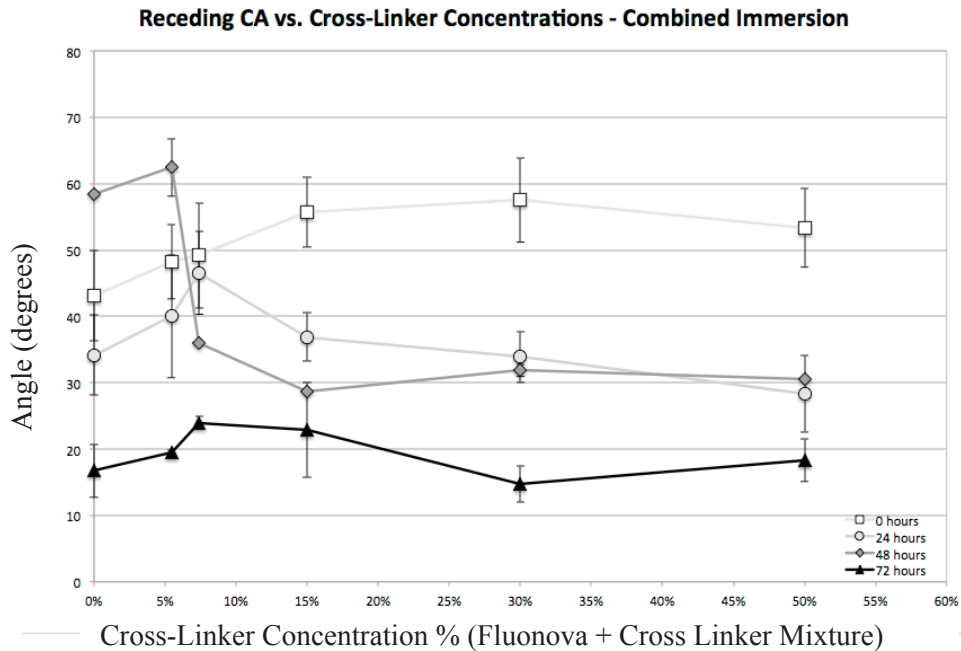


Figure 2-26: Receding CA vs. Cross Linker concentration for different cumulative immersion periods. It can be seen from the plot that 7.4% concentration shows the smallest change between any immersion period (i.e., maximum change/difference is between 0 hrs and 72 hrs).

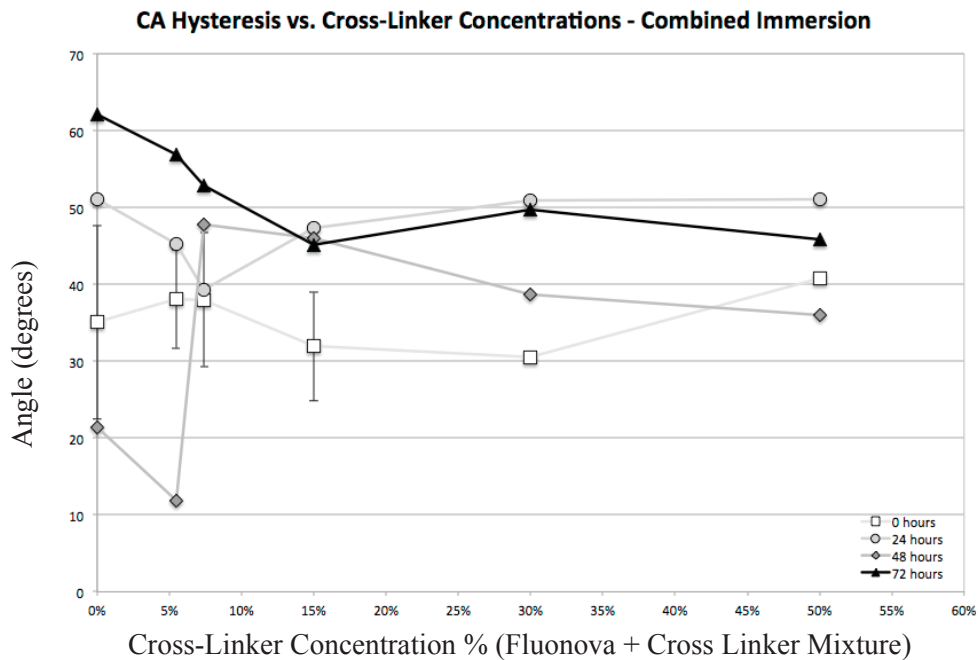


Figure 2-27: CA Hysteresis vs. Cross Linker concentration for different cumulative immersion periods. It can be seen from the plot that 7.4% concentration shows the smallest change between any immersion period (i.e., maximum change/difference, between 0 hrs and 72 hrs, is 14.85°).

It can be seen in the three plots that 7.4% cross-linker concentration (manufacturer's recommendation) results in the best wetting performance for a total immersion period of 72 hours. While advancing and receding CAs may be higher for different concentrations, their overall change with increased immersion time is smallest at 7.4%.

## **2.4 Conclusions**

All coatings tested still show susceptibility to prolonged water immersion; however, it is clearly demonstrated that using the correct solvent, nanoparticle, and cross-linker concentrations would maximize a coating's wetting performance over what was achieved in the previous reporting periods. This wetting performance improvement could also result in durability improvements when subject to prolonged immersion in water.

It has been shown with that solvent concentrations between 75% and 100%, nanoparticle concentrations between 125% and 150% and cross-linker to fluoropolymer concentrations between 5.44% and 7.4% provide the best coating performance results (under the current testing). Although the optimum may exist at intermediate concentrations (solvent and/or nanoparticles), it is recommended that for future work one to use:

- Solvent concentrations of 75%.
- Nanoparticle concentrations of 150%.
- Cross-linker concentration of 7.4% (of 4FVBA Fluonova and cross-linker mixture).

Additional improvements to the coating's performance may also be achieved by optimizing the total adhesive concentration (pending) and/or by using different components (part of an ongoing investigation).

### 3 Wetting Performance of Worn Superhydrophobic Surfaces

---

The results of wearing superhydrophobic surfaces and its effect on roughness parameters, surface properties and wetting behavior have been studied over the last 3 years. An abrasive wear device has been set up to allow consistency, reproducibility and precise control over the amount of wear desired on a surface. Based on the results obtained, relationships in the trends observed with the different roughness parameters and wetting behaviour have been established. In some cases the relationships are strong (roughness parameters  $R_{sk}$ ,  $S_{sk}$ ,  $r$ )<sup>32</sup> while in other cases, the relationships are weak (roughness parameters  $R_a$ ,  $R_q$ ,  $R_z$ )<sup>32</sup> and are unable to capture the different transitions in wetting. It has also been determined that different roughness scales present on a surface wear differently and require separate attention. The following summarize the accomplishments reached as part of this study:

- An abrasion methodology for superhydrophobic surfaces has been developed, for generating random, repeatable, and controlled wear on surfaces without any surface contamination.
- A methodology has been developed to map surface topography helping in elucidation of surface topography descriptors.
- Generation of a noise removal methodology to eliminate artifacts in surface topography data, for physical reality to match mapped surface topography data.
- Successful calculation of Cassie Equation parameters on both surface and linear density basis, and hence water penetration depths, on superhydrophobic surfaces.
- Demonstrating the difference between the original Cassie Equation and the “popular” Cassie Equation, and how the “popular” Cassie Equation can be used to predict advancing contact angles on superhydrophobic surfaces.
- Fabrication of regular geometry cylindrical pillars with hemispherical domes.

#### 3.1 Introduction

Superhydrophobic surfaces (SHS) are extremely water repellent surfaces having low water roll off angles. Quantitative characterization is done by measuring equilibrium contact angle (CA) and hysteresis (difference between advancing CA and receding CA). Equilibrium CA should be greater than 150° and hysteresis less than 10° for a surface to be SHS.

Cassie – Baxter equation,<sup>6</sup> can predict CA ( $\theta_c$ ) on SHS (Equation 3-1).

$$\cos \theta_c = f_1 \cos \theta_1 + f_2 \cos \theta_2 \quad (3-1)$$

Here,  $f_1$  and  $f_2$  denote total area fraction of material 1 and 2.  $\theta_1$  and  $\theta_2$  are the CAs on the smooth surface of material 1 and material 2 respectively. For a case where air is entrapped in hierarchical structures of a SHS as illustrated in Figure 3-1, Equation 3-1 reduces to Equation 3-2.

$$\cos \theta_c = f_1 \cos \theta_1 + f_2 \quad (3-2)$$

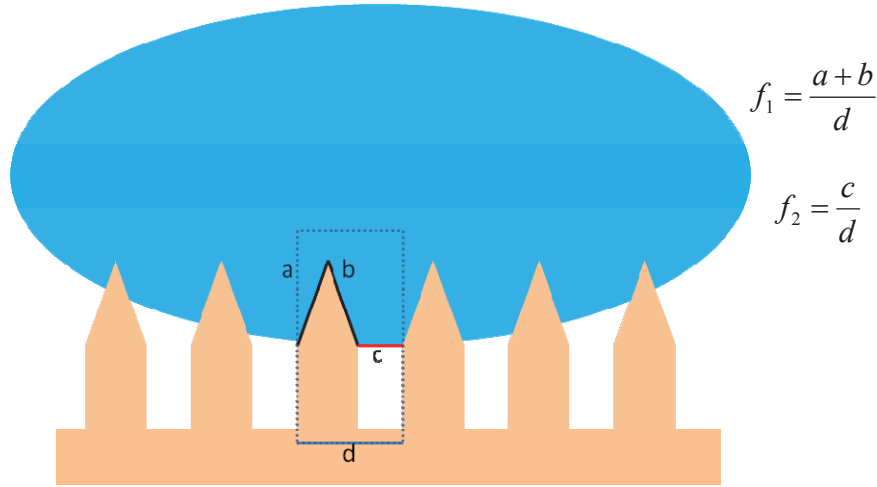


*Figure 3-1: Illustration showing water drop resting on a superhydrophobic surface. Also, it is shown how the parameters  $f_1$  and  $f_2$ , used in the Cassie Equation (3-1), are defined and calculated.*

To predict contact angles, area fraction of air-solid interface ( $f_1$ ) and liquid- air interface ( $f_2$ ) must be known. Presently, calculations of theoretical Cassie angles assume that the drop is in “perfect” fakir state (i.e., no liquid penetrates into asperities) and not in a composite state involving partial penetration into the asperities. This assumption does not hold true on surfaces which deviate from flat top geometry e.g., pyramid, hemispherical top, conical needles, where water will partially impregnate the surface. Developing a methodology to calculate various area fractions ( $f_1$ ,  $f_2$ ) assumes more significance in these cases to be able to predict CAs with a degree of confidence.

The limitation of the Cassie equation is that it does not take contact angle hysteresis (CAH) into account and only predicts equilibrium CA. This presents a hindrance as adhesive behaviour (CAH) of the drop, essential for superhydrophobicity, cannot be predicted. But, to further the research in this field it is important to study surface roughness as it is a prime factor in imparting superhydrophobicity. Studying surface roughness will help in finding surface parameters that can predict adhesion and mobility of a drop on a surface, which in turn will help in designing durable superhydrophobic surfaces. Hence, a methodology is needed to map topography of a superhydrophobic surface.

Confocal scanning microscopy (CSM) is one such technique which allows for non-intrusive spatial resolution of surface topography. Confocal microscopy is a non-contact profilometry technique that can map surface features. Used in conjunction with a water immersion objective, features wetted by water can be resolved which in turn can be used to elucidate parameters  $f_1$  and  $f_2$ . This methodology, of finding surface parameters with help of CSM, will help in predicting CAs using the Cassie equation with a high degree of confidence relative to existing methodologies.

### 3.1.1 Literature Review

In the literature there is some work on using CSM to map surface topography of SHS. D'Acunzi et al.<sup>7</sup> used white light confocal microscope to quantify roughness of the SHS fabricated by sedimenting colloidal silica raspberry particles (1  $\mu\text{m}$  diameter) dispersed in water. The evaporation temperature of water was varied from 25°C to 90° C, this induced convection in water resulting in inhomogeneous topography of colloidal particles. The resulting SHS were scanned by white light CSM and average roughness was measured by dividing the  $800 \times 800 \mu\text{m}^2$  area into smaller squares of  $50 \mu\text{m} \times 50 \mu\text{m}$ .

Luo et al.<sup>8</sup> imaged the water-air interface on a superhydrophobic lotus leaf with help of confocal laser scanning microscope (CLSM). A 10  $\mu\text{l}$  drop of water was deposited on a lotus leaf, and a laser of 408 nm wavelength was used to image the water-air interface from top. It is pertinent to mention here that the objective is imaging the water drop from the air medium, and is not immersed in water. Using CLSM, Luo et al.<sup>8</sup> established that the lotus leaf was in Cassie state with air cushion thickness estimated to be between 10-15  $\mu\text{m}$ .

Wu et al.<sup>9</sup> measured local CA on a flat glass surface containing homogeneously distributed hydrophilic and hydrophobic regions. Rhodamine-B dye was dispersed in water (7 mg/L), and a 3D projection of the water drop was obtained using CLSM. Local CA were measured using geometrical methods by drawing a tangent to the baseline of the drop.

In all, confocal scanning microscopy has been shown to be successful in mapping surface topography and water penetration on SHS. It has been shown to be successful in calculating related parameters (Local CA, average roughness etc.) too. For this reason, the feasibility of using CSM to map underwater surface topography and finding out related surface parameters is the ambit of this report.

### 3.1.2 Motivation of the Study

Predicting wetting behaviour on SHS is of importance to industry to further the applications of SHS, and to academia to further the fundamental studies on SHS. Wetting behaviour can be predicted by studying surface topography of a SHS and delineating various associated surface parameters. A methodology to calculate these parameters would advance the fundamental study on durability of SHS. This would motivate industrial applications of SHS, widening the scope of the field. Further, various surface descriptors computed through mapping the topography are studied and evaluated.

The scope and purpose of this study is evaluating feasibility of confocal scanning microscopy as one such suitable technique to map and describe surface topography of SHS on widest range of surface topographies possible.

## 3.2 Experimental Section

Plasma etched Polytetrafluoroethylene (PTFE) SHS used in this study have been described in detail elsewhere,<sup>10</sup> and they have needle-like structures with random geometry as shown in Figure 3-2. The experimental conditions used in plasma etching chemically affected PTFE to a very minor degree.<sup>10</sup>

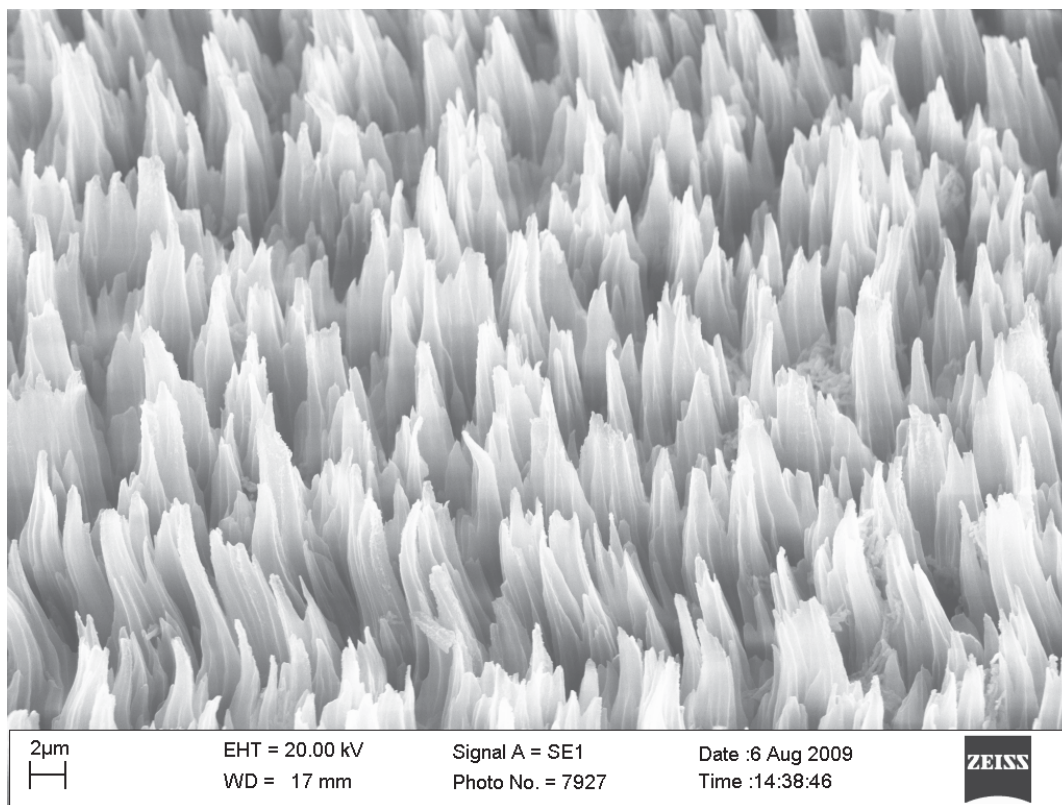


*Figure 3-2: SEM of unworn plasma etched Teflon.*

A gyratory shaker was used to abrade the surface with the help of  $\frac{1}{2}$  mm glass beads. The experiment was designed under standard test similar to specification ASTM F735-06 (Standard Test Method for Abrasion Resistance of Transparent Plastics and Coatings using the Oscillating Sand Method).<sup>11</sup> Samples were placed flat at the bottom of the gyratory shaker while 2L of glass beads, used as abrading material, cover the samples fully. The circular motion of the gyratory shaker abrades the samples in random fashion. This method of abrasion is repeatable, producing controlled wear on a surface, with little to no contamination of samples, and it produces a random wear pattern, and different abrading materials can be chosen. The SHS surface was worn down in varying intervals of three minutes at 250 rpm on a gyratory shaker.

After each wear interval, an abraded SHS was cleaned by sonication in ethanol to get rid of any contaminants on the sample surface. Surface topography and surface descriptors of the samples were then resolved with Carl Zeiss Axio-700 Confocal Scanning Microscope (CSM). A 100x objective lens, with an image field of  $117 \times 94 \mu\text{m}$  and  $0.16 \mu\text{m}$  lateral resolution was used for all the samples. Contact angles were always measured with de-ionised water using the sessile drop method. Water was pumped into the drop at the rate of  $0.5 \mu\text{L/s}$ , and advancing CA were measured at intervals of one second as the drop volume increased from  $20 \mu\text{L}$  to  $60 \mu\text{L}$ . The advancing angle was then averaged over all the advancing CA measured. Water was then removed at rate of  $0.5 \mu\text{L/s}$  from this  $60 \mu\text{L}$  volume water drop till it reached a volume of  $20 \mu\text{L}$ ; receding CA were measured at intervals of one second. Receding CA were then the average of all the individual receding CA measured. Surface imaging was done by SEM (Carl Zeiss LEO 1430).



Before taking SEM images, a gold layer of 10 nm was deposited on the sample surface. Care was taken such that CSM, SEM and CA were all measured on the same position on the sample; this ensured that the parameters (surface descriptors, wetting characteristics) collected through each measurement (CSM, SEM, and CA) were correlated and representative of each other.

### **3.2.1 Fabricating Pillars with Flat Tops**

Photoresist AZ P4620 (AZ Electronic Materials USA Corp., Somerville, NJ, USA) was poured in the silicon master shown in Figure 3-3 (a). Sylgard 184 PDMS (Dow Corning, Midland, MI) was mixed in a 10:1 (pre-polymer/cross-linker) ratio. After removal of air bubbles formed during mixing, the viscous liquid was poured onto the AZ P4620 master and cured at 70 °C for 7 hours and removed from the mould. The final shape of the PDMS pillars is shown in Figure 3-3 (b). Figure 3-3 shows SEM images of the silicon mould used and various fabricated pillars.

10:1 PDMS was poured into the silicon master shown in Figure 3-3 (a) and allowed to curing for 7 hours at 70° C. AZ P4620 was poured into this PDMS negative mask and removed from the mould after four hours. These photoresist pillars were then placed upside down in oven at 143° C for six minutes. The hemispherical dome shaped cylindrical pillars are shown in Figure 3-3 (c).



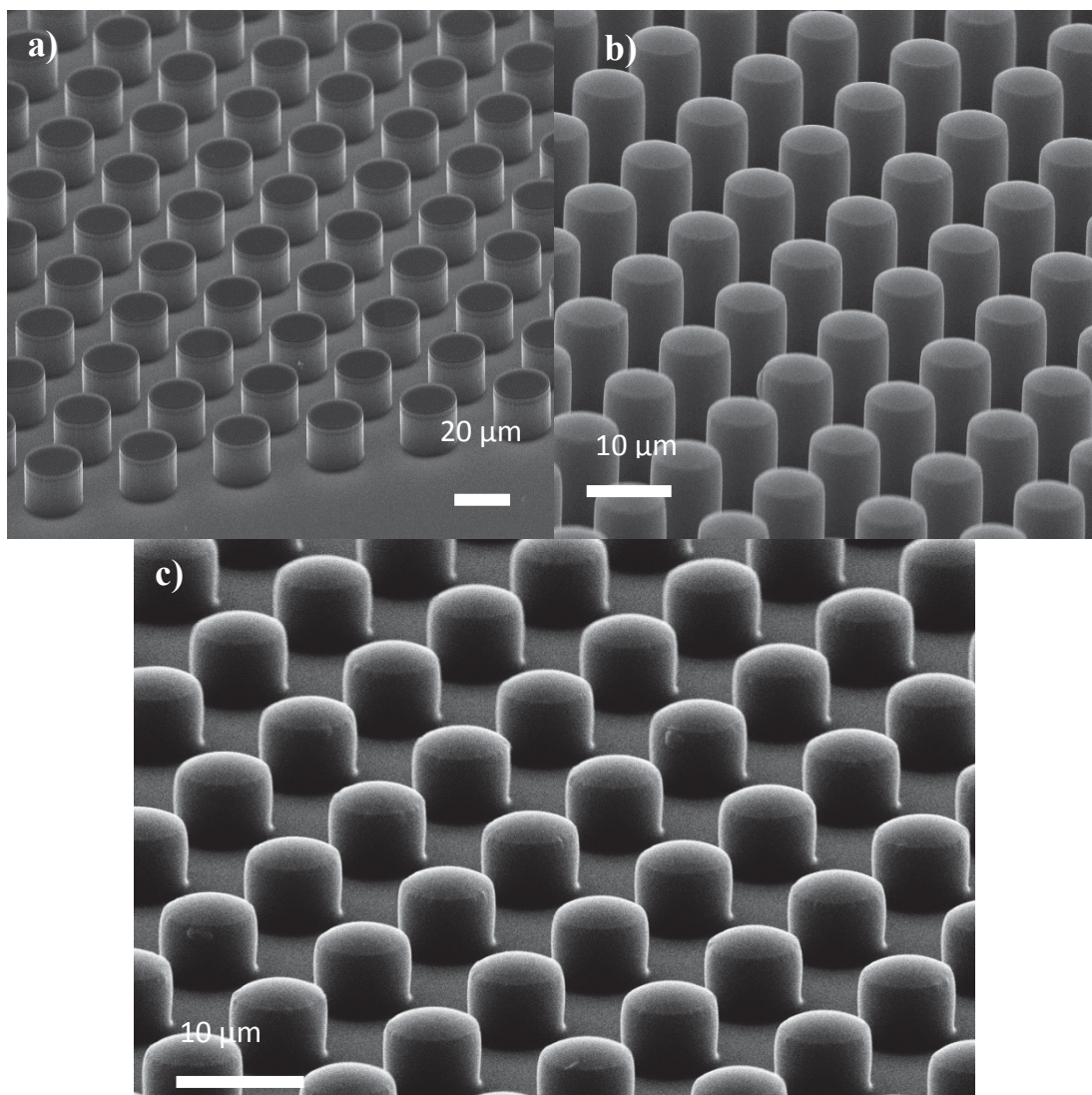


*Figure 3-3: a) SEM image of silanized Si cylindrical flat-top pillars arranged in a rectangular unit cell. b) PDMS pillars fabricated by making a double negative of the pillars shown in Figure a), c) AZ P4620 hemispherical dome cylindrical pillars.*

### 3.3 Results and Discussion

#### 3.3.1 Use of White Light Confocal Microscope in Imaging the Water-Air Interface

SHS investigated in this report were PDMS cylindrical pillars arranged in a rectangular lattice; the SEM image is shown in Figure 3-3 (b). The pillars had flat tops, and the CSM line profile taken with a 20x objective is shown in Figure 3-4. The pillar dimensions are 10 μm in height, cylinder diameter of 8 μm, and the centre to centre pillar distance is 15 μm.

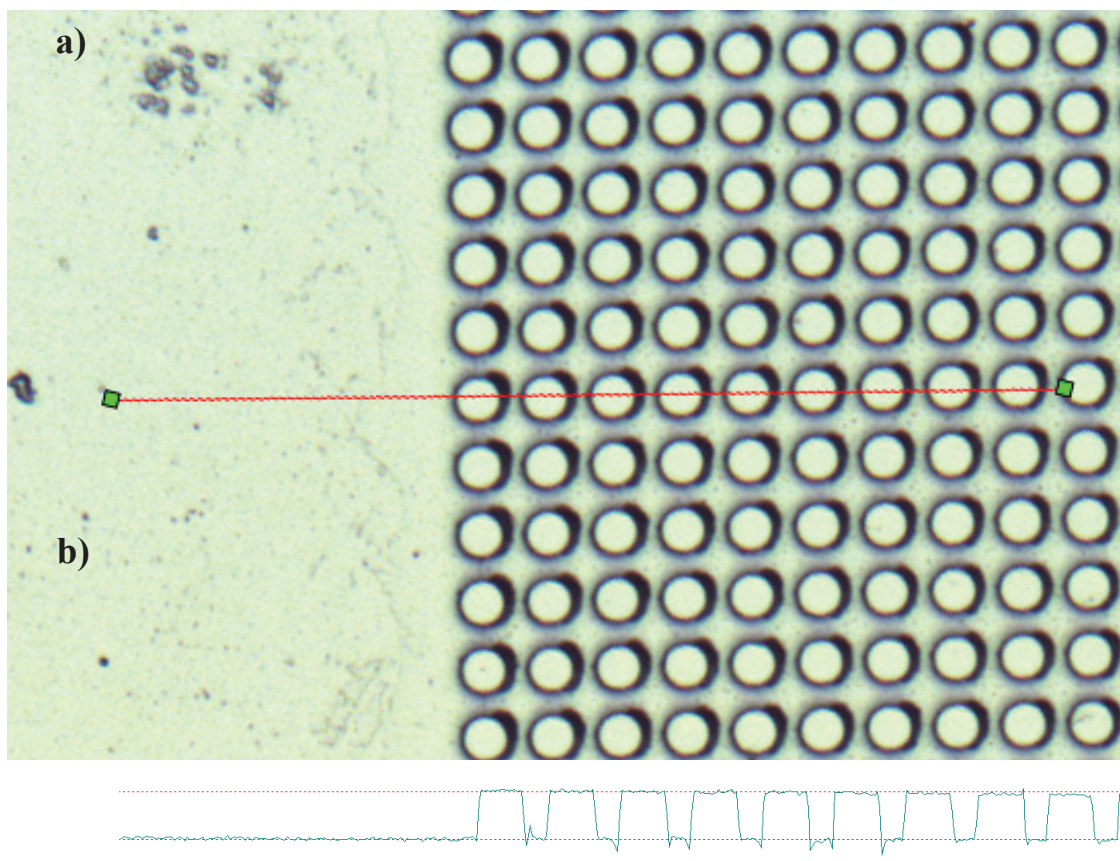


*Figure 3-4: a) CSM “all-in-focus” image of the PDMS superhydrophobic structure with cylindrical flat-top pillars arranged in a rectangular unit cell. b) height profile of the above pillars taken on as denoted by red line in above figure. Pillar height is 10  $\mu\text{m}$ , and their diameter is 8  $\mu\text{m}$  with a centre-to-centre pillar distance of 15  $\mu\text{m}$ .*

The SHS surface was placed in a Petri dish so that the PDMS surface rests on bottom of the dish and immersed in water of roughly 1 mm depth, Figure 3-5. A water immersion objective with 20x magnification was used in subsequent experiments.

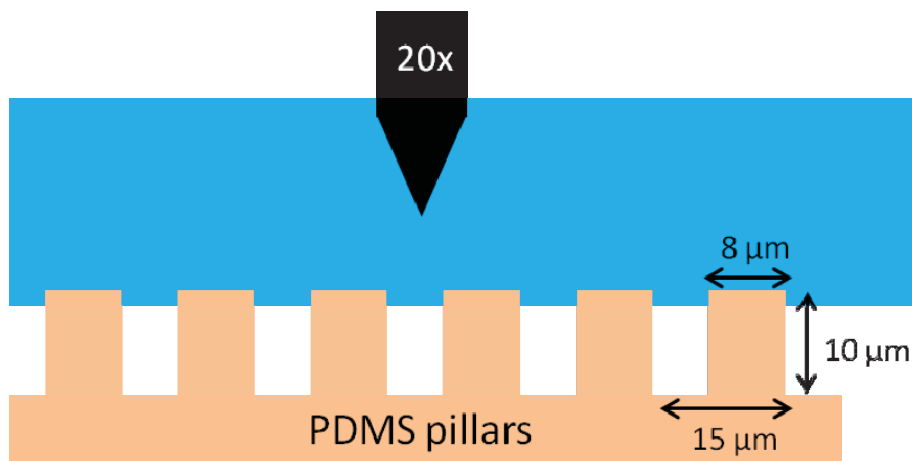


*Figure 3-5: Schematic showing the set-up for imaging the water-air interface on PDMS cylindrical pillar substrate. The SHS is placed in a Petri dish, which is subsequently filled with water just until the SHS is fully covered in water. A water immersion objective with 20x magnification is used to image the surface topography. White areas indicate air.*

Figure 3-5 shows the schematic of the experimental set-up. Local thermal heating by white light used in the experiment can affect the water-air interface, as heating can induce local surface tension changes in the water thereby changing the local wetting profile. To prevent this, a scan was completed within an average time of 30 seconds, and a spot was scanned only once. These factors were helpful in ensuring that sample is not heated up by white light, and thus no effect of local heating due to white light on wetting profile was assumed.

Also, scanning was done near the edges as it would provide a reference for the pillar bases, as all of the substrate is coplanar.

A possible shape of the interface is shown in Figure 3-6. PDMS is an intrinsically low surface energy polymer. Air pockets can be formed over pillar tops, and near the pillar edges there can also be a discontinuity, with water not hugging the PDMS surface and instead forming a parabolic meniscus as illustrated in Figure 3-6.

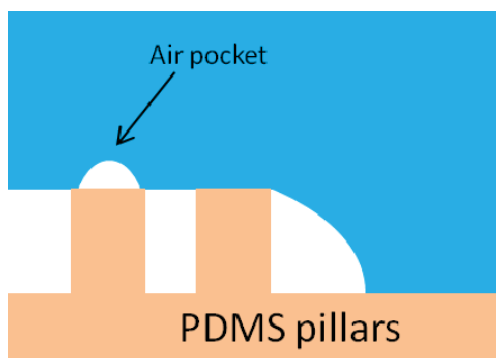


*Figure 3-6: Possible shape of the interface near pillar boundaries and over the pillar tops. The boundary pillar without the air pocket on top demonstrates another possible interface.*



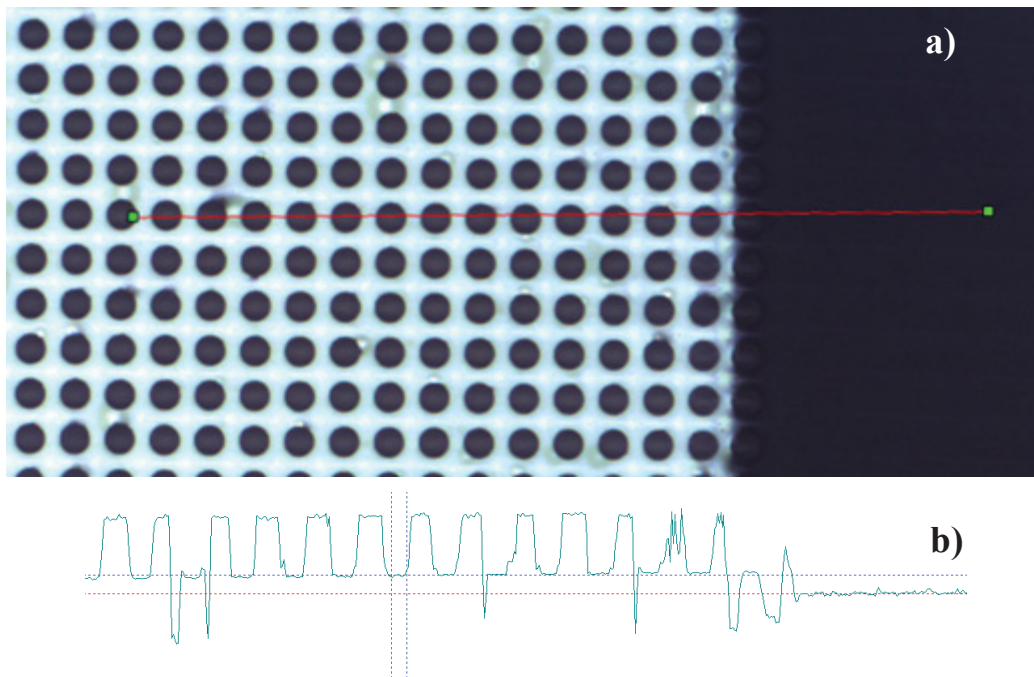


*Figure 3-7: a) CSM image of the PDMS SHS surface immersed under water. On the right is the smooth PDMS surface base acting as a reference. b) Line profile of the immersed SHS, taken along the red line depicted in a). It can be seen that the pillar on the edge has not been imaged correctly. Also, the rest of the pillars have been elevated by a certain degree which in reality should be aligned with the smooth PDMS surface.*

Figure 3-7 shows a CSM image and a line profile taken on one spot on the sample near pillar edges. The PDMS pillar-containing area is bright in contrast to the smooth PDMS, suggesting that the water is either in a complete Cassie or composite Cassie state (i.e., with air completely or partially trapped in the pillar array). Also the top of the pillars are dark suggesting that water is hugging the top of the pillars and not forming air pockets over them.

The change in color is due to very low reflection intensity from the PDMS-water interface. The intensity of the reflected light, at normal incidence, depends upon the reflection coefficient given by,  $(n-1)^2 / (n+1)^2$ . Here,  $n$  is the ratio of the refractive indices of the respective components in contact. This difference is large for the water-air interface and small for the water-PDMS surface as  $n_{air}=1$ ,  $n_{water} = 1.33$  and  $n_{PDMS} = 1.45$ .

The height profile near the pillar boundary is not clear in elucidating the topographical features and the boundary-edge pillar is imaged as submerged into the PDMS surface, which was not possible as ascertained by SEM. From Figure 3-7 (a) there is no evidence suggesting a bright field, which would be proof of entrapped air acting as a surface to reflect-back light. Hence the immersion of the edge pillar is not an artefact due to CSM light rays reflecting through different media.

The pillar base is also elevated from the smooth PDMS surface; in reality both should be aligned. This can be due to the air-water interface acting as a mirror, giving the illusion of a raised pillar base. The raised base of pillars appears to be roughly  $3.6\text{ }\mu\text{m}$  above the actual smooth base surface. If we assume this to be the water-air interface, it is highly unlikely that water has penetrated almost  $6\text{ }\mu\text{m}$  considering that the water level is barely enough to submerge the SHS. It is likely that the reflection, from the PDMS surface and sagging water-air interface, is acting as a mirror/lens and is interfering and giving rise to an illusion of a raised pillar base.

The reasons for the pillar base elevation and the boundary pillar being submerged are yet unknown. Supposing the boundary pillars are all submerged in water, the imaging should not show them as embedded into the surface, instead they should be aligned with the smooth surface. It should be noted that besides these anomalies, the pillar profiles are uniformly consistent.

From this experiment no inference can be made about the location of the water-air interface, and no plausible explanation can be offered for the anomalies present in the CSM imaging near the pillar boundary and elevated pillar base.

While the experiment was in process, one of the regions transitioned into the Wenzel regime (full liquid penetration into the asperities), as signified by the change in the color in Figure 3-8. The height profile on the smooth PDMS surface was taken to be our reference point. On moving into the pillars which are in the Wenzel regime, the pillar base remains aligned with the smooth surface while the pillar features are not resolved properly. The pillar tops are resolved as being pointed instead of the flat tops. The reason behind this result remains inexplicable, as the water immersion lens in this case should behave analogous to a normal objective used in air and give uniform profiles as were obtained in Figure 3-4. As soon as we entered the Cassie regime the pillar profiles became uniform and cylinder-like. The height of the pillars in both regimes is the same, calculated from base to the highest point. The base of the pillars in Cassie regime is again elevated.

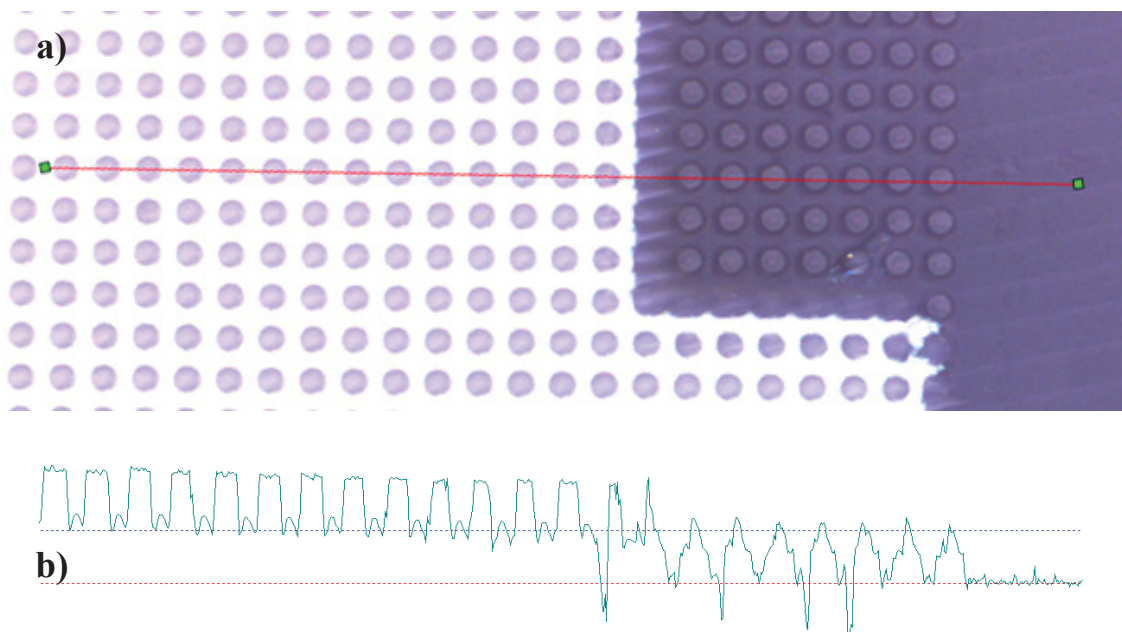


*Figure 3-8: a) CSM image of the PDMS SHS surface immersed under water. A portion of the SHS on the right is in Wenzel regime, as signified by the color change. On the right of the pillars is the smooth PDMS surface acting as a reference. b) height profile taken along the red line depicted in a).*

Another possibility of the elevation of pillar bases can be that water immersion objective is only scanning the pillar height that is wetted by the water and not able to scan underneath (pillar cavities trapping air). The light rays from air cavities trapped underneath are not being detected due to very low intensity after passing through water and reflected by PDMS. This possible reason can be neglected due to the fact that in Figure 3-8 the fully submerged pillars are of the same height as the pillars in Cassie state.

### 3.3.2 Future Work

The inconsistent results from white light confocal microscopy make it presently unsuitable for use in determining the water penetration on SHS. The reason for anomalies in imaging by CSM should be looked into by using better alternative imaging techniques like Laser CSM. Water and PDMS will be dyed fluorescently to better help in imaging the water interface level on SHS.

## 3.4 Characterizing Surfaces through Surface Topography Descriptors

The Cassie Baxter equation<sup>6</sup> has been used to predict advancing angles, but it cannot predict receding contact angles. Hence the Cassie equation is not useful for gauging the superhydrophobic nature of a surface. The aim of this section is to look for the factors which can help describe surface topography on a quantitative basis, and can help in predicting the mobility and adhesion of the liquid drop. This can help directly correlate wetting characteristics to surface

topography, and in effect allow fabrication of surfaces with tuneable superhydrophobicity, which are robust, durable, and wear resistant. The various surface descriptors can be directly computed by use of non-invasive surface scanning techniques like interferometry, and confocal microscopy.

The topographic descriptors in this report have been calculated by the use of white light confocal scanning microscope (CSM) with 100x magnification objective. The samples were plasma etched Teflon surfaces having random needle shaped geometry. The samples were worn down in intervals of three minutes for a total time period of 60 minutes, and the evolution of wetting characteristics and surface descriptors were tabulated at each interval. A more detailed description is provided in experimental section 3.2. Figure 3-9 shows the PTFE surface as it wears down under abrasion.

In this section, the focus is on describing the surface descriptors and how they are useful in helping to uniquely characterize a surface's topography. The surface parameters, individually or in combination, should be able to describe both the horizontal and vertical surface profiles. The complete parameters should be able to characterize the roughness features based on their size, shape, slope and spacing. They are enumerated in the sections below.

### **3.4.1 Introduction**

The applications that stem from the self-cleaning nature of SHS include preventing frost from adhering to the surfaces,<sup>12,13</sup> stain-resistant garments,<sup>14</sup> and reducing frictional drag in water.<sup>15,16</sup> Durability of SHS was highlighted in one of the earlier works in the late 80's, where the author acknowledge erosion of a superhydrophobicity imparting coating as a serious problem.<sup>17</sup>

While adhesive fluoropolymer coatings have enjoyed commercial success as non-stick cookware,<sup>18,19</sup> SHS presently are untapped; despite various reported wide-ranging applications they have not made commercial inroads for widespread use in everyday life. Among other factors hindering the wide usage of SHS (large scale reproduction barriers, cost etc.), prominent amongst them is their durability. Durability is limited by the inherently delicate nature of topography present on SHS, and mild mechanical wear on these surfaces results in loss of superhydrophobicity, rendering wide application range of SHS unutilized.

### **3.4.2 Way Forward**

The majority of studies done until now have not been systematic in correlating wetting characteristics (CA and CAH) and surface topography as a SHS wears down.<sup>20-24</sup> The abrasion procedure used in the majority of the studies is prone to leaving contamination on the SHS and many had a directional wear pattern, affecting and biasing the final CA. Sand abrasion methods used in some studies<sup>20,21,24</sup> are especially susceptible to this contamination. A majority of the studies imparted superhydrophobicity to the bulk material by use of a fluorinated polymer. Abrasion can remove this coating, exposing the bulk material underneath, and introducing a site of heterogeneity (in terms of differing chemistry and roughness from neighbouring material) which affects the wetting properties. Hence, the combined effects of change in roughness and surface chemistry produce a change in the wetting characteristics. These two components need to be studied separately to gain an in-depth knowledge of the individual effect of each on wetting. Also, a contamination free abrasion method conforming to accepted standards in other research fields needs to be transferred over to be used on SHS.

Lack of good experimental data on abrasion of SHS has been the biggest impediment to a more thorough understanding of durability. To our knowledge, this is a first study which reports a systematic investigation of how wetting characteristics of a superhydrophobic surface, changes as it wears. Wetting characteristics were investigated in relation to surface descriptors. Surface roughness and surface chemistry changes during wear have been alienated, and a contamination free random (non-directional) pattern wear method is used to abrade a surface. To study only the effect of change in surface roughness on wetting characteristics, a bulk hydrophobic material is used to keep surface chemistry consistent after abrasion, as depicted in Figure 3-9. The focus of the present research is to find surface parameters that can predict adhesion and mobility of a drop on a surface, which in turn will help in designing durable superhydrophobic surfaces.



*Figure 3-9: Hydrophobic bulk in a SHS eliminates studying changes in surface chemistry, and allows focussing only on surface topography as it is a prime factor in imparting superhydrophobicity.*

### 3.4.3 Experimental Methods

Experimental details of the superhydrophobic PTFE surfaces used in this study have been described in detail elsewhere.<sup>10</sup> The experimental conditions used in plasma etching are such that the PTFE surface is chemically modified to a minor degree and only a small amount of oxygen is incorporated on surface.<sup>10</sup> PTFE SHS used in the study have coniferous random geometry as shown in Figure 3-10.



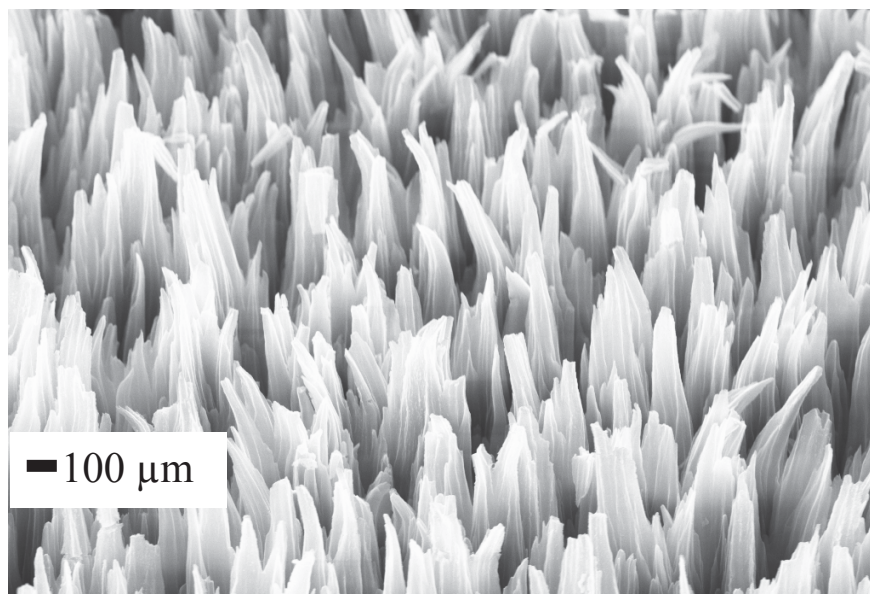


*Figure 3-10: SEM of unworn plasma etched Teflon.*

Surface topography and surface descriptors of the samples were resolved with Carl Zeiss Axio-700 confocal scanning microscope (CSM). CSM helps in quantitative evaluation of the surface topography. A 100x objective with an image field of  $117\ \mu\text{m} \times 94\ \mu\text{m}$  and  $0.16\ \mu\text{m}$  lateral resolution was used for imaging all the samples with a white light source ( $400\ \text{nm} - 700\ \text{nm}$ ). Contact angles were measured with in-house equipment and processed with ADSA25. Wetting characteristics of the sample were measured and quantified by advancing CA and receding CA measurements. Advancing CA provide information about the repellency of a surface, while insight about the mobility of the liquid on the surface is given by the difference between the advancing and receding CA. Smaller differences imply more mobility of the liquid on the surface and vice versa. Contact angles were always measured with de-ionised water using the sessile drop method. A hole was drilled on the sample, and a water filled syringe was mounted below the surface through the hole. The syringe was then driven to create a drop on the surface. Water was pumped into the drop at the rate of  $0.5\ \mu\text{L/s}$ , and advancing CA were measured at one second intervals as the drop volume increased from  $20\ \mu\text{L}$  to  $60\ \mu\text{L}$ . Reported advancing CA are an average of all the measured advancing CA. Water was then withdrawn at a rate of  $0.5\ \mu\text{L/s}$  from this  $60\ \mu\text{L}$  water drop until it reached a volume of  $20\ \mu\text{L}$ . The receding CA were measured at an one second intervals. Reported receding CAs are an average of all the measured receding CAs. Surface imaging was done using a Carl Zeiss LEO 1430 scanning electron microscope (SEM). Before taking SEM images, a gold layer of  $\sim 10\ \text{nm}$  is deposited on the sample surface. SEM helps to elucidate the physical state of the surface after each wear interval.

Mechanical wear on surfaces was done by abrading with  $\frac{1}{2}\ \text{mm}$  diameter inert glass beads (Manus Abrasive Systems, Edmonton, Canada) on an in-house modified gyrotory shaker (Model G2, New Brunswick Scientific Co. Inc., New Jersey, USA). The abrasion experiment was designed based on standard test specification ASTM F735-06 (Standard Test Method for Abrasion Resistance of Transparent Plastics and Coatings using the Oscillating Sand Method).<sup>11</sup> SHS were placed at the bottom and abrasive material covered the surface, as depicted in Figure 3-11.

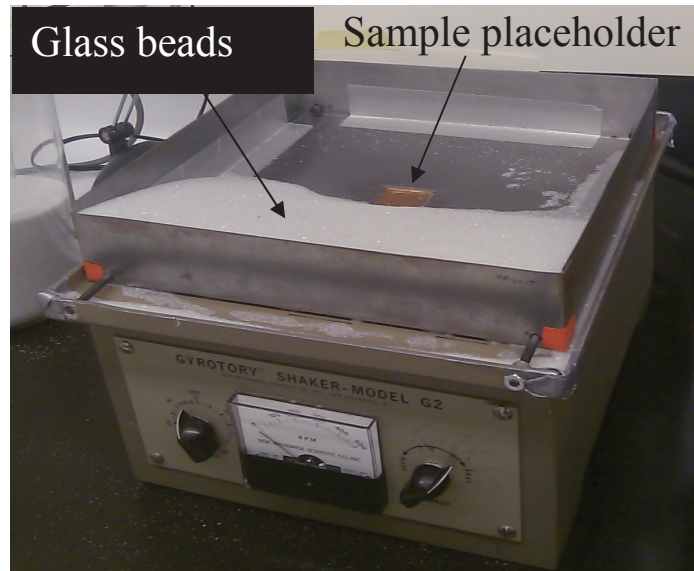


*Figure 3-11: Photograph of abrasion setup.*

This set-up allows control on wear (i.e., revolutions per minute), the abrasive material, and its amount, and generates a random wear pattern on surface. A customized sheet metal tray (10" × 10" × 2", 3200 mL capacity) with walls on each side to confine the abrasive material was built on the gyratory shaker. The bottom plate of the tray had a recessed area (1 3/4" × 1 3/4") to affix the sample flush with bottom of the tray, Figure 3-11. This prevented sample edges from interfering in the motion of the abrading material. Samples were placed flat at the bottom of the gyratory shaker and covered fully with 2L of glass beads, used as the abrading material. The circular motion of the gyratory shaker abraded the samples in random fashion. This method of abrasion is repeatable, and wear can be controlled on a surface by the rotational speed of shaker. Glass beads are inert, and don't leave residue on surfaces and hence produce little to no contamination of the samples. The bead size is sufficiently large so as not to be lodged into any of the asperities in the PTFE SHS.

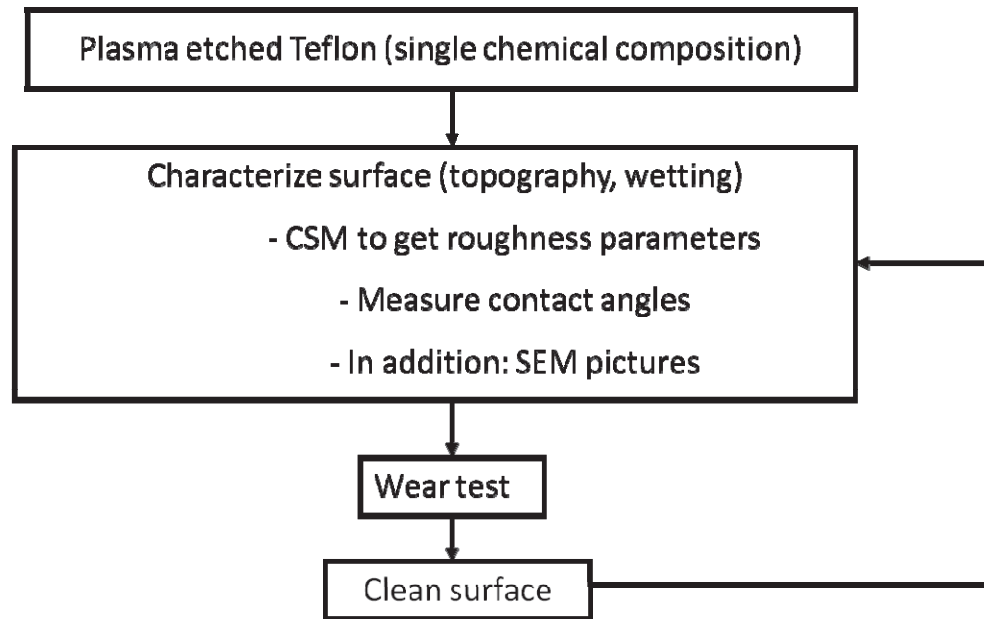


*Figure 3-12: Flowchart of experimental procedure. SHS is abraded and cleaned of contaminants. Topography and wetting are characterized by CSM and CAs respectively.*

Figure 3-12 details the experimental procedure. Plasma etched Teflon SHS were worn down in varying intervals of three minutes at 250 rpm on a gyrotory shaker. Speeds lower than 250 rpm wear down SHS slowly, while greater speeds are aggressive. After each wear interval, an abraded SHS was cleaned by ultrasonication for 15 minutes in 100% ethanol to get rid of any contaminants on the sample surface.

Figure 3-13 shows the sample divisions and the relevant respective characterizations done. After a period of wear, the wetting characterization (Advancing CA + Receding CA) was measured and the confocal scanning was done near the hole where wetting data was collected to keep the data comparison consistent, see the upper part of the sample in Figure 3-13. CSM was taken at three different areas around the hole, to better help in understanding the variation and homogeneity in the worn surface topography. The lower part of the sample, Figure 3-13, was used for SEM imaging to help visualize the topography. A small portion was systematically cut-out from the sample (number 1, 2, 3 etc. in Figure 3-13) for this purpose as depositing of the conductive gold layer for SEM imaging may have contaminated the surface during further wear stages and may have chemically modified the sample surface if removal were attempted. As the samples were cut out for SEM evaluation, a protruded edge began to develop on the sample and hence different regional wear patterns can arise due to obstruction of free flow of abrading material.

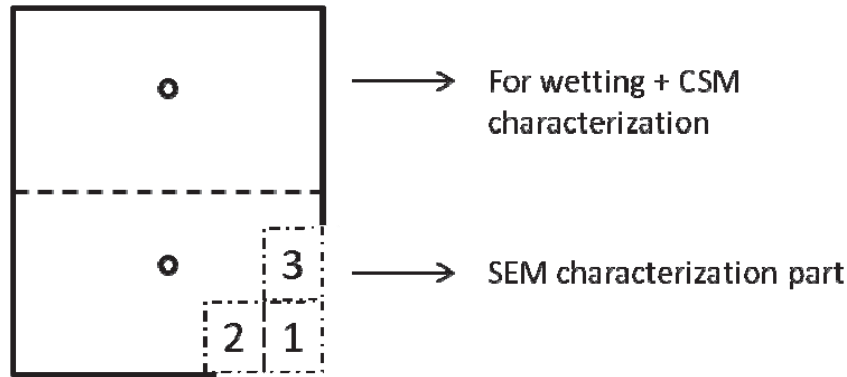


*Figure 3-13: Schematic showing regions of sample and respective characterization done. The holes signify the place where syringe is inserted from the bottom for ADSA CA measurements. Numbered portions 1, 2, and 3 in the lower right corner signify the sample portions which were systematically cut out after each wear cycle.*

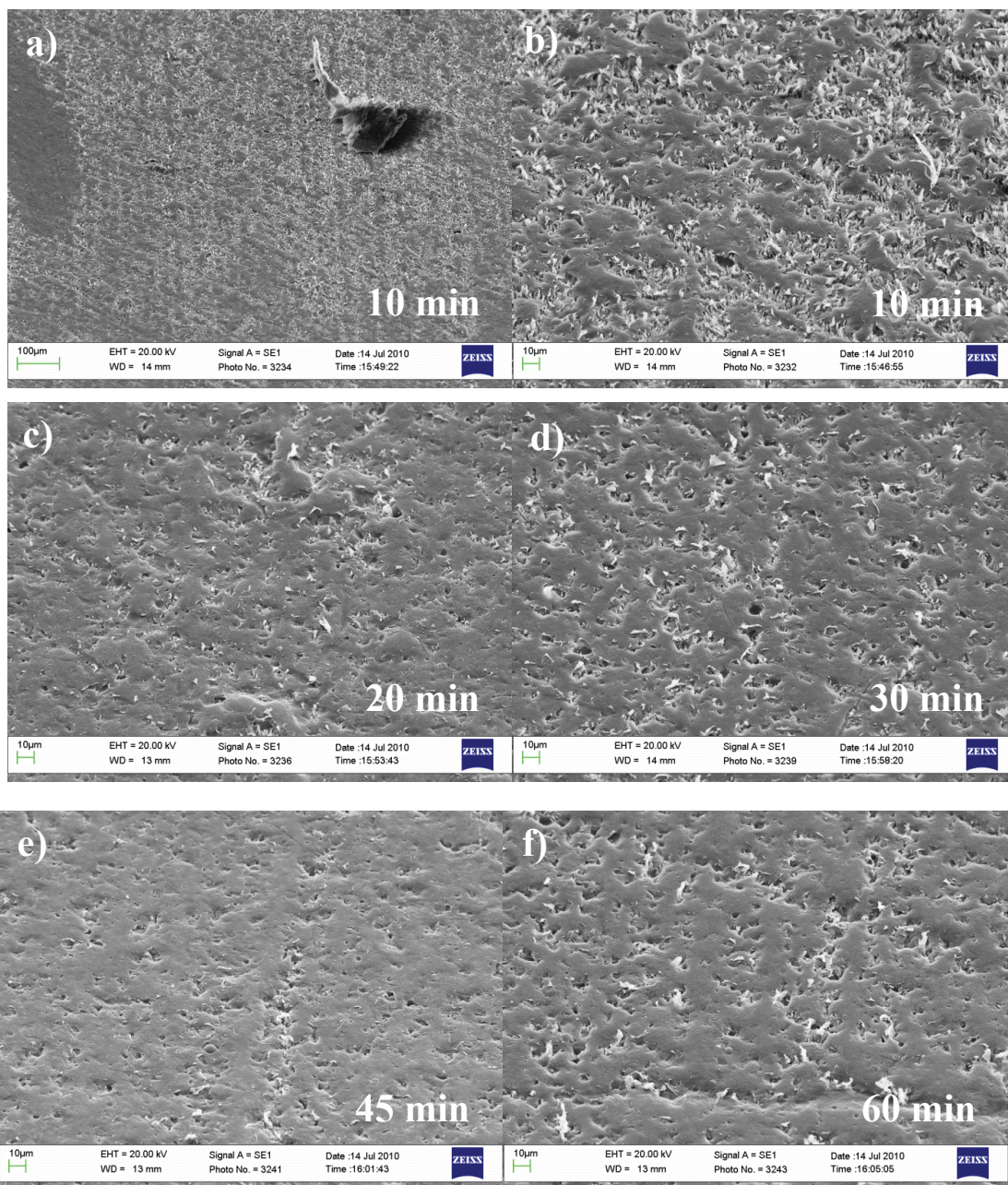
Care is taken such that CSM, SEM and CA were all measured on the same position on the sample; this ensures that the parameters (surface descriptors, wetting characteristics) collected through each measurement (CSM, SEM, and CAs) are correlated and representative of each other.

### **3.4.4 Results and Discussion**

#### **3.4.4.1 Quantitative Examination of Surface Wear and Wetting Characteristics**

Wear is a stochastic phenomenon, and this should be kept in mind as the information is generated, analyzed, and understood. As such, trends may be more valid at times than the absolute values.





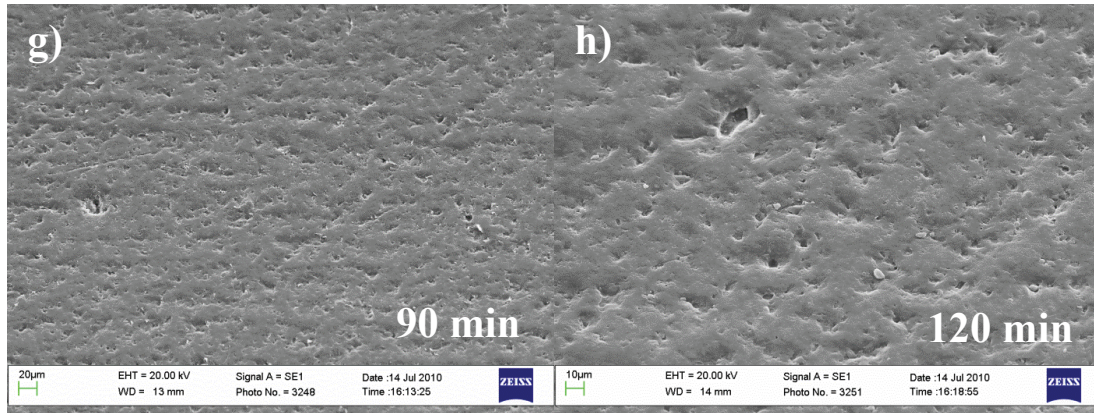
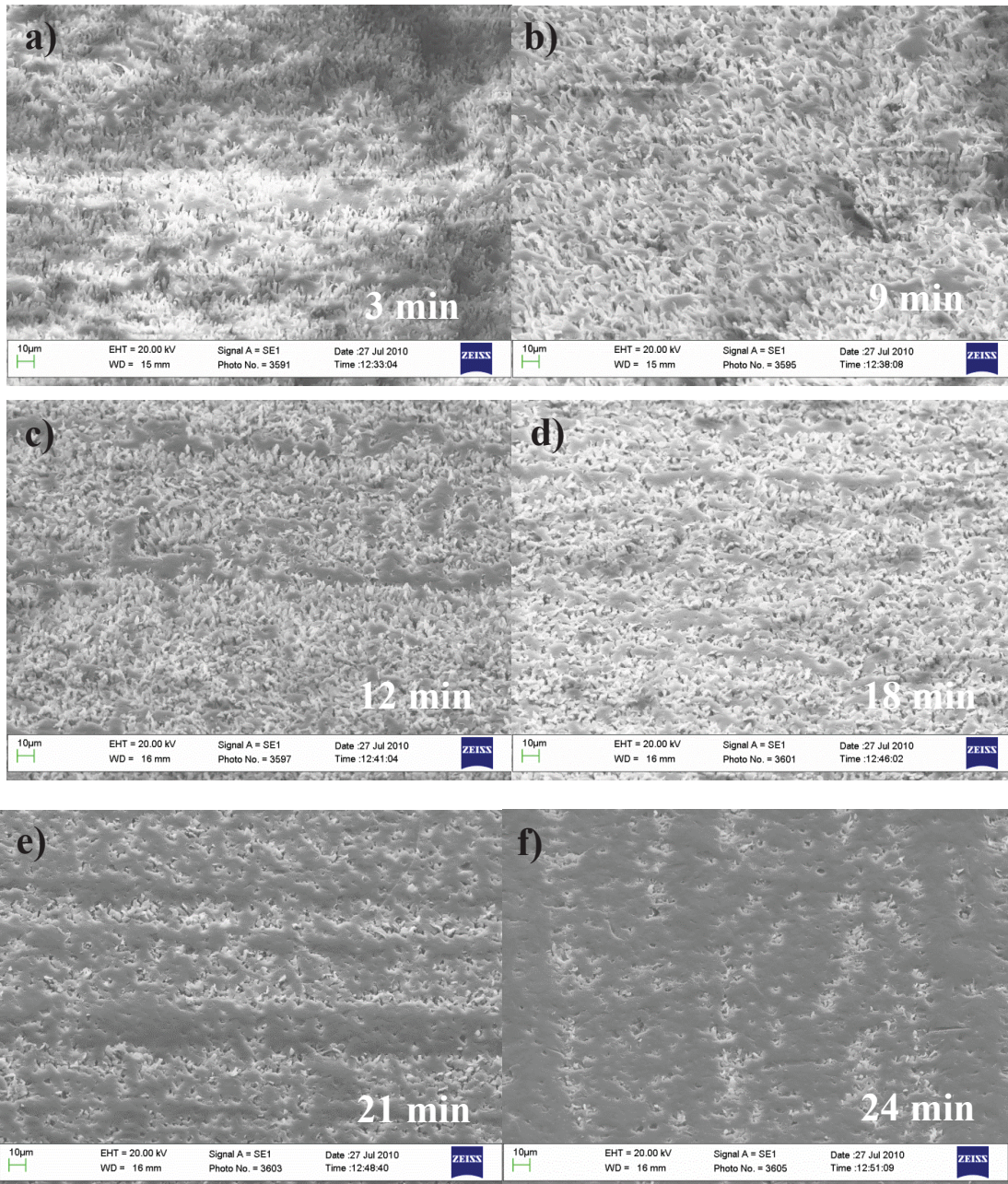


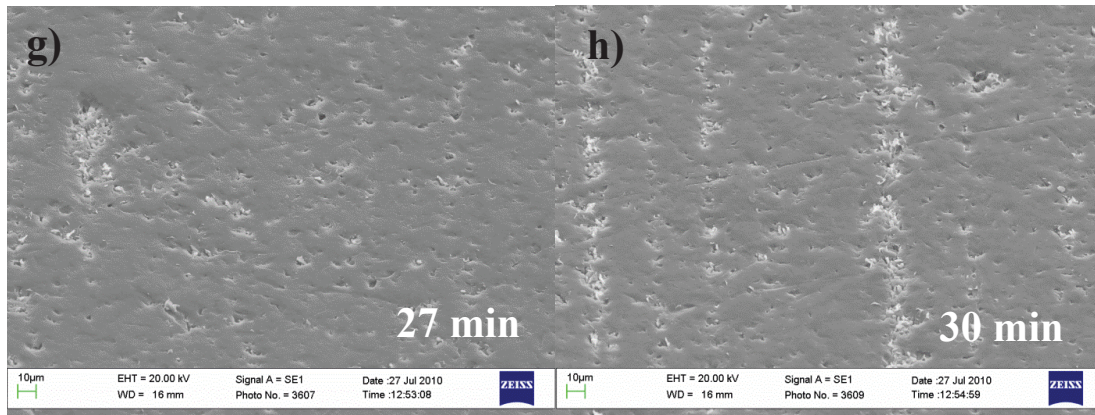
*Figure 3-14: SEM of sample 17 being worn at 250 rpm for different durations of time. Inset shows the cumulative time a surface has been worn. In Figure (a) the protrusion is an artifact stuck on the surface. Figure (a) also shows the regional dependency of wear, due to it being a stochastic phenomenon.*

SEM images in Figure 3-14 show the decrease in surface features (valleys and peaks) as a PTFE surface wears. Figure 3-14 (a) shows the regions with different wear rate, this effect can be dependent on proximity of the worn area to the edges of the sample, where the edges can disrupt the movement of the abrasive, leaving dead regions. The dead region refers to the region having considerably lower rotational speed of abrading material than neighbouring regions. This can occur due to buckling up of the sample edge during abrasion, due to becoming unstuck from the material holding it to the gyratory shaker surface or simply due to inherent waviness of the PTFE sheet. The protruding surface can obstruct free flow of abrading material. Also, since the abrading material rotates in an undefined way on the gyratory shaker, the wear pattern on a surface will be random, and hence regional wear patterns are expected.

Regions in which peaks are dominant decrease progressively with increase in wear time. At 10 minutes (Figure 3-14 b), the peaks and the valleys on the sample surface occupy roughly equal area and by 20 minutes (Figure 3-14 c) the surface is already dominated by plateaus. At 45 minutes (Figure 3-14 e), longer surface wavelength components have started to become dominant, and at 120 minutes (Figure 3-14 h), they dominate completely. It is pertinent to mention here that Figures 3-14 (d) and 3-14 (f) show a similarity in surface wear condition although wear times are different, due to the random regional wear pattern on the surfaces.







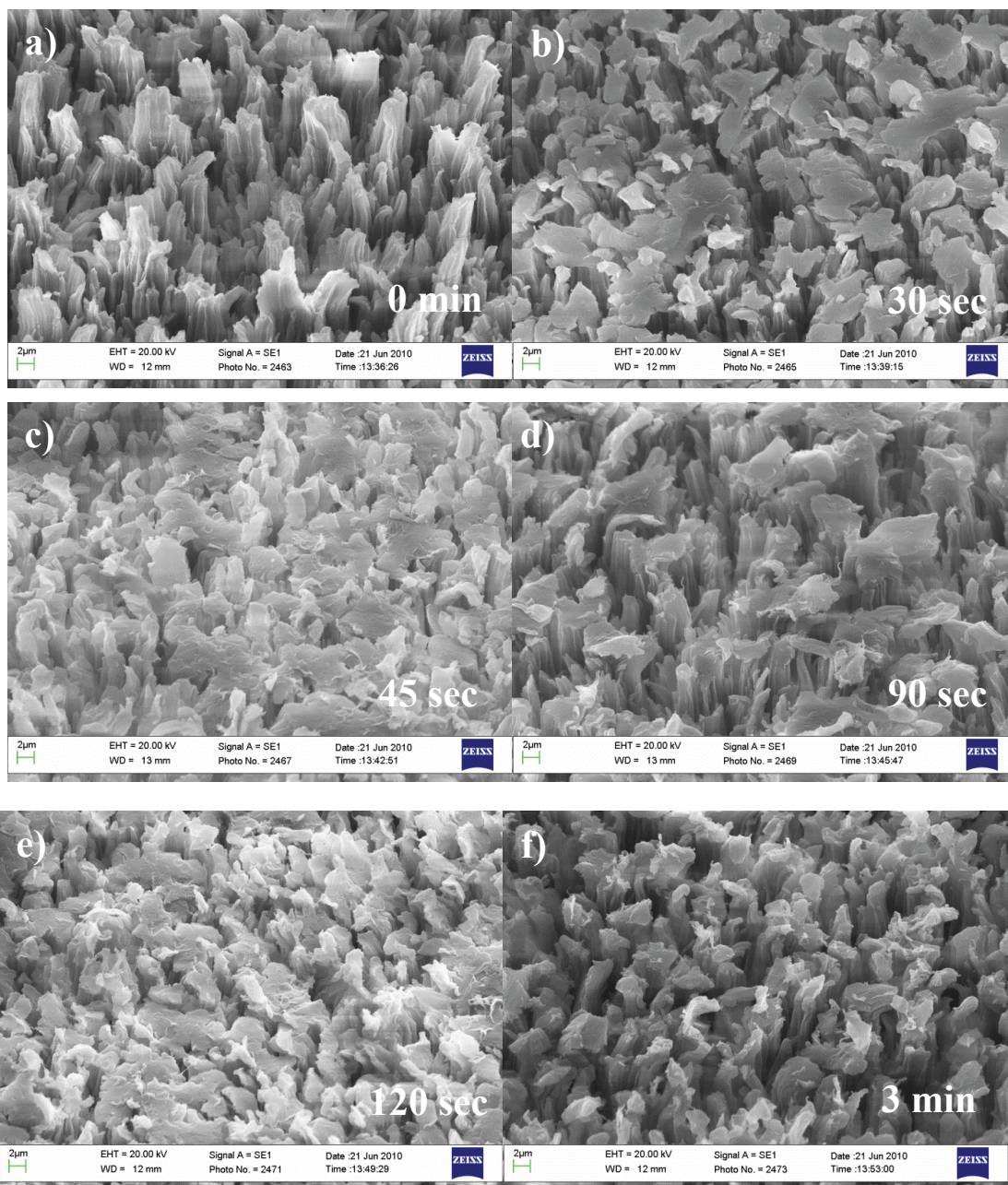
*Figure 3-15: SEM of sample 25 as it is worn down at 250 rpm.  
Inset shows the time the sample has been worn down for.*

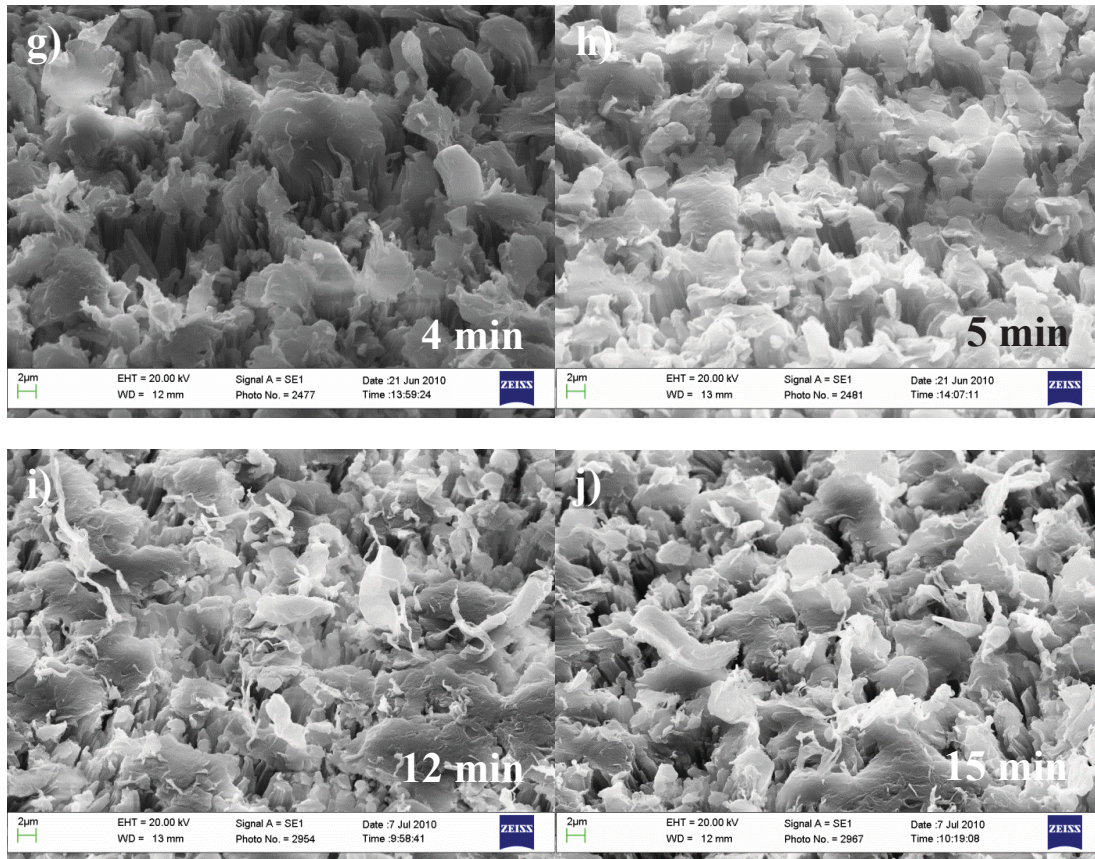
Figure 3-15 shows images of sample 25 at different wear intervals after being worn at 250 rpm. Figure 3-15 (a) shows the small number of randomly distributed patches of flattened PTFE peaks, and as the wear time increases the surface is progressively flattened, as shown in Figure 3-15 (e), (f), (g), and (h). The corrugations in Figure 3-15(h) might be due to the corrugations of the original PTFE sheet which was plasma etched.

SEM images Figures 3-14 (b) and 3-15 (b) show a similarity in the wear pattern, and Figure 3-15 (b) will evolve similar to Figure 3-14 (b) as the surface wears more. This is validated by Figure 3-14 (c) and Figure 3-15 (e). Also, from Figures 3-14 (c) and 3-15 (d), it can be seen that wear pattern is not same even though the wear time difference is small, but Figure 3-15 (e) has a more consistent wear pattern to Figure 3-14 (c). This shows the obvious time dependence of surface wear.

SEM images in Figures 3-14 and 3-15 show that the PTFE surfaces are randomly abraded by the gyratory shaker in a consistent way, if the abrasion conditions are kept the same. The wear pattern is random, homogeneous, and consistent among different samples of same surface.



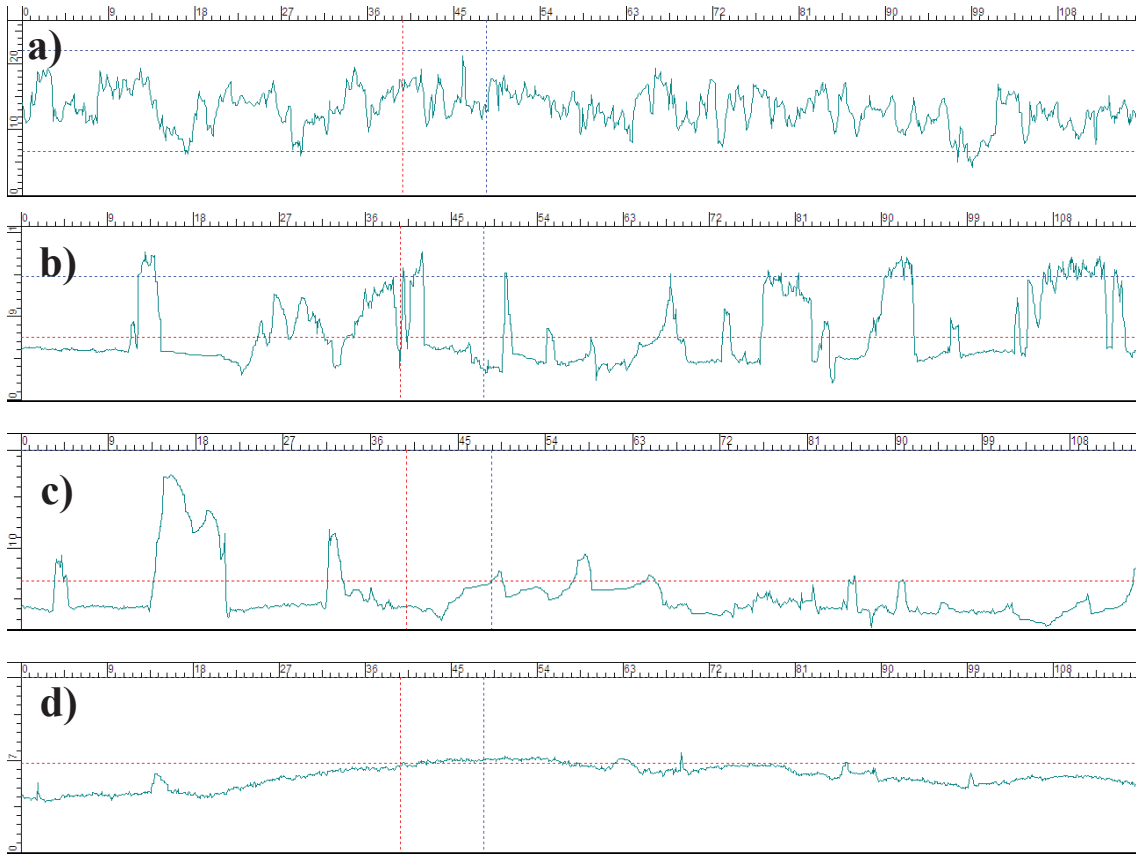




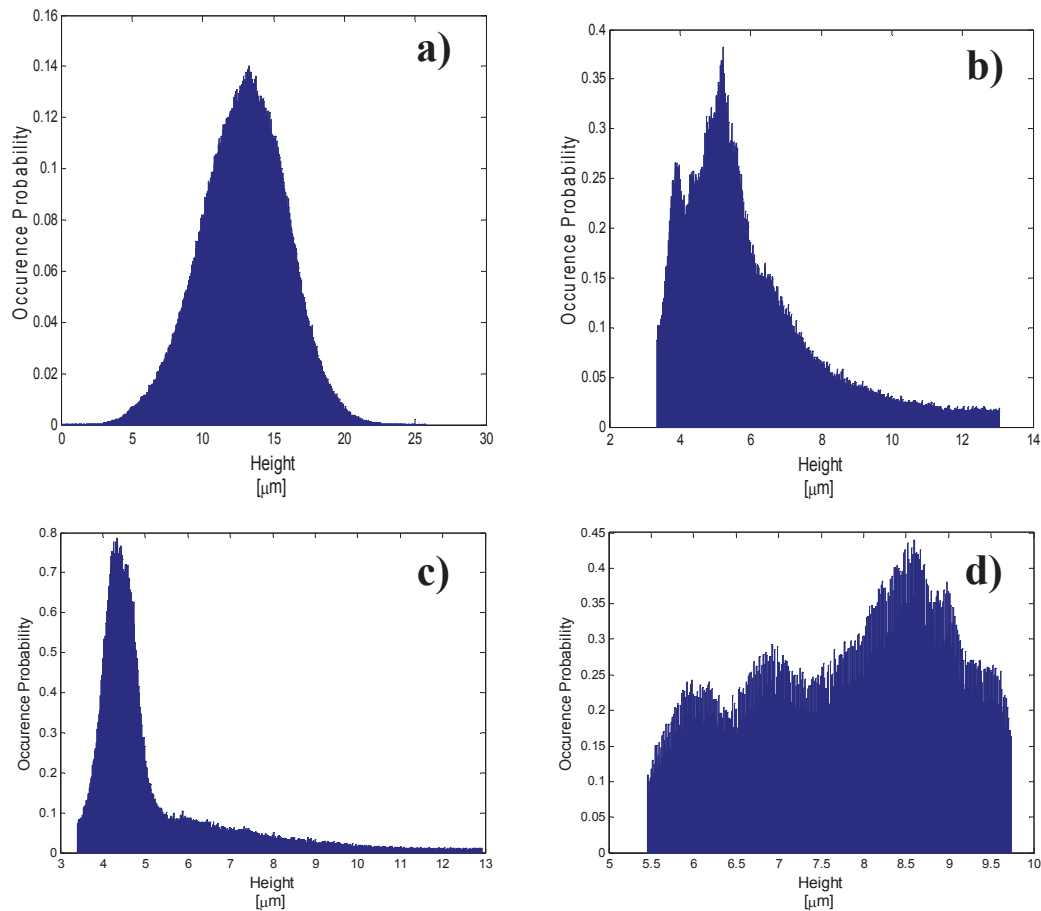
*Figure 3-16: SEM of sample 18 being worn at 250 rpm for different durations of time. Inset shows the cumulative time a surface has been worn.*

Figure 3-16 shows the wear evolution of PTFE surfaces at the inception of the wear, how the surface PTFE peaks are affected in initial wearing time. The peaks are immediately affected, and hence as wear time increases the eroded surface being non-elastic starts flattening, as can be also seen in Figures 3-14 and 3-15. Anomalies in comparison can occur due to differing local wear pattern, as we can see aggressive wear in Figure 3-16 (c) and (e), compared to Figure 3-16 (d), and (f), respectively. Qualitative physical comparison can be done on the samples by using white light confocal scanning microscope (CSM) as shown in Figure 3-17.





*Figure 3-17: Surface profiles for (a) unworn, (b) 3, (c) 12, and (d) 27-minute worn samples evaluated from CSM data. The profiles are for sample 25.*



*Figure 3-18: Normalized histograms for (a) unworn, (b) 3, (c) 12, and (d) 27 minute worn samples evaluated from CSM data. The corresponding height profiles are displayed in Figure 3-16. It can be seen that height distribution starts as Gaussian, becomes positively skewed Poisson distribution, and then becomes a lognormal distribution with high peaks and low valleys removed. The histogram distributions are for sample 25. The information has undergone noise filtering to remove artificial peaks and valleys.*

Figure 3-17 (a) shows that the surface is composed of closely spaced peak features distributed homogeneously. A SEM image of the unworn surface in Figure 3-10 shows the tightly packed peaks. The height distribution is given in Figure 3-18a. The average peak height on the surface is  $12.87 \pm 2.99 \mu\text{m}$ .

As the surface wears down the peaks start getting flattened, as can be seen in height profile in Figure 3-17b and also shown in SEM images Figure 3-15a. The average peak height on the surface is  $6.07 \pm 2.39 \mu\text{m}$ , a 50% decrease from original surface distribution. This shows that all the peaks are affected as wear starts, and the highest peaks have their tops shaved and hence skew the height distribution, Figure 3-15b. SEM image in Figure 3-15a shows small patches of flattened peaks. From CSM height profiles, like the one given in Figure 3-17b, the average length of the flat area was found to be  $\sim 10.6 \mu\text{m}$ . This was calculated by assuming that the heights lying

in the lower 5% probability of the height distribution ( $<3.72\text{ }\mu\text{m}$ ) are flat plains, and 35 samples were taken on 3 different areas (by virtue of CSM measurements) with at least 10 samples on each measurement area. The minimum recorded length of a flattened patch was  $3.9\text{ }\mu\text{m}$ , and maximum  $21.7\text{ }\mu\text{m}$ . In Figure 3-17a, and again illustrated in Figure 3-19, it can be seen that large numbers of flat patches are close to the average length of  $\sim 10\text{ }\mu\text{m}$ , with some flat patches stretching to  $\sim 22\text{ }\mu\text{m}$ . Also as shown in Figure 3-18b, the histogram height distribution shows a positive skew due to peaks being shaved off after abrasion as described previously and shown in Figure 3-15a and Figure 3-17b.

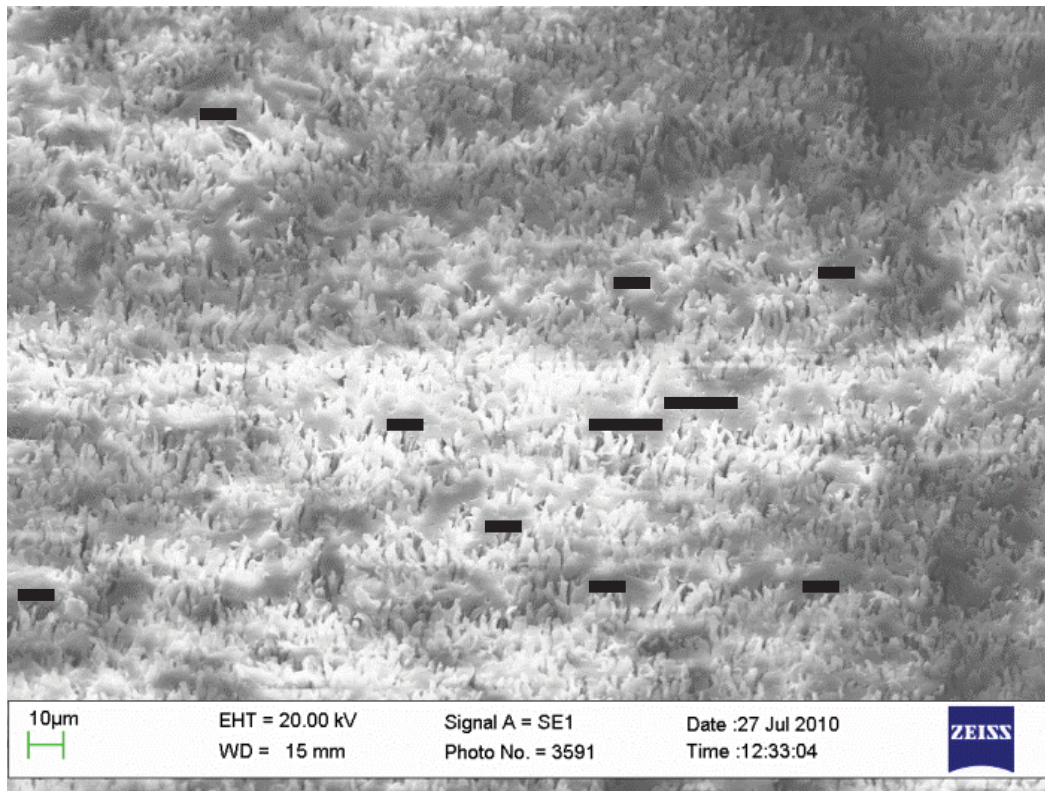


*Figure 3-19: Illustrating the length of flattened patches on sample 25 SEM, worn for 3 minutes. The small black bars have length of  $10\text{ }\mu\text{m}$ , and bigger bars are of length  $20\text{ }\mu\text{m}$ . It can be seen that surface has large number of flattened patches with  $10\text{ }\mu\text{m}$  length, and some of them extend to  $20\text{ }\mu\text{m}$ . The black bars act as a visual guide to flat patches on the surface.*

The histogram height range in Figure 3-18c is the same as the 3 minute histogram in Figure 3-18b. But the noticeable difference arises in height profile in Figure 3-17c due to the noticeable erosion of the highest peaks and average height peaks. This difference can be seen in the height profile, Figure 3-17c, where the flattened areas have increased, with peaks becoming scarce. Height profiles in Figure 3-17c closely resemble the topography in SEM Figure 3-15c, as we see a large number of flattened peak tracks averaging  $\sim 25\text{ }\mu\text{m}$  in length (calculations done based on methodology discussed previously). In Figure 3-18d the histogram range is  $\sim 5.46\text{ }\mu\text{m}$  to  $\sim 9.72\text{ }\mu\text{m}$ . All the peaks have nearly equal probability of occurring, suggesting a flat surface with rough undulations (longer wavelength peaks). This decrease coupled with the accompanying height profile in Figure 3-17d shows that there are no remaining high peaks from the previous

surface. The curvature in the height profile shows the dominating long wavelength component, and is also the reason for the probability increase from  $\sim 8 \mu\text{m}$  to  $\sim 9 \mu\text{m}$  in the histogram, Figure 3-18d. Importantly, it has to be noted that minimum height has increased from the previous wear duration histograms, suggesting that the valleys have been filled by the abraded peak material. Figure 3-15g shows this scenario, with the entire surface flattened.

The close resemblance of physical surface observation through SEM, and quantitative surface data through CSM validates the CSM data in its ability to faithfully report surface topography.

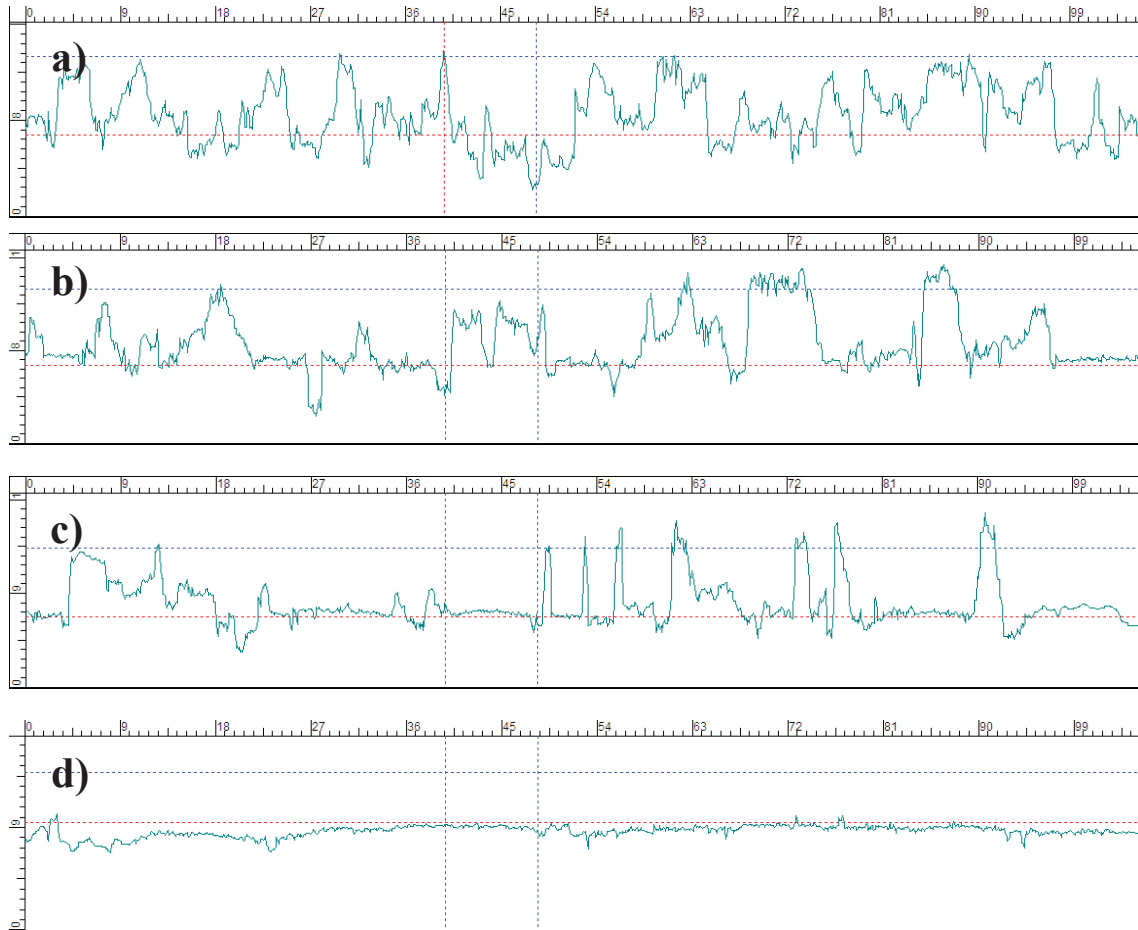


*Figure 3-20: Surface profiles for (a) unworn, (b) 3 minutes, (c) 12 minutes, and (d) 27-minutes worn samples. The profiles are for sample 27-1.*

Figures 3-20 and 3-21 repeat the same observations from CSM data for another sample, 27-1, as done in previous section for sample 25. It can be seen that the trend in Figures 3-20 and 3-17 closely mimics each other. The height distribution histograms in Figures 3-18 and 3-21 show the same evolution, except the difference in the starting height distributions. The variation in unworn sample height distribution is expected, as the wear is a stochastic phenomenon. But as the surface wears down, the peaks become scarce and then completely flatten out in same manner in both the samples. The difference in Figures 3-20d and 3-17d arises due to absence of major curvature on the surface, and hence the respective histograms differ too as shown in Figures 3-18d and 3-21d. The rough undulations are still present on the 27 minute worn surface, and it is not completely flat.

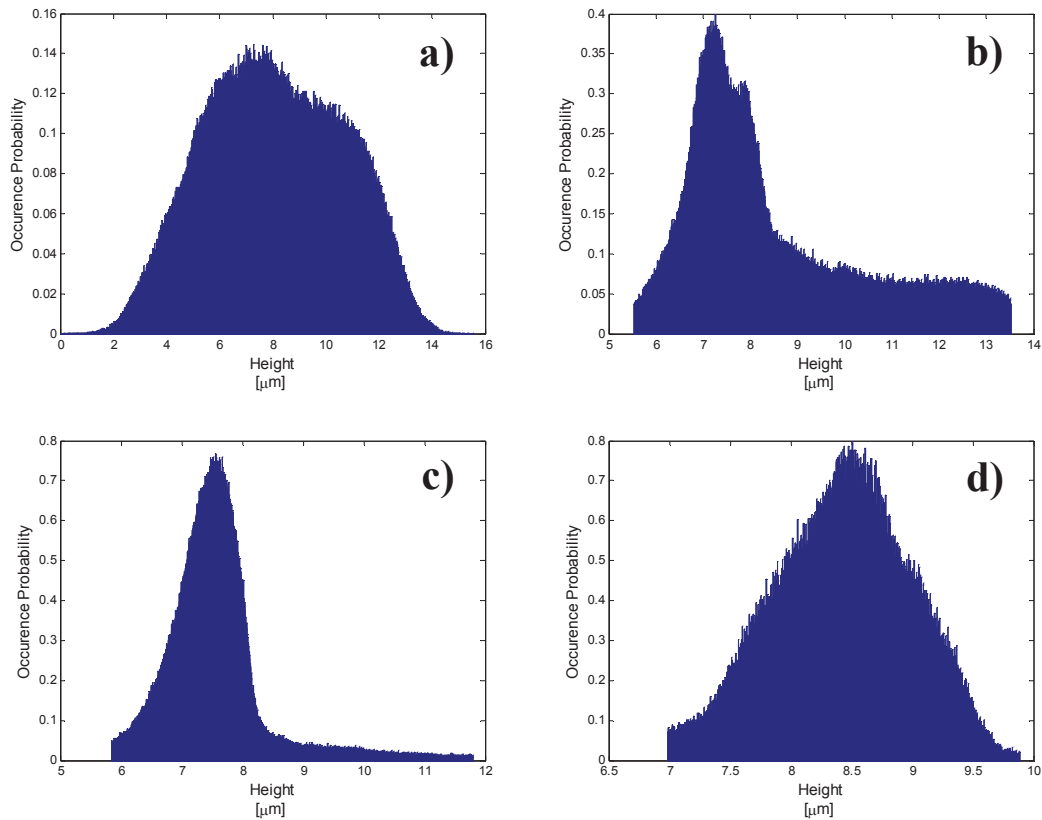


*Figure 3-21: Normalized histograms for (a) unworn, (b) 3 min, (c) 12 minutes, and (d) 27-minutes worn samples evaluated from CSM data. The corresponding height profiles are displayed in Figure 3-17. It can be seen that height distribution starts as Gaussian, becomes positively skewed, and then returns to Gaussian but with high peaks and low valleys removed. The profiles are for sample 27-1. The information has undergone noise filtering to remove artificial peaks and valleys.*

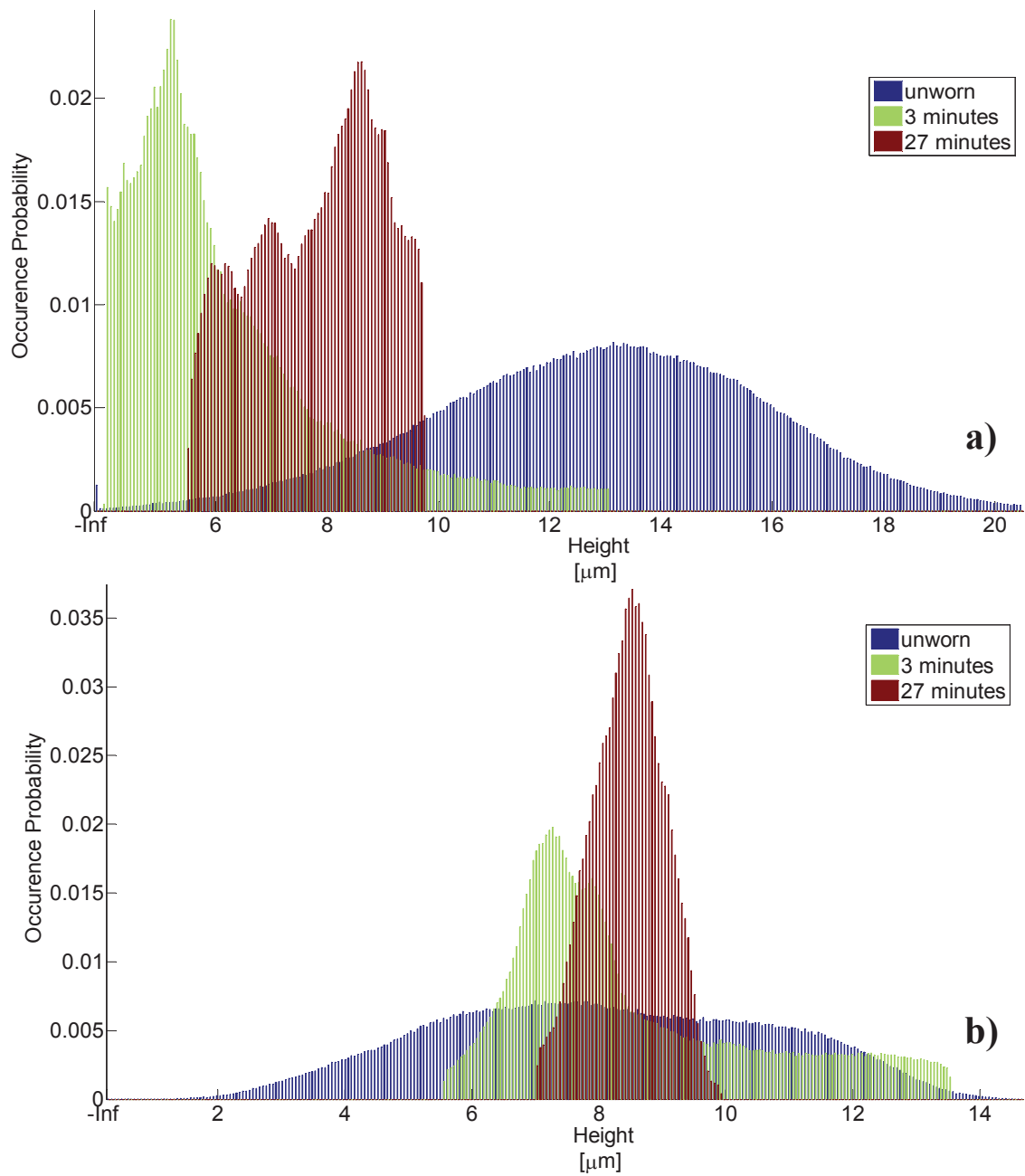


Figure 3-22: Comparing height distribution in (a) Sample 25, and (b) Sample 27-1 at unworn, 3 minutes, and 27 minute of wear duration. Normalized histograms have been evaluated from CSM data. The information has undergone noise filtering to remove artificial peaks and valleys.

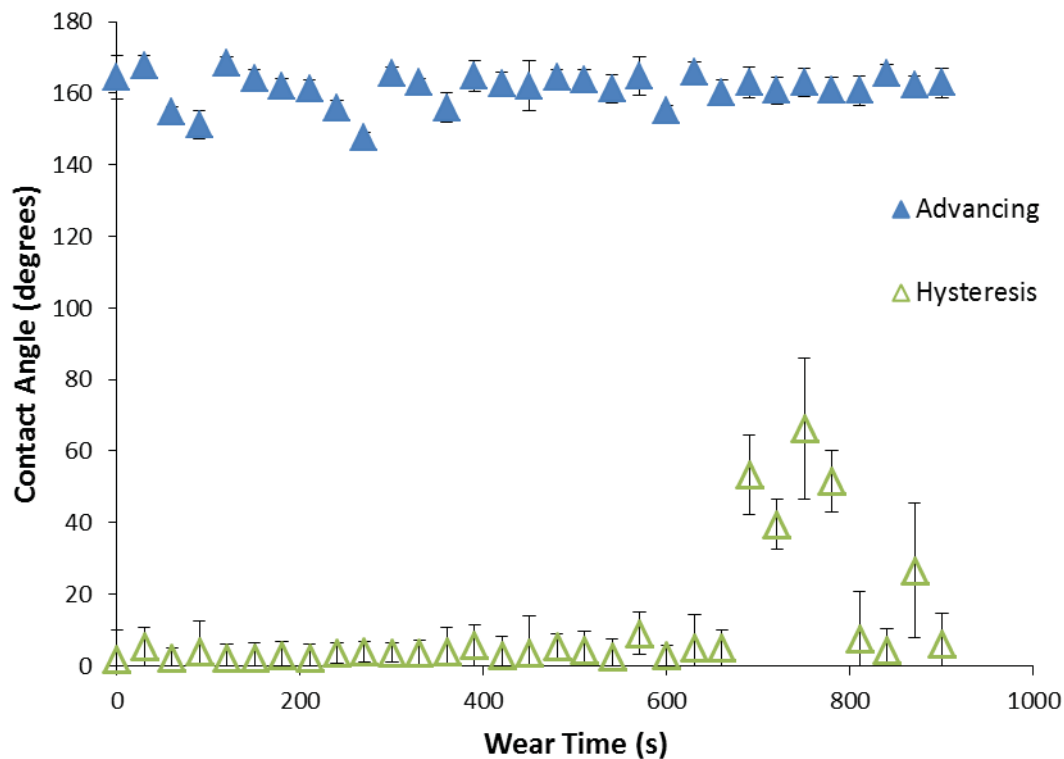


Figure 3-22 shows the normalized height distribution histograms for unworn, 3 minute, and 27 minute sample plotted on one graph, for two samples. It can be seen that initially, the surface heights form a nearly Gaussian distribution. After 3 minutes of wear, both height histograms shift to the left and in the same fashion. After a wear time of 27 minutes, the surface is dominated by what were once the valleys on the unworn surface, for both the samples. Hence also illustrating the flatness of the surface. The initial distribution of the heights in the surface 27-1 makes the heights and valleys wear off in a nearly symmetrical fashion. Whereas in sample 25, the peaks were aggressively worn off in the initial minutes of wear.

From Figures 3-18 and 3-21, starting from a nearly Gaussian distribution with wide height distribution among valleys and peaks, the height distribution becomes positively skewed for both the samples as they wear. When the surface becomes nearly flat with higher wavelength undulations, the histogram returns to a normal distribution but with a very narrow height distribution. The above discussion shows that the surface topography changes consistently among samples. The minor differences in the histograms are due to different height distributions in the starting unworn sample, but the evolution of heights with abrasion shows the same trend for all samples.

CSM height data helps to quantitatively evaluate the change in roughness and surface features as a surface abrades. SEM helps validate the CSM data. The abrasion method chosen is also consistent among all the samples. Thus the CSM data can be used for further qualitative measurements of various surface roughness descriptors.

The main motivation of this study is to understand the repellency and mobility of the liquid on the surface as it wears. Advancing CA helps in understanding the adhesion on the SHS, and the difference between advancing and receding CA, known as CA hysteresis, and serves as an indicator of the mobility of a liquid on the SHS. Advancing and receding CA collectively are termed as the wetting characteristics of a surface. Hence, Figures 3-23, 3-24 and 3-25 tabulate the wetting characteristics on various surfaces as they wear.



*Figure 3-23: Wetting data on plasma etched PTFE surface, sample 18.  
This graph shows the wetting data in the initial stages of wearing.*

Figure 3-23 shows the wetting characteristics in the initial stages of wear for sample 18. The CA hysteresis jumped at 690 s (11.5 min) until 780 s (13 min), and then dropped back to  $\sim 10^\circ$ . SEM images in Figure 3-16 show the corresponding surface topography change. It can be seen that initially the peaks are spread out and as the surface is eroded, the peaks have their tops shaved off and also their “packing density” becomes compact. Figure 3-16a, c, f and h show this. CA hysteresis jumps at around 690 s. The SEM image at 720 s, Figure 3-16i, shows that peaks have been abraded off and their “packing density” is compact. Also, little shards of Teflon are protruding from the surface. The surface in Figure 3-16j at 15 minutes, is in the same condition as in Figure 3-16i, but the CA hysteresis at this point is  $< 10^\circ$ . The difference can arise due to regional topography differences on the surfaces due to stochastic wear on the surface. It is to be noted here that, the advancing angle during the whole wear duration is nearly constant at  $160^\circ$ , showing that repellency is not affected, unlike mobility, as the surface topography changes.

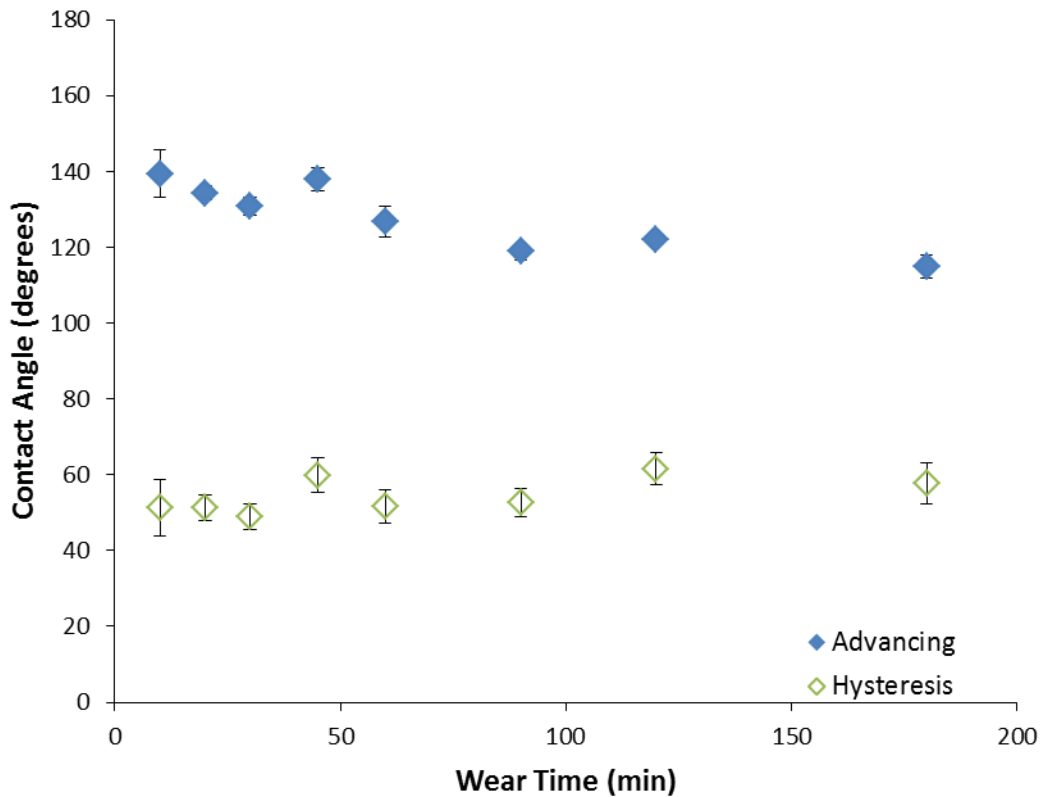


*Figure 3-24: Wetting data on plasma etched PTFE surface, sample 17.  
Graph tabulates the long term wear wetting data.*

Figure 3-24 depicts the wetting characteristics of a surface subjected to wear for a long time. The CA hysteresis for the sample has already risen to 51° at 10 minutes of abrasion, and stays nearly constant with an increase of only 6° after 3 hours of abrasion. The advancing contact angle decays with a gentle slope and reaches 115°, the intrinsic contact angle for the smooth surface of Teflon. Figure 3-14b shows that after 10 minutes of wear, the surface peaks are mostly flat.

From Figure 3-23, it can be deduced that the water drop remains mobile on the surface in the initial period of wearing. From Figures 3-16 and 3-23, the surface effectively repels water drops while the peaks are still dominant, and tentatively as the peaks start to flatten to a greater extent the mobility of the water drop is compromised, Figure 3-24. The exact delineation point where the mobility decreases cannot be gauged from this information, or a point even exists after which the mobility decreases universally for all the samples. The point when CA hysteresis jumps and the mobility for the drop decreases, and conversely adhesion increases, will not be constant for all surfaces. This is due to the fact that both the surface topography and abrasion on the surface is random. Figures 3-23 and 3-24 show this too, as the mobility jumps at different wear times, and that CA hysteresis jumps in between and then drops for sample 18, Figure 3-23.

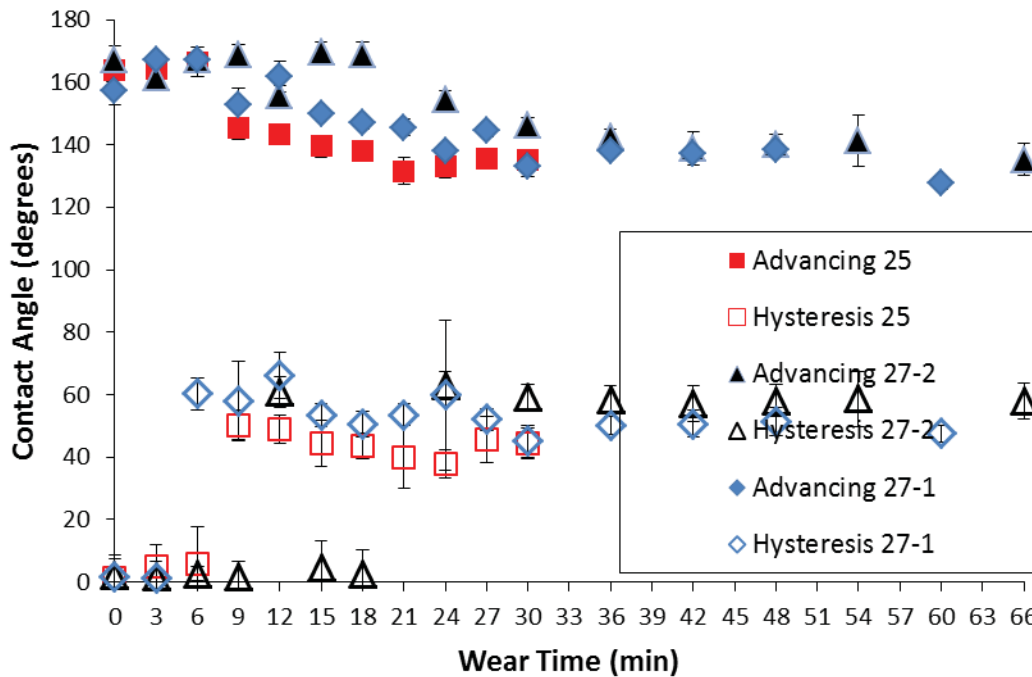
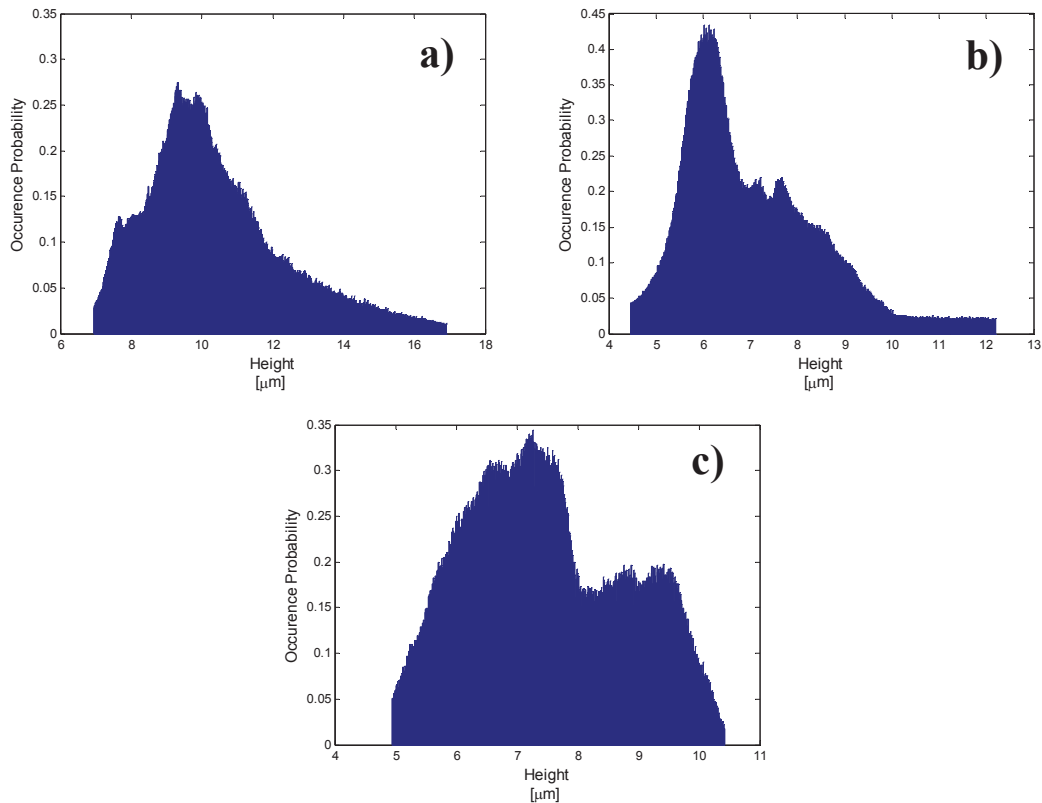


Figure 3-25: Wetting data on various plasma etched PTFE surfaces.

Figure 3-25 shows the water advancing CA and CAH on the surfaces with respect to wear time. It can be seen that CA hysteresis rises after 9, and 6 minutes of wear for samples 25 and 27-1, respectively. For sample 27-2, CA hysteresis rises momentarily at 12 minutes but then drops back to  $<10^\circ$  and finally rises after 24 minutes. This behaviour was observed in Figure 3-23 for sample 18, too. For sample 27-2, a wear time of 24 minutes will be taken as when the hysteresis jumps, as it is permanent. The advancing CA, and CA hysteresis follow the same trend for all the samples except the difference between CA at various wear times. SEM images in Figures 3-15e and f, sample 25, show that the surface starts becoming flat after 24 minutes of wear time, and the wetting data for all samples show similar behaviour between contact angles after this point. This can be due to consistent abrasion among the samples as discussed earlier. Additionally, Figure 3-14c, sample 17, also shows it becoming flat  $\sim 20$  minutes, and the mobility of the water drop has already decreased as shown in Figure 3-24. Figure 3-24 shows that the liquid drop at this point is in a high state of immobility. Mobility for the water drop on the surface is typically lost when the surface peaks start flattening generally after  $\sim 5$ -10 minutes of wear. Figure 3-26 quantifies this by using normalized histograms at the wear time at which surface mobility is lost. Sample 25, Figure 3-26a, and sample 27-1, Figure 3-26b, show similar height distributions with the same bandwidth for the heights, and with the surface dotted with a small number of high peaks. Sample 27-2, Figure 3-26c, on the contrary shows a surface height distribution containing mainly a flat surface, and with a miniscule number of high peaks.



*Figure 3-26: Normalized histograms for the samples when the hysteresis jumps, (a) Sample 25 at 9 minutes, (b) Sample 27-1 at 6 minutes, and (c) Sample 27-2 at 24 minutes.*

#### **3.4.4.2 Evolution of Surface Topographical Descriptors**

In the previous section, a quantitative look into the CA behaviour and how the topography changes as a surface wears was investigated. As surface topography changes, so do the various surface descriptors. These surface descriptors can offer an insight into studying the mobility traits of the drop on a surface. In the following section, a study into various surface descriptors is undertaken, and if the topography descriptors can be used to predict CA changes.

Root mean square (RMS) roughness is a statistical measurement of the square root of the average of the squares of the roughness measurements. Roughness is a measurement of the deviation of surface height from the mean line, and hence can be used to quantify surface texture.

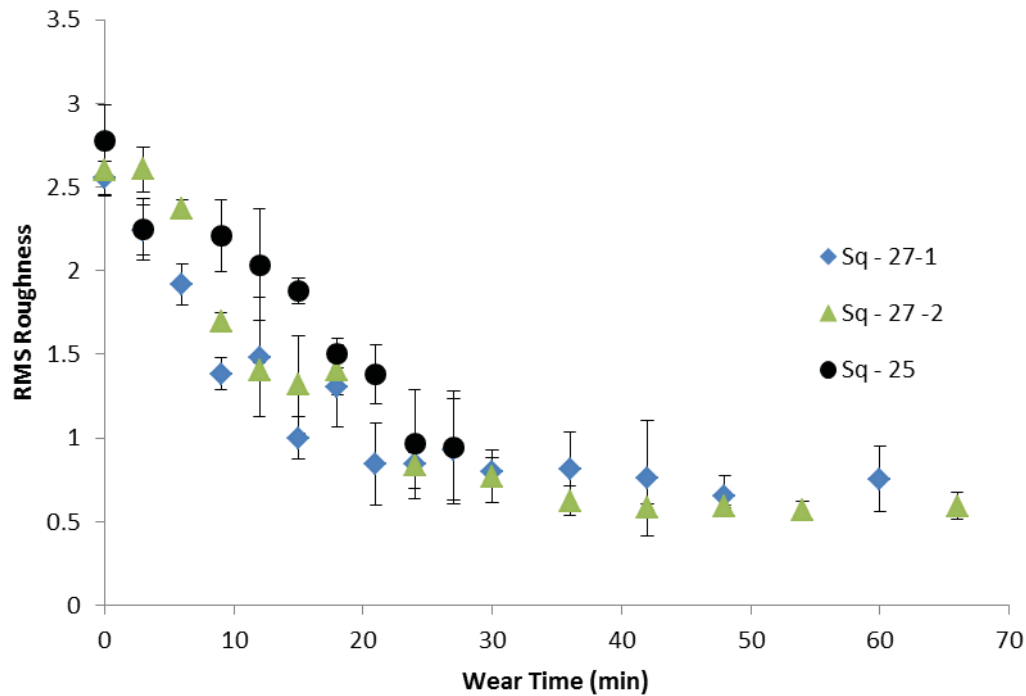


Figure 3-27: RMS roughness for PTFE worn surfaces.

Figures 3-14, 3-15, 3-16, 3-17, and 3-20 all show, by SEM and CSM that the peaks start to diminish as the surface starts to wear. Hence the roughness and RMS roughness should decrease too, as they are dependent on average heights. The slope for the RMS roughness curve in Figure 3-27 decreases roughly linearly until 24 minutes, and then it follows a very mild decreasing slope. For sample 25, SEM images in Figure 3-15 validate that the surface was abundant with peaks until 18 minutes of wear time and the peaks were being shaved off progressively. The RMS roughness curve in Figure 3-27 shows a decline for sample 25, showing that flattening of peaks is having an adverse effect on surface roughness as expected. Sample 25 surface has started flattening (peaks have diminished) at 24 minutes wear time, also validated by Figure 3-15f, and by 27 minutes peaks have totally flattened, Figure 3-15g. For sample 25, it is apparent in Figure 3-27 that the RMS roughness value for 24 and 27 minutes wear time lie in close vicinity of each other. Also, the slope after 24 minutes is smaller than the initial slope, for both samples 27-1 and 27-2. This is also validated by surface height data from CSM, as shown in Figure 3-20d, for sample 27-1. At 27 minutes, the peak distribution has diminished in relation to unworn peak surface distribution for samples 25 and 27-1. Correspondingly, the mobility of the surface is also diminished after this point for all the surfaces as shown in Figure 3-25. RMS roughness shows the same trend for all the samples, but the mobility (receding CA) for different samples is affected at different wear times for individual samples, Figure 3-25. When CA hysteresis increases, RMS roughness for samples 25 and 27-1 lie in close proximity, but for sample 27-2 it is roughly half the magnitude of that for sample 27-1. Hence, a definitive correlation between mobility and RMS roughness cannot be found. Repellency (advancing CA) for the surfaces given in Figure 3-25 increased until 9 minutes of wear and remained nearly constant after 21 minutes; it decreases with a gentle slope at intermediate times. The RMS

roughness slope on the contrary does not align with this behaviour. The slope rapidly decreases while the advancing CA increases minimally in the initial wear time period. The slope of the RMS roughness curve, Figure 3-27, does show consistent behaviour with the slope of wetting characteristics curve, Figure 3-25, as they are constant as wear time exceeds 30 minutes.

Surfaces can exhibit the same average and RMS roughness parameters, hence to distinguish and characterize surfaces additional parameters should be considered. Skewness and Kurtosis, are two roughness descriptors that may be useful. Skewness measures the asymmetry of the roughness profile about the mean line, and Kurtosis is a parameter that helps evaluate “peakedness” or “flatness” of the surface profile relative to normal distribution. The following sections discuss the relevancy of skewness and kurtosis in relation to PTFE abrasion. Skewness and kurtosis are normalized by the third and fourth power of the RMS roughness respectively, and hence can be strongly influenced by outliers.<sup>26</sup>

As mentioned above, skewness measures the asymmetry of the profile about the mean line. Zero signifies perfect symmetry about the mean line, and a surface having predominant plateau with deep valleys will exhibit a negative skewness, while a surface having disproportionate number of high peaks will exhibit positive skewness, illustrated in Figure 3-28. Skewness can be used for distinguishing different shapes having same RMS roughness and may be useful in monitoring different types of wear conditions.<sup>27</sup> For example, a surface having peaks, and its exact negative surface, containing valleys, will have the same average and RMS roughness. The magnitude of skewness will also be the same, except surfaces containing peaks will exhibit positive skewness.

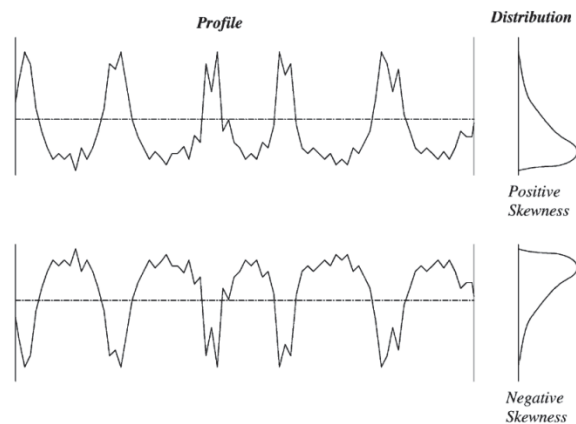


*Figure 3-28: Schematic showing surface profile and the corresponding skewness distribution curve.<sup>26</sup>*

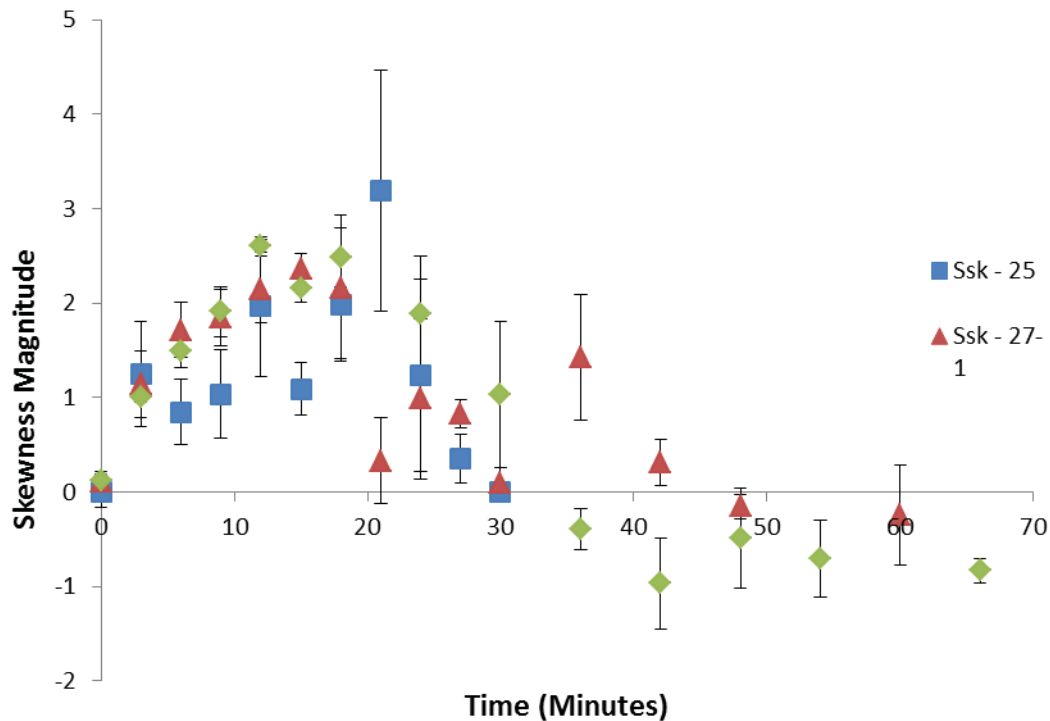


Figure 3-29: Evolution of skewness as a surface wears down.  
Error bars show the standard deviation in the parameter.

Figure 3-29 shows the graph of the evolution of the skewness parameter.

1. A starting value of  $\sim 0$  shows that surface is not skewed. This can mean that the surface is flat or that it has an equal distribution of high peaks and low valleys. This observation can be supplemented using kurtosis data, or RMS roughness data. Figure 3-27 shows high RMS roughness for an unworn surface, which rules out the possibility for a smooth surface.
2. As the surface wears, skewness increases positively showing that peaks are becoming more predominant. As Figures 3-14b, 3-15a and 3-16b show that the tops of peaks are shaved off, but valleys are unaffected, Figure 3-15b. This indicates that the value should be positively skewed, in favour of peaks. Skewness shows positive slope until 20 minutes and is highest at this point, showing high random distribution of peaks, which is corroborated by Figures 3-14d and 3-15c.
3. After 24 minutes, skewness decays indicating fewer peaks than before, and increasing plateaus. Figures 3-15h and 3-17d show that this is indeed the case.

Skewness can be divided into three regimes. Regime 1, when wear is starting and peaks are aplenty until 9 minutes. This also shows us that the majority of the peaks resist abrasion until 9 minutes, as shown in Figures 3-17b and 3-20b. Regime 2 has a more random disproportionate distribution of peaks, and large flat patches are on the surface until 20 minutes, as shown in



Figures 3-17c and 3-20c. Regime 3 signifies the region when peaks are decaying and the surface is becoming flattened, as illustrated by Figures 3-17d and 3-20d. In Figure 3-27 until 21 minutes, i.e., regime 1 and regime 2 for skewness, RMS roughness shows a large negative slope. After 21 minutes, i.e., regime 3 for skewness, RMS roughness has an almost constant slope in Figure 3-27. So a change in slope can help distinguish regime change, and indicate that wear is affecting the surface.

The skewness predicts that the surface is changing with respect to peaks and valleys, and that the distribution is random, but it does not predict mobility (receding CA) and repellency (advancing CA) for the surface. At 9 and 24 minutes, samples 27-1 and 27-2, have roughly the same skewness distribution but the contact angle hysteresis displayed is different at these wear times, Figure 3-25, showing that the topography is different. Even for a 21 minute worn surface, the skewness values fall within large error limits, and it is difficult to distinguish topography based on these values. For sample 25, SEM images in Figure 3-15 and CSM data in Figure 3-17 (Figure 3-20 for sample 27-1) shows that after 20 minutes, the peaks have predominantly been flattened. For example, SEM images of sample 25, at 18 minutes, Figure 3-15d, and 24 minutes, Figure 3-15f, show different topographies, also the wetting data in Figure 3-25 is somewhat similar, and from Figure 3-29 skewness values are close to each other within the error range. Thus, there is no way to distinguish even with corresponding RMS roughness data, the predominance of peaks or valleys in these samples just from skewness values. Hence supplemental kurtosis values may need to be taken into account too.

Hence, skewness helps in monitoring the dominance of peaks or valleys, or even if the surface is flat for PTFE surfaces. The slope helps us in determining the wear condition on the surface, but wetting characteristics show no definite trend as a surface wears.

As mentioned above, kurtosis is the parameter that helps evaluate “peakedness” or “flatness” of the surface profile relative to normal distribution. A surface having normal distribution (Gaussian) has kurtosis of 3, while surface with few peaks and low valleys shows kurtosis smaller than 3, and a surface with many high peaks and low valleys shows kurtosis greater than 3. Figure 3-30 illustrates these values. Surfaces with the same RMS roughness but different shapes can be distinguished with help of kurtosis. Kurtosis is a useful indicator for the presence of either peak or valley defects which may occur on a surface.<sup>27</sup> Figure 3-31 shows the kurtosis of surfaces as they are worn down.

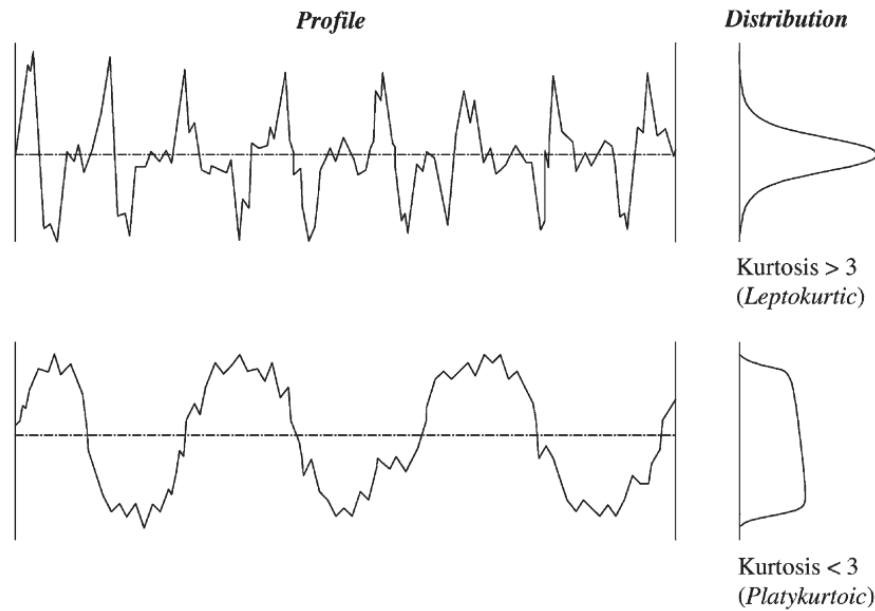


Figure 3-30: Schematic showing surface topography and corresponding kurtosis.<sup>26</sup>

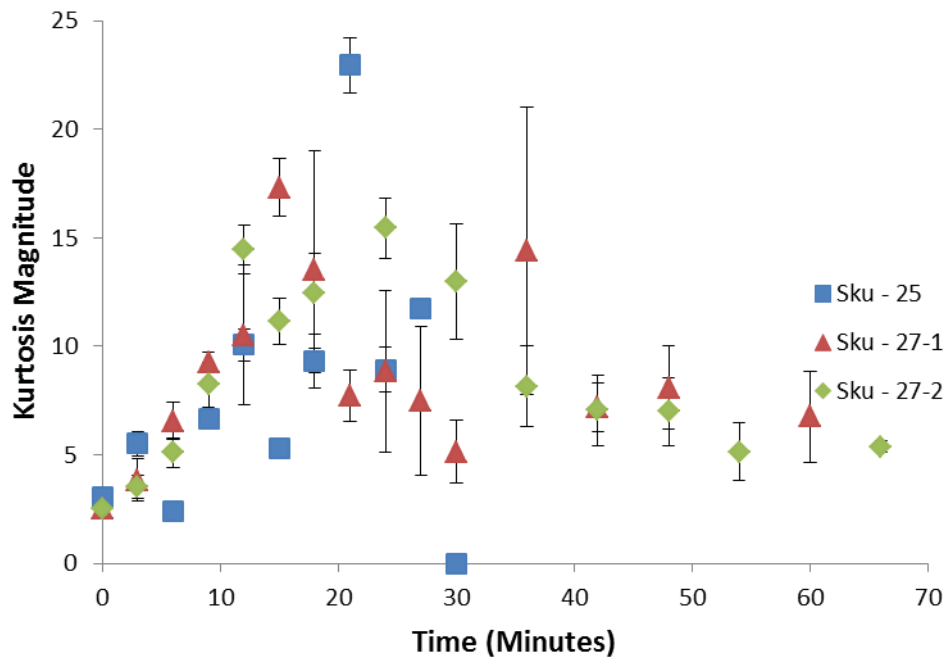


Figure 3-31: Evolution of kurtosis as a surface wears down.  
Error bars show the standard deviation in the parameter.

Also, the regimes 1, 2, and 3 as defined in the skewness section will be transferred over to kurtosis for comparison. If the kurtosis values do not give reasonable and defined trends in these regimes, new regimes will be defined for kurtosis.

1. The kurtosis value for the surfaces is increasing unequivocally in regime 1, as it should be because of increase in relative “peakedness” of the surface. In regime 1, the contact angle hysteresis remains nearly constant at  $\sim 3^\circ$ . Also, from SEM images for sample 25, Figure 3-15, the majority of the area is still covered by peaks and valleys. This randomness of the peak distribution implies that kurtosis will increase in this regime, as effectively the “peakedness” of the surface is increasing. Height distribution histograms in Figures 3-18 and 3-21 also show that the peaks although not dominant are a significant portion of the heights on the surface.
2. As the wear enters regime 2, all the peaks are affected and their height is decreasing which affects the kurtosis and it is wavering. The standard deviation in this regime is very high, illustrating the locally varying nature of topography at different points when the peaks have started to become affected. SEM images Figures 3-15b, c and d physically show the topography change in this regime. CSM data in Figure 3-17c and Figure 3-20c illustrate the onset of the regime, and the topography difference is apparent in Figure 3-17d and Figure 3-20d with the majority of peaks being flattened.
3. In regime 3, kurtosis decreases as the plateaus on the surface are increasing. The slope in this regime is mild, contrary to the slope in regime 1. This is because the majority of peaks have flattened, as they are the parameters that affect kurtosis. Also, wetting data in Figure 3-25 (both advancing and receding CA) shows a gentle slope in this regime, with a tendency to remain constant, showing that topography has already undergone the majority of the changes in previous wear time.

Skewness and kurtosis align with each other, and can supplement each other. The hindrance is that given the value for both of these parameters, one will not be able to identify the regime (1, 2, 3 etc.) of the state the surface is in without using any other quantitative method (height profile or SEM). This is due to the fact that certain values for both skewness and kurtosis are prone to fall in all three regimes. RMS roughness values can give an indication, but definite pinpointing is not possible.

Hence in their present individual form, skewness and kurtosis are unable to predict either adhesion or repellency of the surface. The roughness descriptors need to be combined and computed with other roughness parameters to gain a complete understanding of wetting characteristics.

### **3.4.5 Future Work**

The surface roughness parameters can help build an attack vector guided towards identifying a surface topography i.e., shape, and size of the peaks/valleys etc. Hence further investigation should be done, which can help a conclusive snapshot of a surface topography state. Further, these surface parameters should be studied in relation to wetting characteristics. The final aim should be to predict wetting characteristics based on surface topography.

## 4 Superhydrophobic and Superoleophobic Behaviour on Variant Geometry Micropillar Arrays

---

The design and fabrication of textured silicon wafers, with the intention of understanding repellence and mobility of fluids of different surface tensions, has been studied over the past two years. It has been shown that while all the wafers, designed and fabricated, exhibit SH behaviour, the surface's repellency, and the fluid's mobility vary between textures. Additionally, the work done has also consisted of refining the analytical process and optimizing surface and micropillar textures to achieve better superoleophobic surfaces. The work carried out as part of this study can be summarized as follows:

- Developed design rules to produce micropillar arrays of desired, arbitrary geometry and to produce a desired Cassie fraction
- Developed methods to use modified lithographic techniques to physically realize micropillar arrays with different undercut geometries and top surfaces
- Produced a surface that has multi-scale roughness to generate extremely low contact angle hysteresis
- Produced a surface that has enhanced repellency of oils in the superoleophobic surface
- Demonstrated that the Cassie equation does hold for the superoleophobic surface, allowing it to be used in the design of future surfaces

### 4.1 Introduction

The intent of this project is to produce superhydrophobic and superoleophobic behaviour by controlling the 3-D profile of surface roughness, with the ultimate goal of producing surfaces that are both highly repellent to liquids with a range of surface energies and behaviours. Using standard silicon etching techniques developed by the semiconductor industry it is possible to easily control two dimensions of geometry along the surface plane of the material being etched, while use of different materials with different isotropic and anisotropic etch rates allows for limited control of the third dimension of the profile. To this end, regular arrays of micropillars with variant sidewall profiles have been fabricated over the past year, with the work since August 2011 focused upon the oleophobic surface already fabricated.

As a review of terms, the primary metrics used for assessing the repellency and mobility of a liquid on a surface are contact angle and contact angle hysteresis. In particular, the advancing contact angle is strongly associated with how well a surface repels a liquid while the contact angle hysteresis, which is the difference between the advancing and receding contact angles, is associated with how easily the surface can shed the liquid.<sup>28</sup> By typical definitions a superhydrophobic surface is one that exhibits a contact angle  $>150^\circ$  and a contact angle hysteresis  $<10^\circ$ .

In terms of understanding contact angles on rough surfaces the primary governing equations are the Wenzel equation and the Cassie-Baxter equation. The Wenzel equation is valid for when a liquid has completely penetrated into the roughness present and is shown in Equation 4-1.<sup>29</sup>

$$\cos \theta_w = r \cos \theta_l \quad (4-1)$$

The governing variables are the intrinsic contact angle  $\theta_l$ , the apparent Wenzel contact angle  $\theta_w$ , and the surface roughness  $r$ , which is the ratio of the actual surface area in contact with the liquid, divided by the projected two dimensional surface area enclosed by the contact perimeter. In the event that a liquid fails to completely penetrate into the roughness and is thus suspended over a layer of gas, the Cassie-Baxter equation applies, as seen in Equation 4-2.<sup>6</sup>

$$\cos \theta_c = f_1 \cos \theta_l - f_2 \quad (4-2)$$

Here the apparent contact angle  $\theta_c$  is controlled by the intrinsic contact angle  $\theta_l$ , the ratio of the area of the drop in contact with the solid surface  $f_1$ , and the ratio of the area of the drop in contact with the gas phase  $f_2$ . In the Cassie-Baxter equation in the event that  $f_2$  goes to 0 then the equation reduces to the Wenzel equation and  $f_1 = r$ . In general  $f_1 + f_2 \geq 1$ , but in the event  $f_1 + f_2 = 1$  then a reduced form of the Cassie-Baxter equation can be used, taking the form seen in Equation 4-3.

$$\cos \theta_c = f(\cos \theta + 1) - 1 \quad (4-3)$$

In this formulation of the Cassie-Baxter equation  $f = f_1$  and the variable is frequently referred to as the Cassie fraction, a convention that shall be used in this report. This form is particularly useful for the purposes of design for photolithographic fabrication as the features can only be defined two dimensionally so  $f$  serves as a design parameter for laying out areas on the surface that will be etched and not etched. This method was used to establish from simple geometry a design equation for hexagonally packed pillars on the surface, seen in Equation 4-4.

$$f = \frac{2d^2}{\sqrt{12}x^2} \quad (4-4)$$

In this equation the separation between pillar centres,  $x$ , and the pillar diameter,  $d$ , are used to determine the Cassie fraction,  $f$ , although the equation can easily be rearranged to determine any of the three variables from the other two.

Since August 2011, work has proceeded primarily on refining the analysis and understanding of the superoleophobic surfaces consisting of micropillar arrays with overhanging caps fabricated previously, seen in Figure 4-1. These pillars were fabricated on a silicon wafer with a layer of silicon dioxide grown thermally on top, whereby the pattern was defined using standard photolithographic techniques. After etching the exposed silicon dioxide layer the underlying silicon layer was deep reactive ion etched, with the change that the ion etch was changed from an anisotropic vertical etch to an isotropic etch at the mid-point of the etch procedure so that at the tops of the pillars there would be an overhanging plate of silicon dioxide.

Analysis of the receding angles gathered previously showed a need for an improvement in technique in order to gather more precise and accurate results. This improvement of analysis has allowed for the better illumination of phenomena occurring on the surfaces. Of the eight cases fabricated,<sup>32</sup> seven were deemed viable for testing, as seen in Figure 4-2. The case not tested was as before, due to errors in the fabrication process producing a non-viable textured surface.

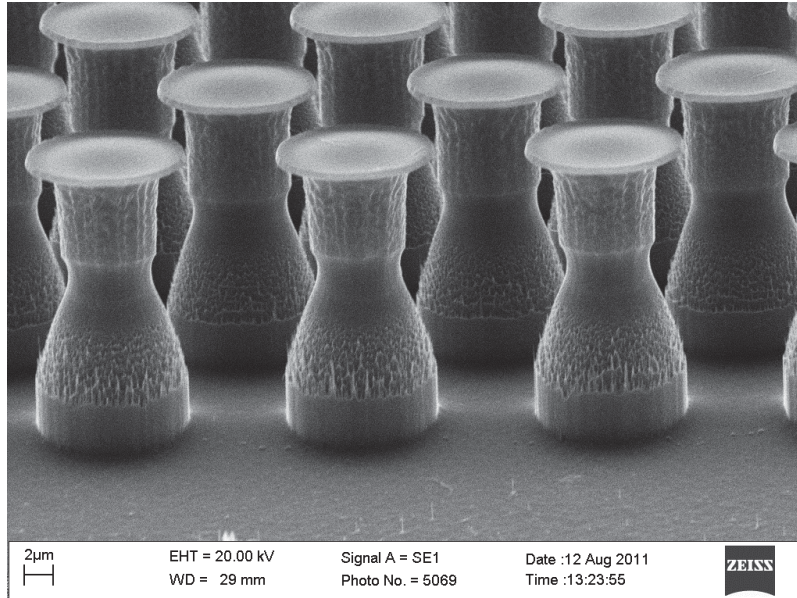


*Figure 4-1: SEM image of the micropillars with overhanging caps.  
Image taken at 7000X magnification.*

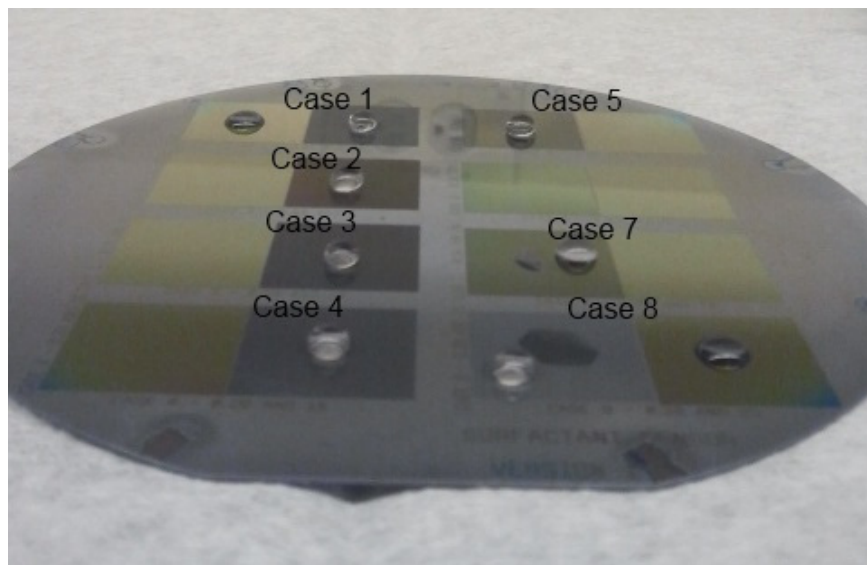


*Figure 4-2: The oleophobic wafer with placed hexadecane drops on the seven cases tested.*



## 4.2 Procedure

After initial analysis, done in August 2011, of the dynamic contact angles of water, ethylene glycol, and hexadecane on the various cases of the superoleophobic surfaces, deeper study of the results showed that in many of the cases the receding angle was not properly reached, producing ambiguity in the results and a large degree of uncertainty. A new set of measurements with a new measurement procedure was necessary to correct this issue.

Previously, to obtain the advancing and receding contact angles droplets of the studied liquids were developed on the surface using a top down needle to produce an initial 20 $\mu$ L droplet, then grown to 70 $\mu$ L and contracted back to 20 $\mu$ L at a rate of 0.5 $\mu$ L/s while a camera took images twice a second. This procedure proved insufficient to obtain the actual receding angle for the majority of the ethylene glycol and hexadecane trials, so a longer period of receding examination was needed. For the new set of trials, the droplets started at an initial volume of 25 $\mu$ L and had their volumes increased to 75 $\mu$ L and then reduced to 10 $\mu$ L, again at a rate of 0.5 $\mu$ L/s while a camera took images at a frequency of 2Hz. This procedure was performed with water, ethylene glycol (EG) and hexadecane (HDEC), with these liquids chosen for their varying surface tensions of 72.8mN/m, 47.7mN/m, and 27.47mN/m, respectively.<sup>30</sup> The end states for the advancing and receding processes involving hexadecane on Case 8 is shown in Figure 4-3.

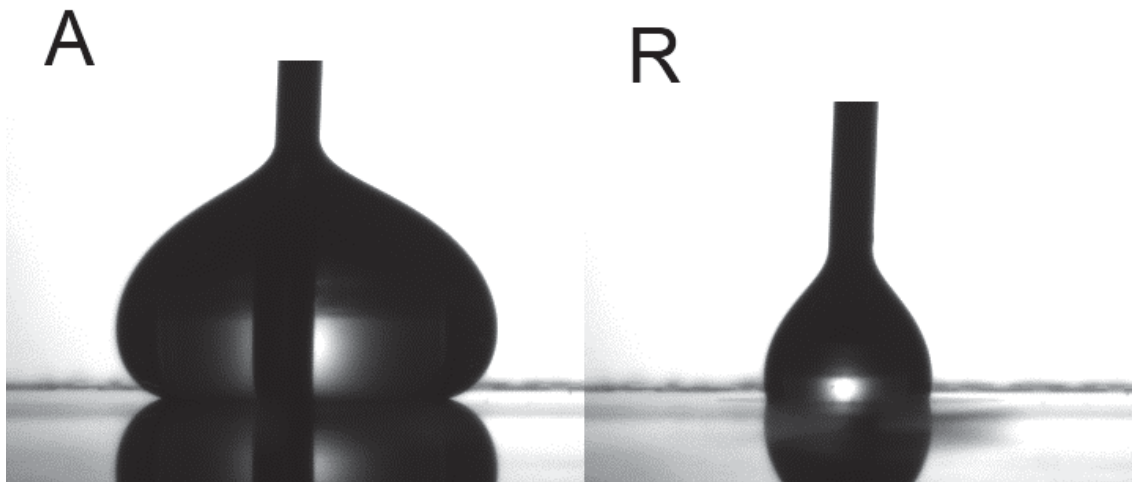


*Figure 4-3: Hexadecane drop developed on Case 8 of the surface. The end state of the advancing (A) drop when it is at 75 $\mu$ L is shown on the left, while the end state of the receding (R) drop when it is at 10 $\mu$ L is shown on the right.*

Special attention was given toward measuring not just the contact angles of the drops, but the contact radius of the drops so that ‘advancing’ and ‘receding’ could be properly assessed. In this case, the definition of the advancing contact angle is the contact angle measured when the radius of contact between the drop and the surface is increasing, while the receding contact angle is the contact angle measured while the contact radius is decreasing. The extended period of volume decrease combined with this more careful method of determining the receding contact angle produced results of greater accuracy and precision than previously reported.

### 4.3 Results

The dimensions of the pillar tops had already been determined previously and are re-iterated for illustrative purposes in Table 4-1. The measured values of Table 4-1 are necessary to further understanding the analysis to follow as the Cassie fraction,  $f_c$ , is needed to make predictions about how the surface should behave and compare to actual behaviour. Additionally, while Case 7 was measured, its behaviour was deemed too far outside the rest of the surfaces to include in analysis, its deviation accounted for by the extreme tightness of the pillar spacing and intermittent connections between the tops of the pillar plates, as seen in Figure 4-4. The combination of the visible fabrication errors and the outlying contact angle data has led to the conclusion that Case 7 is behaving in a manner different from the rest of the cases and thus a proper comparison between them is not possible.

*Table 4-1: Measured dimensions of the tops of the pillars  
for the oleophobic wafer compared with their designed dimensions.*

	Designed Diameter (μm)	Measured Diameter (μm)	Designed Pillar Spacing (μm)	Measured Pillar Spacing (μm)	Designed Cassie Fraction	Measured Cassie Fraction
Case 1	20	20.6	16	15.4	0.280	0.297
Case 2	5	6.0	4	3.0	0.280	0.403
Case 3	10	11.1	8	6.9	0.280	0.345
Case 4	15	15.3	12	11.7	0.280	0.291
Case 5	20	20.2	5.35	5.15	0.560	0.571
Case 6	5	N/A	0.56	N/A	0.560	N/A
Case 7	10	10.8	2.73	1.93	0.560	0.653
Case 8	25	25.6	20	19.4	0.280	0.294

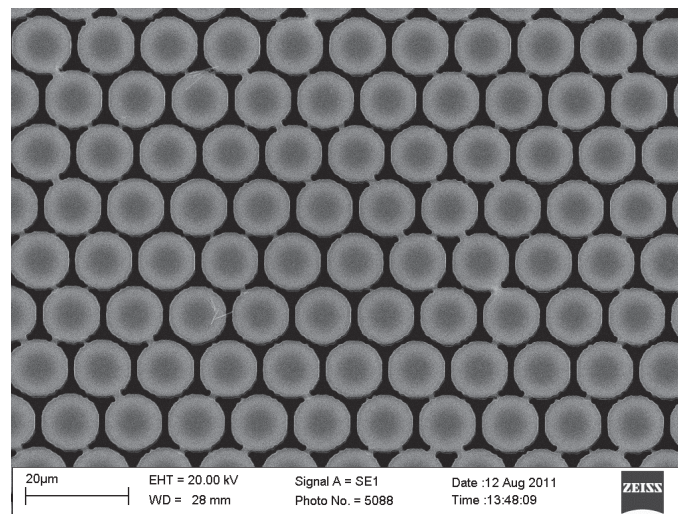


*Figure 4-4: SEM image of Case 7 and the intermittent connectivity between the pillar tops. Image taken at 5000X.*

Of the remaining six cases and the intrinsic contact angle taken from the smooth parts of the wafer, the data collected is summarized in Tables 4-2, 4-3, and 4-4, showing the contact angles for water, ethylene glycol, and hexadecane, respectively. The contact angle hysteresis is also shown for all cases.

*Table 4-2: Table of measured contact angles with water on the various cases.*

<b>Case</b>	<b>Advancing CA (°)</b>	<b>Receding CA (°)</b>	<b>Contact Angle Hysteresis (°)</b>
Intrinsic	126.3±0.3	89.9±1.3	36.4±1.3
1	170.0±1.9	126.0±0.7	44.0±2.0
2	166.7±1.2	121.7±0.3	45.0±1.2
3	169.5±1.9	123.3±1.1	46.2±2.2
4	167.9±1.5	122.2±1.8	45.7±2.3
5	169.9±1.0	107.9±1.3	62.0±1.6
8	166.6±1.7	116.9±0.7	49.7±1.8

*Table 4-3: Table of measured contact angles with ethylene glycol on the various cases.*

<b>Case</b>	<b>Advancing CA (°)</b>	<b>Receding CA (°)</b>	<b>Contact Angle Hysteresis (°)</b>
Intrinsic	98.2±1.2	61.1±1.8	37.1±2.1
1	165.0±2.5	105.5±1.1	59.5±2.7
2	153.3±2.1	94.7±0.8	58.6±2.2
3	160.9±2.9	102.0±0.5	58.9±2.9
4	165.0±2.9	104.3±0.7	60.7±3.0
5	153.3±1.7	84.5±1.0	68.8±2.0
8	165.6±4.2	104.0±1.1	61.6±4.3

*Table 4-4: Table of measured contact angles with hexadecane on the various cases.*

<b>Case</b>	<b>Advancing CA (°)</b>	<b>Receding CA (°)</b>	<b>Contact Angle Hysteresis (°)</b>
Intrinsic	81.0±2.2	43.9±1.5	37.1±2.7
1	167.0±3.4	94.5±2.0	72.5±3.9
2	155.3±2.7	88.7±1.9	66.6±3.3
3	160.8±3.2	95.5±1.1	65.3±3.4
4	164.6±1.7	98.1±0.8	66.5±1.9
5	155.6±0.7	73.8±1.2	81.8±1.4
8	164.7±3.5	97.4±2.3	67.3±4.2

As can be seen, all of the textured cases examined showed a dramatic increase in both advancing and receding angles in comparison with the intrinsic contact angles, with increases in advancing contact angles >80° for some cases with hexadecane. There is a trade-off, however, readily seen in the fact that the contact angle hysteresis has also increased for all cases.

## 4.4 Analysis

Analysis of the data collected begins by comparing our observed data with theory. As we do not have observational measurements to assess the appearance of the underside of the drops, on the surfaces, we do not know whether any sagging of the drops occurs, and therefore, we do not know the  $f_2$  value and we cannot use Equation 4-2. We must therefore assume that  $f_1 + f_2 = 1$  and use Equation 4-3 to make any predictions. To begin with, we take the intrinsic advancing and receding angles and the Cassie fractions determined in Table 4-1, and use them to predict what the advancing and receding angles should be for each case. These values along with the observed values have been plotted against the Cassie fraction in Figures 4-5, 4-6, and 4-7, for water, ethylene glycol, and hexadecane, respectively. The intrinsic contact angles are included as the limiting point where  $f = 1$ .

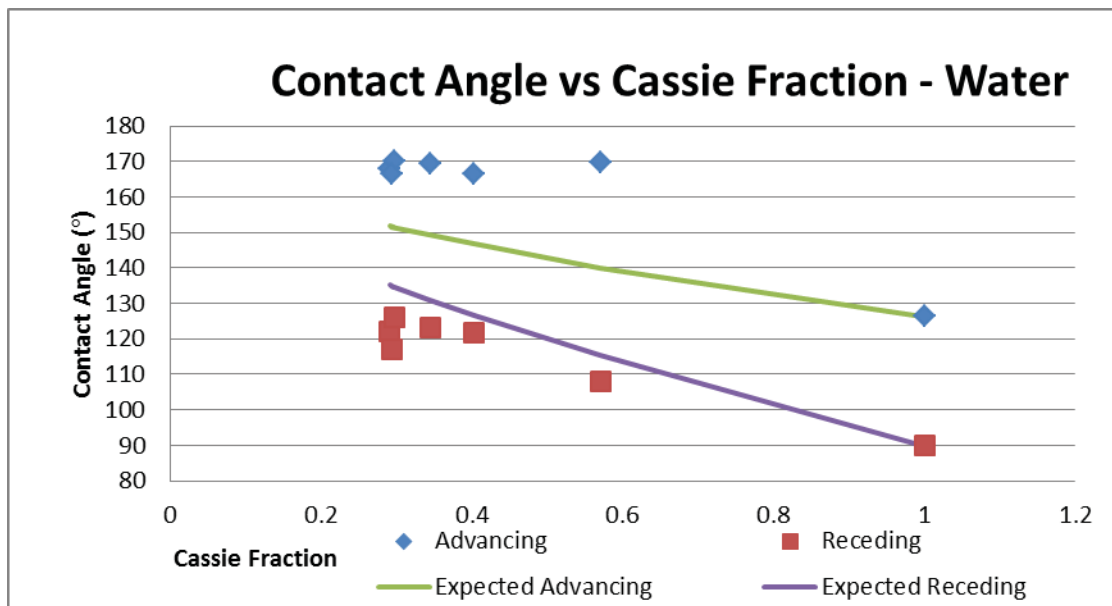


Figure 4-5: Expected and observed advancing and receding angles for water plotted against the Cassie fractions for each case.

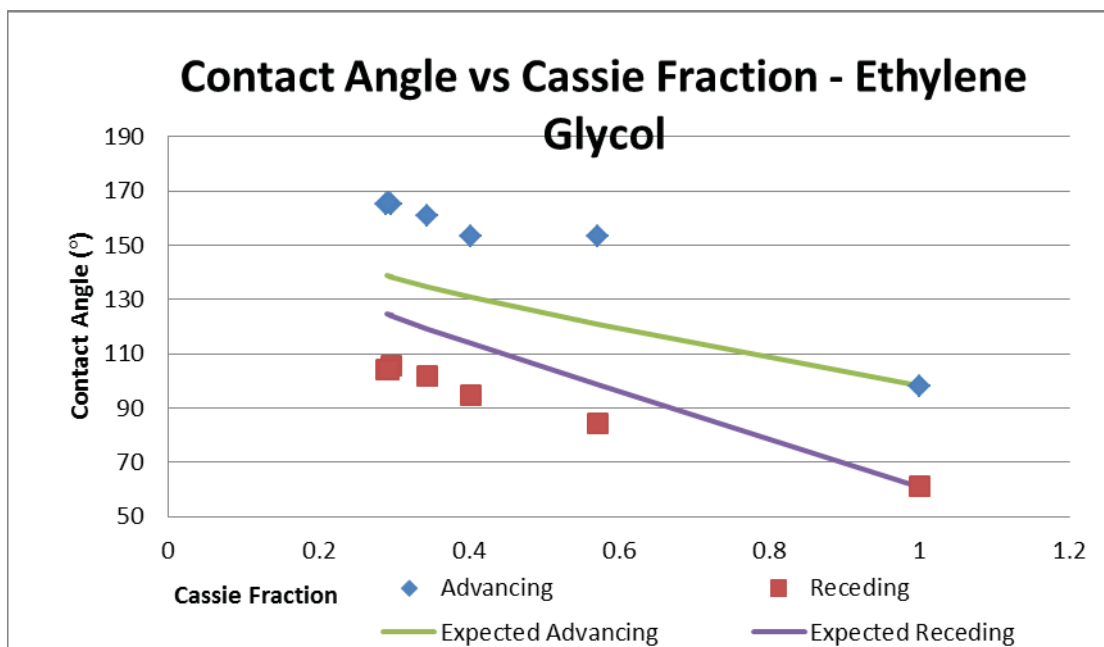


Figure 4-6: Expected and observed advancing and receding angles for ethylene glycol plotted against the Cassie fractions for each case.

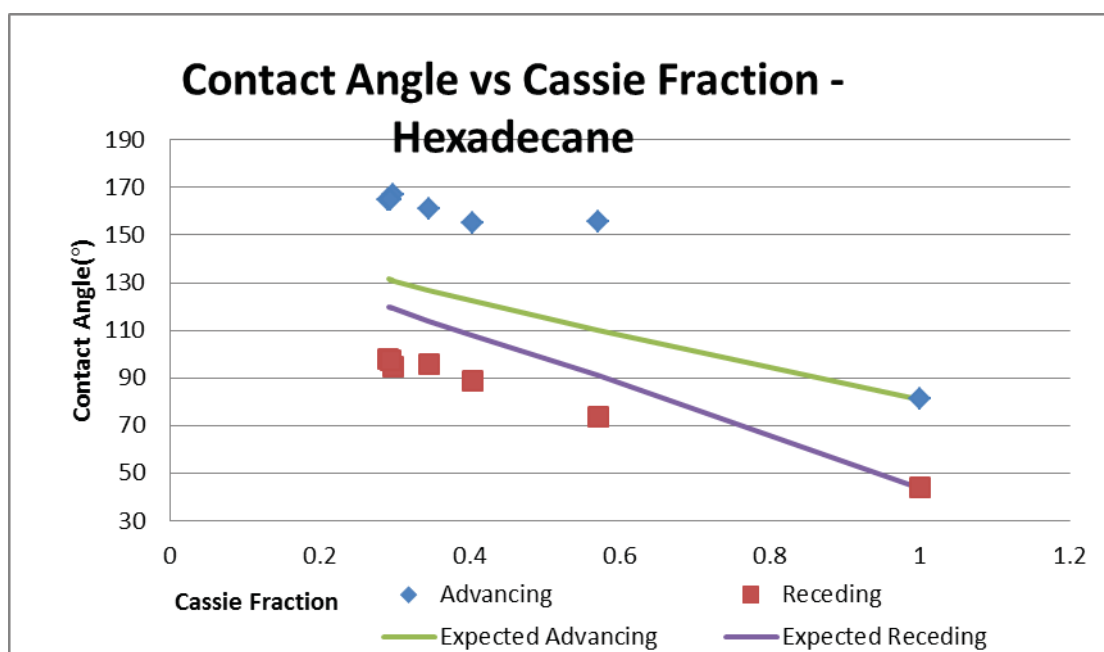


Figure 4-7: Expected and observed advancing and receding angles for hexadecane plotted against the Cassie fractions for each case.

As seen in the Figures presented, the observed advancing angles are all well above the predicted values, while the receding angles are well below the predicted angles, although both advancing and receding demonstrate a generally linear trend of decreasing contact angles as the Cassie fraction increases. However, while this data is useful in showing trends, evidence suggests that the Cassie-Baxter equation is only valid for the equilibrium contact angles.<sup>31</sup> Determining the equilibrium contact angle from the advancing and receding angles is a subject not well represented in literature, so multiple averaging methods were sought to determine a way to find appropriate values in between the advancing and receding angles. Of the averaging methods attempted, the one that showed the best fit between theoretical values and observed values was Equation 4-5.

$$\cos \theta_E = 0.5 \cos \theta_A + 0.5 \cos \theta_R \quad (4-5)$$

This method determines the equilibrium contact angle  $\theta_E$  by taking the cosines of the advancing contact angle  $\theta_A$  and receding contact angle  $\theta_R$  and giving them an equal weight of half each. Using this method, averaged contact angles were determined for all the cases and all the liquids, and the intrinsic equilibrium contact angle was then used to predict the contact angles for the cases using Equation 4-3. The observed and predicted averaged contact angles are presented in Figures 4-8, 4-9 and 4-10.

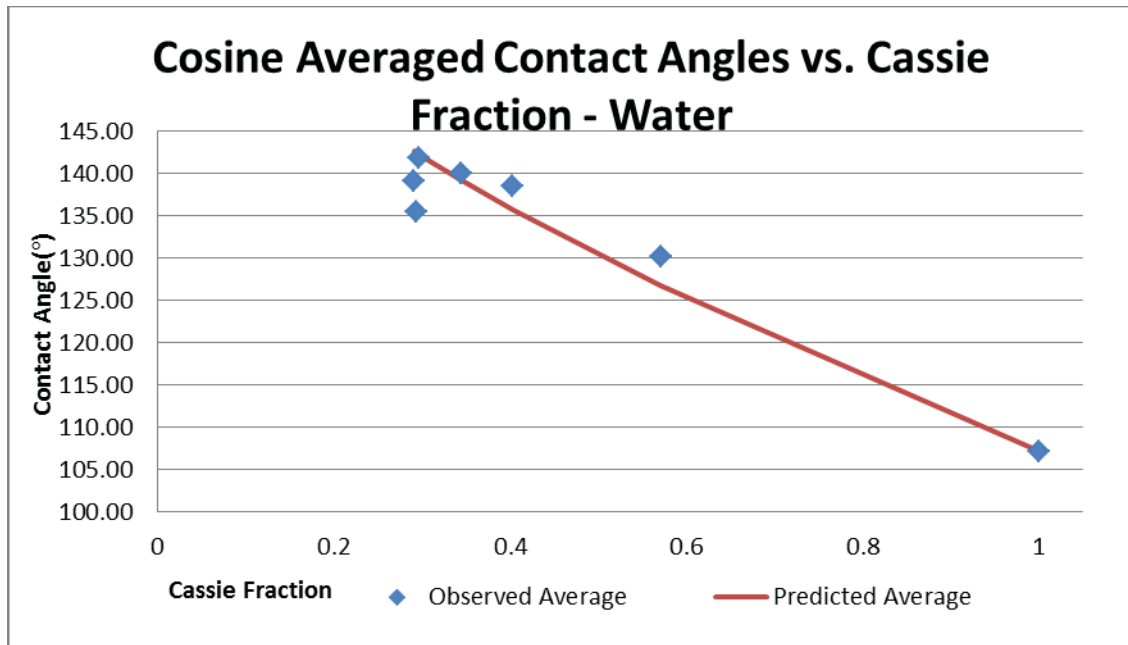


Figure 4-8: Cosine averaged contact angles with water vs. Cassie fraction.



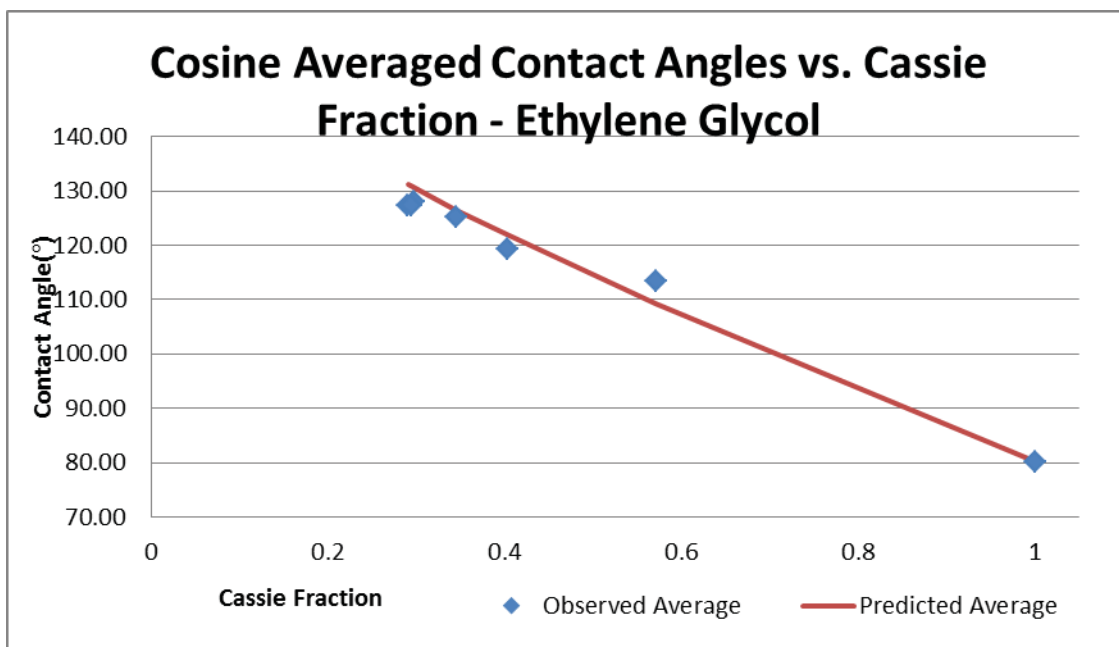


Figure 4-9: Cosine averaged contact angles with ethylene glycol vs. Cassie fraction.

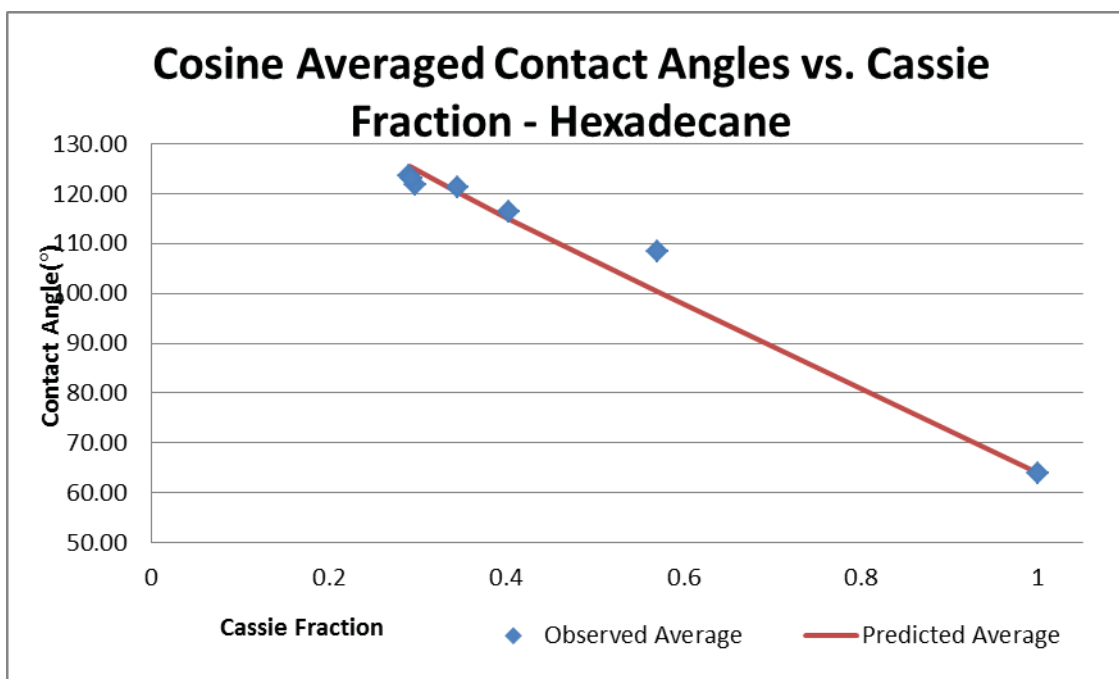


Figure 4-10: Cosine averaged contact angles with hexadecane vs. Cassie fraction.

As can be seen from the Figures presented, the cosine averaged contact angles follow predicted values strongly, indicating that the Cassie-Baxter equation still holds for these surfaces despite the strong degree of enhancement in repellency and increase in contact angle hysteresis exhibited. This finding suggests that even with complex undercut geometries the Cassie-Baxter equation will hold and thus can be used for the purposes of designing new surfaces using the same design rules as have been previously devised.

## **4.5 Future Work**

Due to the limited number of data points from the first set of surfaces, future work should be focused on better discerning what parameters have the greatest effect on contact angle. The past several months have been devoted to design and fabrication of a new set of surfaces with 17 cases in comparison to 6 and a much more varied spectrum of Cassie fractions, pillar diameters, and pillar separations. Initial results are just arriving with these new surfaces that should allow confirmation of behaviour with differing horizontal geometries.

Because of the greatly expanded contact angle hysteresis from intrinsic values, the future step should also include a thorough examination of drop shedding tendencies with tilted angle experiments and wind tunnel testing to confirm that the enhancement in repellency has come at the expense of drop mobility on the surfaces.

Also, an examination of cross-sectional geometry is needed to check that the effects seen are not just for circular plate geometries, but can be generalized to any geometry. The final result should lead to producing surfaces that exhibit both high repellency to water and oils and show a low contact angle hysteresis so that fully superoleophobic surfaces could be fabricated.

## 5 Publications

---

The work performed during the course of the current reporting period (year three), has also lead to the publication and presentation of the following work:

### Journal Publications

- G. Fang, A. Amirfazli, “Understanding the Edge Effect in Wetting: A Thermodynamic Approach”, *Langmuir*, 28, 9421-9430, 2012

### Journal Papers (in preparations)

- B.M. Koch, J.W. Elliott, A. Amirfazli, “Towards Understanding of Superomni-phobic Surfaces”

### Conference Presentations

- G. Fang, A. Amirfazli, “A Thermodynamic Approach to Describe Spreading of Sessile Drops Encountering a Sharp Edge”, CECAM workshop "Modeling Wetting Phenomena: From Particle Based Models to the Continuum" Lausanne, Switzerland, Sept. 14-16, 2011

This page intentionally left blank.

## References

---

- [1] Bayer, I. S.; Steele, A.; Martorana, P. J.; Loth, E. *Applied Surface Science* 2010, 257, 823–826.
- [2] Bayer, I. S.; Steele, A.; Martorana, P.; Loth, E.; Robinson, S. J.; Stevenson, D. *Applied Physics Letters* 2009, 95, 063702.
- [3] Bayer, I. S.; Steele, A.; Martorana, P. J.; Loth, E.; Miller, L. *App. Phys. Lett.* 2009, 94, 163902.
- [4] Steele, A.; Bayer, I.; Loth, E. *Nano Letters* 2009, 9, 501–505.
- [5] Bayer, I. S.; Brown, A.; Steele, A.; Loth, E. *Appl. Phys. Express* 2009, 2, 125003.
- [6] Cassie, A. B. D.; Baxter, S. *Trans. Faraday Soc.* 1944, 40, 546–551.
- [7] D’Acunzi, M.; Mammen, L.; Singh, M.; Deng, X.; Roth, M.; Auernhammer, G. K.; Butt, H.-J.; Vollmer, D. *Faraday Discuss.* 146, 35–48.
- [8] Luo, C.; Zheng, H.; Wang, L.; Fang, H.; Hu, J.; Fan, C.; Cao, Y.; Wang, J. *Angew. Chem. Int. Ed. Engl.* 2010, 49, 9145–9148.
- [9] Wu, J.; Zhang, M.; Wang, X.; Li, S.; Wen, W. *Langmuir* 2011, 27, 5705–5708.
- [10] Minko, S.; Müller, M.; Motornov, M.; Nitschke, M.; Grundke, K.; Stamm, M. *Journal of the American Chemical Society* 2003, 125, 3896–3900.
- [11] ASTM International ASTM Standard F735-06, 2003 - Standard Test Method for Abrasion Resistance of Transparent Plastics and Coatings Using the Oscillating Sand Method 2003.
- [12] Kulinich, S. A.; Farzaneh, M. *Langmuir* 2009, 25, 8854–8856.
- [13] Mishchenko, L.; Hatton, B.; Bahadur, V.; Taylor, J. A.; Krupenkin, T.; Aizenberg, J. *ACS Nano* 2010, 4, 7699–7707.
- [14] Choi, W.; Tuteja, A.; Chhatre, S.; Mabry, J. M.; Cohen, R. E.; McKinley, G. H. *Advanced Materials* 2009, 21, 2190–2195.
- [15] Shirtcliffe, N. J.; McHale, G.; Newton, M. I.; Zhang, Y. *ACS Appl Mater Interfaces* 2009, 1, 1316–1323.
- [16] McHale, G.; Shirtcliffe, N. J.; Evans, C. R.; Newton, M. I. *Applied Physics Letters* 2009, 94, 064104–064104–3.
- [17] Reick, F. G. Toys and games using superhydrophobic surfaces, US Patent 4199142, 1980.

- [18] Thomas, P. Surface Coatings International Part B: Coatings Transactions 1998, 81, 604–609.
- [19] Tannenbaum, H. P. Fluoropolymer non-stick coatings, US Patent 6761964, 2004.
- [20] Deng, X.; Mammen, L.; Butt, H.-J.; Vollmer, D. Science 2012, 335, 67–70.
- [21] Deng, X.; Mammen, L.; Zhao, Y.; Lellig, P.; Müllen, K.; Li, C.; Butt, H.; Vollmer, D. Advanced Materials 2011, 23, 2962–2965.
- [22] Larmour, I. A.; Saunders, G. C.; Bell, S. E. J. ACS Applied Materials & Interfaces 2010, 2, 2703–2706.
- [23] Xu, Q. F.; Mondal, B.; Lyons, A. M. ACS Appl Mater Interfaces 2011, 3, 3508–3514.
- [24] Xiu, Y.; Liu, Y.; Hess, D. W.; Wong, C. P. Nanotechnology 2010, 21, 155705.
- [25] Neumann, A. W.; Spelt, J. Applied Surface Thermodynamics; CRC Press, 1996.
- [26] Gadelmawla, E. S.; Koura, M. M.; Maksoud, T. M. A.; Elewa, I. M.; Soliman, H. H. Journal of Materials Processing Technology 2002, 123, 133–145.
- [27] Michigan Metrology 3D Functional Parameters.
- [28] Pierce, E.; Carmona, F.; Amirfazli, A. Colloids and Surfaces A: Physicochemical and Engineering Aspects 2008, 323, 73–82.
- [29] Wenzel, R. N. Industrial & Engineering Chemistry 1936, 28, 988–994.
- [30] Surface tension values of some common test liquids for surface energy analysis  
<http://www.surface-tension.de/>.
- [31] Johnson, R.; Dettre, R. Advances in Chemistry, 1964, Vol 43, p112-135.
- [32] Amirfazli, A., DRDC Atlantic CR 2011-255, October 2011.



## List of symbols/abbreviations/acronyms/initialisms

---

2k-4FVBA	Fluonova's Two-component Fluorinated Polyurethane sealant
3-D	Three-Dimensional
ACS	American Chemical Society
AF	Amorphous Fluoropolymer
ASME	American Society of Mechanical Engineers
ASTM	American Society for Testing and Materials
B#	Superhydrophobic coating Batch Number #
CA	Contact Angle
CAH	Contact Angle Hysteresis
CDF	Cumulative probability Distribution Function
CMC	Critical Micelle Concentration
CSM	Confocal Scanning Microscopy
CU	Complete Undercut
DI	De-Ionized
DMSO	Dimethyl Sulfoxide
DND	Canadian Department of National Defence
DRIE	Deep Reactive Ion Etching
EG	Ethylene Glycol
FE	Free Energy
FEB	Free Energy Barrier
HDEC	Hexadecane
HDMS	Hexamethyldisilazane
HU	Hybrid Undercut
ICNMM	International Conference on Nanochannels, Microchannels and Minichannels
IPA	Isopropyl Alcohol
L	Litre
LOC	Lab-On-Chip
LOP	Lab-On-Paper
LSG	Lesser Silicon Grass
McMat	Applied Mechanics and Materials
MSG	Major Silicon Grass
OP	Oleophobic
OTS	Octadecyltrichlorosilane
PMMA	Poly(methyl methacrylate)
POSS	Polyhedral Oligomeric Silsesquioxanes
PTFE	Polytetrafluoroethylene
R&D	Research and Development
rpm	Revolutions per minute
SA	Sliding Angle
SDS	Sodium Dodecyl Sulfate
SEM	Scanning Electron Microscopy
SH	Superhydrophobic
SHS	Superhydrophobic Surface
SIS	International Symposium on Surfactants in Solution

SOS	Superoleophobic Surface
SS	Surfactant Sensor
TFE	Trifluoroethanol
TPCL	Three-Phase Contact Line
V	Volume

## Distribution list

---

Document No.: DRDC Atlantic CR 2012-216

### **LIST PART 1: Internal Distribution by Centre**

- 1 Paul Saville, DRDC Atlantic
  - 1 Gary Fisher, H/DLP DRDC Atlantic
  - 1 H/DLA, DRDC Atlantic
  - 3 DRDC Atlantic Library (1 hard copy, 2 CDs)
- 
- 6 TOTAL LIST PART 1

### **LIST PART 2: External Distribution by DRDKIM**

- 1 Library and Archives Canada  
Attn: Military Archivist, Government Records Branch
  - 1 Scott Duncan, DRDC Suffield
  - 1 Alidad Amirfazli, Department of Mechanical Engineering, University of Alberta,  
Edmonton, Alberta T6G 2G8
  - 1 DSTL 7, Regan Reshke, Empire Building, 496 Discovery Ave.  
Kingston, Ontario K7K 7E9
  - 1 DRDKIM
- 
- 5 TOTAL LIST PART 2

### **11 TOTAL COPIES REQUIRED**

This page intentionally left blank.

DOCUMENT CONTROL DATA		
(Security classification of title, body of abstract and indexing annotation must be entered when the overall document is classified)		
1. ORIGINATOR (The name and address of the organization preparing the document. Organizations for whom the document was prepared, e.g., Centre sponsoring a contractor's report, or tasking agency, are entered in section 8.)	2. SECURITY CLASSIFICATION (Overall security classification of the document including special warning terms if applicable.)	
Alidad Amirfazli Department of Mechanical Engineering University of Alberta Edmonton, Alberta, T6G 2G8	UNCLASSIFIED (NON-CONTROLLED GOODS) DMC A REVIEW: GCEC APRIL 2011	
3. TITLE (The complete document title as indicated on the title page. Its classification should be indicated by the appropriate abbreviation (S, C or U) in parentheses after the title.)		
Superomniphobic Surfaces for Military Applications: Nano- and Micro-Fabrication Methods: Year Three Report		
4. AUTHORS (last name, followed by initials – ranks, titles, etc. not to be used)		
Amirfazli, Alidad		
5. DATE OF PUBLICATION (Month and year of publication of document.)	6a. NO. OF PAGES (Total containing information, including Annexes, Appendices, etc.)	6b. NO. OF REFS (Total cited in document.)
October 2012	98	32
7. DESCRIPTIVE NOTES (The category of the document, e.g., technical report, technical note or memorandum. If appropriate, enter the type of report, e.g., interim, progress, summary, annual or final. Give the inclusive dates when a specific reporting period is covered.)		
Contract Report		
8. SPONSORING ACTIVITY (The name of the department project office or laboratory sponsoring the research and development – include address.)		
Defence R&D Canada – Atlantic 9 Grove Street P.O. Box 1012 Dartmouth, Nova Scotia B2Y 3Z7		
9a. PROJECT OR GRANT NO. (If appropriate, the applicable research and development project or grant number under which the document was written. Please specify whether project or grant.)	9b. CONTRACT NO. (If appropriate, the applicable number under which the document was written.)	
12SZ20	W7707-098197	
10a. ORIGINATOR'S DOCUMENT NUMBER (The official document number by which the document is identified by the originating activity. This number must be unique to this document.)	10b. OTHER DOCUMENT NO(s). (Any other numbers which may be assigned this document either by the originator or by the sponsor.)	
	DRDC Atlantic CR 2012-216	
11. DOCUMENT AVAILABILITY (Any limitations on further dissemination of the document, other than those imposed by security classification.)		
12. DOCUMENT ANNOUNCEMENT (Any limitation to the bibliographic announcement of this document. This will normally correspond to the Document Availability (11). However, where further distribution (beyond the audience specified in (11) is possible, a wider announcement audience may be selected.)		

13. **ABSTRACT** (A brief and factual summary of the document. It may also appear elsewhere in the body of the document itself. It is highly desirable that the abstract of classified documents be unclassified. Each paragraph of the abstract shall begin with an indication of the security classification of the information in the paragraph (unless the document itself is unclassified) represented as (S), (C), (R), or (U). It is not necessary to include here abstracts in both official languages unless the text is bilingual.)

Superomniphobic surfaces possess unique properties that limit the ability of aqueous and organic liquids to adhere to the surface. As a result surface contamination should be minimized and their cleanability improved. Such traits in a material will have potential benefits to military systems ranging from rainwear, to chemical agent protection, to improved communications, and corrosion protection. This document reports on: the improvement of a sprayable superomniphobic coating by modifying the components; the study of the relationship between surface wear and wetting characteristics using confocal microscopy; and the interpretation of contact angle measurements for liquids on lithographically produced surfaces. A more durable coating was made however it was still susceptible to degradation with liquid contact duration. Skewedness and root mean square roughness surface descriptors have been identified for characterizing wear-wetting relationships; however, a combination of many surface parameters may be required to adequately wetting-wear behaviour. Finally it was found that the cosine of the measured contact angle accurately agrees with the cosine angle predicted by the Cassie equation for measurements made on complex lithographic surfaces, indicating that this equation can be used for designing surfaces.

14. **KEYWORDS, DESCRIPTORS or IDENTIFIERS** (Technically meaningful terms or short phrases that characterize a document and could be helpful in cataloguing the document. They should be selected so that no security classification is required. Identifiers, such as equipment model designation, trade name, military project code name, geographic location may also be included. If possible keywords should be selected from a published thesaurus, e.g., Thesaurus of Engineering and Scientific Terms (TEST) and that thesaurus identified. If it is not possible to select indexing terms which are Unclassified, the classification of each should be indicated as with the title.)

Superhydrophobic; Non-wetting; Repellent; Omniphobic; Oleophobic



This page intentionally left blank.

## **Defence R&D Canada**

Canada's leader in defence  
and National Security  
Science and Technology

## **R & D pour la défense Canada**

Chef de file au Canada en matière  
de science et de technologie pour  
la défense et la sécurité nationale



[www.drdc-rddc.gc.ca](http://www.drdc-rddc.gc.ca)